QUANTUM ELECTRODYNAMICS WITH SUPERCONDUCTING CIRCUITS: EFFECTS OF DISSIPATION AND FLUCTUATIONS

Zur Erlangung des akademischen Grades eines
DOKTORS DER NATURWISSENSCHAFTEN
von der Fakultät für Physik des
Karlsruher Instituts für Technologie

genehmigte

DISSERTATION

von

Dipl.-Phys. Stephan André
aus Karlsruhe

Tag der mündlichen Prüfung: 1.06.2012

Referent: Prof. Dr. Gerd Schön

Korreferent: Prof. Dr. Alexander Shnirman

Contents

List of Publications

Publications in refereed journals

1) J. Hauss, A. Fedorov, S. André, V. Brosco, C. Hutter, R. Kothari, S. Yeshwant, A. Shnirman, and G. Schön, *Dissipation in circuit quantum electrodynamics: lasing and cooling of a low-frequency oscillator*, New J. Phys. **10**, 095018 (2008).

2) S. André, V. Brosco, A. Shnirman, and G. Schön, *Phase diffusion and locking in single-qubit lasers*, Phys. Rev. A **79**, 053848 (2009).

3) S. André, P. Q. Jin, V. Brosco, J. H. Cole, A. Romito, A. Shnirman, and G. Schön, *Single-qubit lasing in the strong coupling regime*, Phys. Rev. A **82**, 053802 (2010).

4) S. André, L. Guo, V. Peano, M. Marthaler, and G. Schön, *Emission spectrum of the driven nonlinear oscillator*, Phys. Rev. A **85**, 053825 (2012).

Publications in conference proceedings

5) S. André, V. Brosco, A. Fedorov, G. Schön, and A. Shnirman, *Decoherence and relaxation in driven circuit QED systems*, AIP Conf. Proc. **1074**, 4 (2008), *Proceedings of the 2nd int. workshop on solid state quantum computing, Taipei, Taiwan, 25-27 June 2008.*

6) S. André, V. Brosco, M. Marthaler, A. Shnirman, and G. Schön, *Few-qubit lasing in circuit QED*, Physica scripta **T 137**, 014016 (2009), *Proceedings of the Nobel Symposium 2009, Qubits for future quantum computers, May 2009 in Göteborg, Sweden.*

7) S. André, V. Brosco, A. Shnirman, and G. Schön, *Superconducting micromasers*, Physica E **42**, 444 (2010), *Proceedings of the conference "Frontiers of quantum and mesoscopic thermodynamics", Prague, July 28 - August 2, 2008.*

8) L. Guo, M. Marthaler, S. André, and G. Schön, *The role of damping for the driven anharmonic quantum oscillator*, *submitted to "Journal of Physics: Conference Series"* (2012).

Acknowledgements

First of all I want to thank my supervisors who worked together with me during my time as a Diploma and PhD student at the institute. They all had a big part in helping me to do the scientific work that finally led to this thesis. So a big thanks goes to Valentina Brosco, Jared Cole, Michael Marthaler and Alessandro Romito.

I thank Gerd Schön for giving me the opportunity to work as a PhD student at TFP and also for giving me the opportunity to visit numerous conferences and workshops throughout my time as a PhD student. I also thank Alexander Shnirman for agreeing to referee this thesis.

I thank my colleagues at TFP, especially Pei-Qing Jin, Panagiotis Kotetes, Georgo Metalidis and Jens Michelsen, who became very good friends of mine, and who helped and supported me in all kind of things during my time at the institute. Roland Grein gave me many useful hints in the last weeks before the exam. I also thank the secretaries, Evmarie Schwartz and Edith Herzog, for always being helpful.

Chapter 1

Introduction

Superconducting circuits are fascinating objects, since they allow studying the laws of quantum mechanics on a macroscopic scale of typically a few μm. When the circuits are operated at low temperature and sufficiently isolated from the electromagnetic environment, they can be described by few quantum variables, like the electrical charge or the magnetic flux [1].

One interesting application of superconducting circuits is their use as quantum bits (qubits), quantum-mechanical two-level systems for quantum information processing [2]. A necessary condition to realize quantum bits is a non-equidistant energy spectrum, since quantum logical operations should only act in the subspace of the two qubit basis states, without causing transitions to other states [3]. This condition can be fulfilled by using Josephson junctions, which provide a nonlinear, dissipationless electrical element and naturally lead to a non-equidistant energy spectrum of the circuit.

The field of circuit quantum electrodynamics (circuit QED) explores the coupling of superconducting qubits to superconducting microwave resonators. In this context, the qubits are also referred to as "artificial atoms". Circuit QED systems have been investigated for several reasons: On one hand, resonators can be used in quantum information processing to couple superconducting qubits or to provide readout of the qubit state [4]. On the other hand, they allow exploring quantum optics in a new parameter regime, characterized by a strong qubit-resonator coupling and a richer noise spectrum [5].

Superconducting qubits have the advantage that the energy-spacing between the two qubit levels can be easily tuned by external control parameters, like gate voltages or an external magnetic flux. The wide control over the qubit level splitting can be used in experiments to tune qubits in and out of resonance with the resonator and to address individual qubits by an external coherent driving.

Another advantage of superconducting qubits is their macroscopic dipole moment, which naturally leads to a strong coupling between the "atom" and the resonator, allowing for a coherent exchange of excitations between the two systems. The circuit QED architecture has been proposed as a promising candidate for the realization of a quantum computer. In this architecture, the combination of tunability of individual qubits and strong coupling to the resonator is used to build efficient 1- and 2-qubit gates and to provide a readout scheme for the qubits [4].

The measurement of an individual qubit can be performed by detecting the frequency shift of the resonator induced by the qubit. In this context, it is advantageous to use nonlinear microwave resonators including Josephson junctions to obtain a significant increase of the readout contrast. The idea was successfully tested in a number of recent circuit QED experiments and led to the development of the "Josephson bifurcation amplifier" (JBA) [6, 7, 8].

Apart from their use for quantum information processing, circuit QED systems also have been used to investigate the quantum nature of the interaction between matter and light, in analogy to quantum optics experiments with real atoms [5]. Again, the key features in these experiments are the tunability of the artificial atoms and the strong qubit-resonator coupling. To name two examples, the strong coupling allows to clearly resolve the nonlinear energy spectrum of the coupled system [9], while the control over the qubit frequency has been used to generate arbitrary photon states in a resonator [10].

On the other hand, one of the major problems with superconducting circuits is their coupling to the electromagnetic environment, which leads to decoherence of the quantum state and limits the number of coherent operations that can be performed. Due to the macroscopic size of the circuits, decoherence is generally strong and can result from various contributions, like Ohmic (Markovian) noise, slow 1/f noise, or the coupling to two-level fluctuators [11, 12]. Many efforts have been made to reduce the decoherence of superconducting qubits; as an example, microwave resonators can serve as noise filter and enhance the lifetime of qubits [4].

Although in most cases, decoherence is unwanted, the strong coupling to the electromagnetic environment has been used in a recent experiment to obtain an efficient pumping mechanism of a superconducting qubit. This led to the observation of lasing behavior in a microwave transmission line which was strongly coupled to the qubit [13].

In this thesis, we theoretically investigate two different circuit QED systems: the single-qubit laser and the driven nonlinear resonator. In the following, we will shortly discuss the two systems as well as our approach and some main results.

Single-qubit lasing

Lasing behavior in a microwave resonator induced by a single qubit has been observed in 2007 by Astafiev *et al.* [13]. The device used in the experiment, called "artificial-atom maser“, consists of a coplanar waveguide resonator which is capacitively coupled to a charge qubit. The key idea of the experiment was to use an external bias to obtain an incoherent pumping mechanism for the charge qubit and thus to create a population inversion in the two-level-system.

The experiment measured a pronounced increase of the emission power of the resonator around the one-photon-resonance, i.e, for values of the qubit level spacing close to the resonator frequency; this indicates a strong increase of the number of photons in the resonator. Additionally, a narrowing of the emission line was observed, which was taken as a further hint for the electrical field in the resonator being in a lasing-like state.

The experiment successfully demonstrated single-qubit lasing, but also left some open questions. Despite the linewidth narrowing, the emission line was still much broader than expected. Moreover, the emission line showed a Gaussian rather than a Lorentzian shape, which would be expected for a laser. These observations were attributed to the presence of low-frequency charge noise, without however explaining the mechanism of the broadening or providing an estimate for the expected linewidth [13].

In this thesis, we analyze static and spectral properties of single-qubit lasers. In contrast to conventional, many-atom lasers, single-qubit lasers are characterized by a low number of photons in the resonator and by strong coupling between the qubit and the resonator. They operate in a regime where quantum fluctuations of the electrical field become dominant and strongly influence the linewidth of the laser.

We start by investigating the lasing transition. A single-qubit laser can be driven from the non-lasing to the lasing regime by increasing the coupling strength or by decreasing the detuning between the qubit and the resonator. However, there is no sharp lasing threshold like for a many-atom laser, but rather a broad transition region. The fluctuations of the electrical field, which are rather weak deep in the lasing regime, can be relatively large in this transition region.

For our analysis, we use a master equation approach based on the Liouville equation for the reduced density matrix of the qubit and the resonator. In this approach, the coupling to the environment , which includes damping of the resonator and the incoherent pumping of the qubit, is described, within the usual Markov approximation, by dissipation terms for the reduced density matrix. This approach has the advantage that it does not require any further approximations; however, the numerical solution of the Liouville equation is limited by the size of the basis we can handle. Thus, to assure convergence, the average photon number in the resonator must not be too large.

In addition to the master equation approach, we also discuss two approximation schemes, namely the semiclassical and the semiquantum approximation. They provide a good estimate for the average photon number in the resonator, and thus allow us to investigate some basic stationary properties in parameter regimes where the numerical solution can not be applied.

Our main focus is the description of the emission spectrum of a single-qubit laser. We observe that the linewidth depends in a non-monotonous way on the coupling strength between the qubit and the resonator: approaching the lasing transition from weak coupling, we observe the linewidth narrowing which is typical for lasers. However, for stronger coupling the linewidth increases again, and the lasing state deteriorates. Far above the lasing threshold, the linewidth can even become comparable to the bare linewidth of the resonator.

In the lasing regime, the linewidth generally increases with the detuning between the qubit and the resonator; near the lasing transition, the enhancement of the linewidth can become very pronounced. This behavior is due to the amplitude fluctuations of the electrical field, which can be relatively large in the transition region. Approximation schemes like the commonly used phase diffusion model, which neglect the amplitude fluctuations, fail to predict the correct qualitative behavior of the linewidth. The fluctuations also affect the lineshape of the emission spectrum, so that the emission line can deviate from a simple Lorentzian form.

We finally make two extensions to our model. First, we consider the case that the resonator is coupled to several qubits. This allows us to study the scaling behavior of the lasing properties. For increasing numbers of qubits, we observe a sharpening of the lasing transition, so that the system approaches the behavior of a many-atom laser.

In the second extension, we include the effects of low-frequency noise, which can not be treated by means of the usual dissipation terms in the Liouville equation. For certain types of superconducting qubits, like the charge qubit used in the above-mentioned experiment, low-frequency noise is a leading source of decoherence, while its role is suppressed in other devices, like the transmon [14]. Based on a simple model, we show that for realistic parameters, the width and shape of the emission line in the presence of low-frequency noise are determined by the properties of the slow noise and we give an estimate for the resulting linewidth.

The driven nonlinear resonator

A necessary condition for quantum information processing is the possibility to read out the state of individual qubits [15]. Circuit QED offers a readout method for superconducting qubits by coupling them off-resonantly to a microwave resonator and measuring the shift of the resonator frequency. This shift, which depends on the qubit state, can be detected by driving the resonator and measuring the phase of the reflected or transmitted signal [4]. Since the resonator does not lead to transitions of the qubit, this constitutes a quantum non-demolition measurement.

By using Josephson junctions, superconducting resonators can be made nonlinear. Nonlinear resonators have been used in recent circuit QED experiments which were concerned with the development of a Josephson bifurcation amplifier (JBA) to be used as high-contrast readout device for superconducting qubits [6, 7, 8]. JBAs make use of the bistability of coherently driven nonlinear resonators, which leads to the coexistence of two oscillation states of low and high amplitude [16]. In the readout process, the two qubit states are mapped onto the two oscillation states of the driven resonator, which can be easily distinguished, since they differ strongly in amplitude and phase.

Due to thermal and quantum noise, a driven nonlinear resonator can switch between the two oscillation states. When the resonator is locked to low- or high-amplitude oscillations, the noise leads to fluctuations of the amplitude and phase of the electrical field in the resonator. Investigating these fluctuations is an interesting problem, since Josephson junctions allow the engineering of large nonlinearities, and since due to the driving, the resonator is in a non-equilibrium state.

Like in the treatment of single-qubit lasing, we use a master equation approach to describe the dynamics of a driven nonlinear resonator. We investigate the emission spectrum, which yields detailed information about the classical and quantum fluctuations of the resonator. Standard approaches for computing the spectrum are based on a linearization of the equations of motion and predict a sharp peak at the driving frequency due to the coherent driving, accompanied by broad Raman-like side-peaks [17]. The side-peaks are shifted from the sharp peak by the detuning between the driving and the resonator.

Using the numerical solution of the master equation, we show that the large nonlinearities which are typical for circuit QED systems lead to the appearance of two additional, second-order side-peaks, which are not predicted by linearized theories. We also derive an approximative expression for the emission spectrum which relates the side-peaks to transitions between the eigenlevels of the Hamiltonian in the rotating frame, the so called quasi-energy levels.

Using this expression for the spectrum, we see that one of the second-order peaks, shifted by twice the detuning from the driving frequency, results from transitions between next-to nearest quasi-energy levels, which are forbidden for a linear resonator. The other second-order side-peak, located directly at the driving frequency, is a direct consequence of the nonlinear nature of the quasi-energy Hamiltonian.

In the last part of the thesis, we investigate the effects of a two-level-fluctuator (TLF) on a driven nonlinear resonator. TLFs can act as a source of decoherence for superconducting circuits including Josephson junctions [12]; the qualitative difference to a thermal bath results from the fact that the state of the TLF can change due to its interaction with the system.

Recent experimental and theoretical works have investigated the measurement backaction of a driven nonlinear resonator on a two-level-system which is off-resonant with the resonator and has a long coherence time. Here we explore the other limit: the TLF level splitting can be located near the frequency of the resonator, and the TLF relaxation rate can be large.

The behavior of a driven nonlinear resonator can be very sensitive to small changes of the resonance frequency or the temperature. Our goal is here to investigate how the dynamics of the resonator is affected by the coupling to the TLF.

We especially investigate the switching of the resonator from low-to high-amplitude oscillations, which plays a central in the high-contrast readout with JBAs. Solving the master equation for the coupled resonator-TLF system numerically, we show that the coupling to a TLF can increase the switching time by several orders of magnitude. The effect can be qualitatively described by means of an effective temperature and damping, which depend on the parameters of the TLF.

Contents

In the chapters **2**-**4**, we discuss single-qubit lasing; the driven nonlinear resonator is described in the chapters **5** - **7**.

In chapter **2**, we describe the experimental setup that was used to observe single-qubit lasing and derive the Hamiltonian describing the system. We then discuss the master equation approach and show how we can solve it numerically in order to calculate the stationary and spectral properties of a single-qubit laser. Additionally, we present two approximation schemes that lead to analytical expressions for the average photon number.

We discuss the physical properties of a single-qubit laser in chapter **3**. We start by describing the transition between the lasing and non-lasing regime. The main part of the chapter revolves around the emission spectrum. We discuss the behavior of the linewidth as function of the coupling strength and the detuning. In the last part of the chapter, we investigate the shape of the emission line in the lasing transition region.

We then extend our model of the single-qubit laser in chapter **4**: First, we investigate few-qubit lasing. We discuss the scaling of physical quantities with the number of qubits and explain some qualitative differences between a single-qubit laser and a many-atom laser. In the second part of the chapter, we use a simple model to describe the effects of low-frequency noise on the properties of a single-qubit laser. We especially show how the width and the shape of the emission spectrum is affected by slow noise.

In chapter **5**, we shortly describe the basic dynamics of a driven nonlinear resonator and its use as a measurement device. We then derive the Hamiltonian of the system and show how we can describe the system in the frame rotating with the driving frequency, where the Hamiltonian becomes time-independent. We also discuss the use of the master equation to calculate time-dependent properties like the switching time of the resonator.

We discuss the physical properties of driven nonlinear resonators in chapter **6**. We first investigate some stationary properties and the switching from low- to high-amplitude oscillations, which will be useful for the next chapter. We then focus on the emission spectrum of a driven, nonlinear resonator and the appearance of second-order side peaks for strong nonlinearities.

In chapter **7**, we investigate the coupling of a driven nonlinear resonator to a TLF. We derive expressions for the effective temperature and damping of the resonator which are valid for TLFs with a short coherence time. We then focus on the switching rate of the driven resonator from low- to high-amplitude oscillations. We also extend our discussion to the case of a TLF with a longer coherence time.

The thesis contains two appendices with calculations regarding the driven nonlinear resonator that are not carried out in the main part. In App. **A**, we derive an approximative expression for the emission spectrum, which relates the emission peaks to transitions between quasi-energy levels. Finally, in App. **B**, we derive expressions for the effective temperature and damping of a driven resonator in presence of a TLF.

Chapter 2

Single-qubit lasing: Methods

Single-atom lasing in a solid-state environment has been observed for the first time in an experiment performed in 2007 [13]. The lasing behavior was detected in the experiment by measuring an increase of the emission power of the transmission line. Additionally, a reduction of the linewidth was observed, which is a strong hint that the electromagnetic field in the resonator was indeed in a lasing state.

In contrast to a conventional, many-atom laser, a single-qubit laser is characterized by a much lower intensity of the emitted radiation and stronger quantum fluctuations. The major difference to conventional lasers lies in the fact that while in the latter, many atoms are weakly coupled a cavity, in a single-qubit laser one artificial atom is strongly coupled to a two-dimensional resonator [18].

Lasing induced by a single atom has also been observed in quantum optics experiments, where Rydberg atoms were injected into a high-quality cavity [19, 20]. In these single-atom masers, the atoms are pumped to the excited state before entering the cavity, which has a very high quality factor to make lasing possible. On the other hand, The qubit in a single-qubit laser is continuously pumped, and the transmission line has a moderate quality factor, which allows to measure the radiation emitted by the resonator. Also, dissipation on the qubit and the resonator is much stronger. Finally, inhomogeneous broadening caused by slow, non-Markovian noise can strongly influence the qubit-resonator system.

These unique features of a single-qubit laser make it an interesting system to be studied. Due to the strong coupling between the qubit and the resonator, a single-qubit laser can be driven far above the lasing threshold. Another important feature is that the frequency of the qubit can be controlled via a gate voltage, so that the qubit can be tuned away from the resonance. As a consequence, a single-qubit laser can be operated in regimes that were previously not explored.

In this chapter, we start with a short introduction about superconducting qubits and circuit QED and describe the experimental setup used in the single-qubit lasing experiment (Sec. 2.1). We then derive the Hamiltonian for the system (Sec. 2.2). and show in Sec. 2.3 how we can use a master equation approach to calculate static and spectral properties of a single-qubit laser. The method is however numerically demanding and restricted to the regime of not too high average photon number in the resonator, which makes it desirable to have analytical approximations that can be used in certain limits. We therefore describe two approximation schemes in Sec. 2.4: the semiclassical approximation, which neglects all fluctuations, and the semiquantum approximation, which still includes the effects of spontaneous emissions.

2.1 Introduction

2.1.1 Superconducting circuits and circuit QED

Superconducting circuits have attracted much attention in the last decades from numerous experimental and theoretical groups, which attempted to observe and understand the appearance of quantum effects on a macroscopic scale. These efforts led to the experimental observation of macroscopic quantum tunneling [21, 22] and energy quantization [23] in superconducting circuits. Another major breakthrough was the demonstration of superpositions of macroscopically distinct quantum states [24, 25, 26].

One interesting application for these circuits is their potential use for quantum information processing [2]. The nonlinearity of superconducting circuits including Josephson junctions makes it possible to isolate two quantum states and to create a quantum bit, a quantum mechanical two-level system, which in this context is often called “superconducting qubit”. The ultimate goal in the domain of quantum information processing is the building of a quantum computer, working with qubits (quantum bits) instead of classical bits like a conventional computer. A quantum computer could perform tasks that are well beyond the reach of classical computers, like the simulation of quantum systems or the factorization of very large numbers, which plays an important role in cryptography [3].

As pointed out by diVincenzo [15], a physical system must match certain criteria to be considered a candidate for the realization of a quantum computer. For example, it must have a sufficiently long coherence time in order to allow for a large number of coherent manipulations before the phase information is destroyed. Other criteria involve the possibility to couple several qubits and to measure the state of individual qubits. There are currently several physical systems that are promising candidates for the building of a quantum computer, amongst them are superconducting circuits, ion traps, [27, 28], spins in quantum dots [29, 30] and cavity QED systems [31].

Superconducting qubits have the advantage that they can be easily integrated into electrical circuits. This means that their properties, like the energy splitting and the coupling between different qubits, can be tuned by external parameters, e.g., magnetic fluxes or voltages [32]. Furthermore they can be scaled up to large systems. On the other hand, the strong coupling to control parameters also leads to a considerable (unwanted) coupling to the noisy electromagnetic environment. As a consequence, superconducting qubits have rather short coherence times and are heavily influenced by various kinds of noise, like 1/f-noise [11]. In the last years, however, continuous improvement of the circuit designs has helped to substantially increase the coherence times of superconducting qubits [33, 14].

Superconducting qubits are sometimes referred to as “artificial atoms“. In cavity quantum electrodynamics (cavity QED), the quantum nature of the electromagnetic field is probed by investigating the interaction between a real atom and the single mode of a high-quality cavity. Similarly, the field of “circuit QED” investigates the coupling of a superconducting qubit to the single mode of a two-dimensional microwave transmission line, which serves as resonator [4, 5]. Circuit QED experiments take advantage of the macroscopic dipole moment of the qubit as well as the small effective mode volume of the transmission line, which naturally lead to a large coupling strength between qubit and the resonator. In 2004, two experiments were able to reach for the first time in a circuit QED setup the strong coupling regime, which allows for a coherent exchange of excitations between the “atom” and the resonator [34, 35].

Many experiments have investigated the coupling of superconducting qubits with regard to the application in quantum information processing. The circuit QED architecture has been proposed as a promising candidate for the realization of a quantum computer, where resonators are used to build $1-$qubit gates, to couple several qubits and to provide a measurement of the qubits’ state [4, 36]. In the last years, experiments have achieved to use circuit QED setups to realize 2-qubit gates [37, 38, 39], to transfer excitations

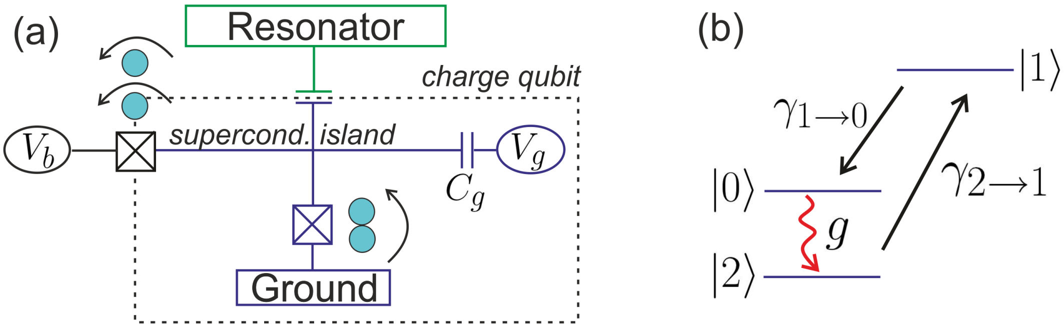

Figure 2.1: The superconducting single-electron transistor- (SSET-) laser. (a) The basic setup: Cooper pairs can tunnel to the island through the lower Josephson junction. If the voltage V_b is high enough, it can break up one Cooper pair and lead to two consecutive single-electron tunneling events. (b) The level structure: If the state $|0\rangle$ has a higher energy than the state $|2\rangle$, the single-electron tunneling corresponds to an incoherent pumping of the charge qubit.

between two qubits [40, 41], and to perform nondestructive readout of the quantum state of qubits [38, 39, 42].

Another class of circuit QED experiments have focused on investigating quantum optics in a previously unexplored parameter regime, characterized by a strong qubit-resonator coupling and strong decoherence. To name just a few examples, the possibility to resolve individual photon number states [43] and the nonlinearity of the energy spectrum [9] in a circuit QED setup were demonstrated, which both showed the quantum nature of the microwave field. Other experiments achieved to generate single microwave photons [44] and, using the wide control over the qubit level splitting and the coupling strength via microwave pulses, to even synthesize arbitrary photon states [10]. In another experiment, which we will describe below, lasing induced by a single artificial atom was observed in a microwave transmission line [13].

2.1.2 Single-qubit lasing

We start by describing the experimental setup used by Astafiev *et al.* in 2007 [13] to demonstrate lasing behavior of a microwave resonator induced by a single qubit. The basic setup is plotted in Fig. 2.1a.

The artificial atom is a charge qubit, a small superconducting island that is connected to the ground by a Josephson junction. The charge qubit works in the charge regime, which is characterized by a single-electron charge energy E_C that is much larger than the Josephson tunneling energy, $E_C \gg E_J$, and the temperature, $E_C \gg k_B T$. This makes the number N of excess charges on the island a good quantum number. The electrostatic energy of the charge states $|N\rangle$ can be controlled by tuning the gate voltage V_g,

$$E_{ch}(N) = E_C \left(N - N_g\right)^2 \tag{2.1}$$

with the single-electron charge energy $E_C = e^2/\left(2C_\Sigma\right)$, where C_Σ is the total capacitance of the superconducting island, and the reduced gate charge $N_g = C_g V_g/e$ [32]. The largest energy scale in the system is the superconducting gap Δ_{sc}, i.e, the energy needed to break up a Cooper pair. This means that charge states with unbound electrons (N odd) have a much higher energy than charge states with only Cooper pairs (N even).

By tuning the gate voltage close to a charge degeneracy point, $N_g \approx 1$, it is possible to operate the device in a regime where the two states $|0\rangle$ and $|2\rangle$, corresponding to 0 or 2 excess electrons on the island (in other words, 0 or 1 excess Cooper pairs), are similar in energy, while all other states have a much higher energy. In this regime, the device can be operated as a proper two-level-system, with the two states being separated by the electrostatic energy $\epsilon_{ch} = E_{ch}(0) - E_{ch}(2) = 4E_C\left(N_g - 1\right)$. The system can make transitions between the two states via the process of Cooper pair tunneling from and to the island through the Josephson junction.

The charge qubit can be operated as a superconducting single electron transistor (SSET) by connecting a drain electrode to the island by a Josephson junction with a high resistance [45, 46]. If the drain voltage is high enough to break up Cooper pairs, $V_b > \left(2\Delta_{sc} + E_C\right)/e$, it can lead to two consecutive single-electron tunneling events in the incoherent process $|2\rangle \to |1\rangle \to |0\rangle$. If the gate voltage is tuned such that the state $|0\rangle$ has a higher electrostatic energy than the state $|2\rangle$, $\epsilon_{ch} > 0$, this corresponds to an incoherent pumping of the qubit, which causes a population inversion.

In the single-qubit lasing setup, the charge qubit is capacitively coupled to a transmission line resonator. When the qubit is in the state $|0\rangle$, it can transfer an excitation to the resonator, i.e., make a coherent transition $|0\rangle \to |2\rangle$ and create a photon in the resonator. The cycle of incoherent pumping to the excited state and coherent transition to the ground state is called the “photon-assisted Josephson quasiparticle cycle and can lead to an accumulation of photons in the resonator, which can be detected via a substantial increase of the emission power of the radiation emitted by the transmission line.

2.2 The Hamiltonian

The system can be described by the Hamiltonian

$$H = -\frac{1}{2}\left(\epsilon_{\mathrm{ch}}\tau_z + E_J\tau_x\right) + \hbar\omega_R a^\dagger a + \hbar g_0\tau_z\left(a + a^\dagger\right) \tag{2.2}$$

where $\tau_z = |2\rangle\langle 2| - |0\rangle\langle 0|$ and $\tau_x = |2\rangle\langle 0| + |0\rangle\langle 2|$ are Pauli operators in the charge basis of the qubit, and $a^{(\dagger)}$ are the creation and annihilation operators for the resonator. The first term describes the electrostatic energy difference between the states $|0\rangle$ and $|2\rangle$ and Josephson tunneling, parametrized by the Josephson energy E_J. The second and third terms describe a single mode of the resonator with frequency ω_R and the capacitive coupling between the qubit and the resonator.

We can now make a unitary transformation to the diagonal basis of the qubit, which leads to the Hamiltonian

$$H = \frac{1}{2}\Delta E\cdot\sigma_z + \hbar\omega_R a^\dagger a + \hbar g_0\left(\cos\zeta\sigma_x - \sin\zeta\sigma_z\right)\left(a + a^\dagger\right), \tag{2.3}$$

where σ_x, z are the Pauli operators in the basis of the qubit eigenstates, and $\Delta E = \sqrt{\epsilon_{\mathrm{ch}}^2 + E_J^2}$ is the energy splitting. The angle ζ is defined via the relation $\tan\zeta = \epsilon_{\mathrm{ch}}/E_J$.

We will assume that the qubit is not too far from resonance with the resonator, $|\Delta E - \omega_R| \ll \omega_R$, and that the coupling is much smaller than the resonator frequency, $g_0 \ll \omega_R$. These conditions are usually fulfilled in circuit QED lasing experiments, since typical values for the coupling strength and the resonator frequency are $g_0 = 10 - 100\mathrm{MHz}$, $\omega_R \sim 5 - 10\mathrm{GHz}$. Also, to observe lasing, the qubit and the resonator must not be too far detuned, so that also the condition $|\Delta E - \omega_R| \ll \omega_R$ will be fulfilled.

These relations allow us to make a Rotating Wave Approximation (RWA): In the Heisenberg picture, and in the absence of coupling, the resonator and qubit operators will show fast oscillations, $a^{(\dagger)}(t) = a^{(\dagger)}(0)\exp\left[\mp i\omega_R t\right]$ and $\sigma_\pm(t) = \sigma_\pm(0)\exp\left[\pm i\Delta E t\right]$, where we introduced the raising and lowering operators $\sigma_\pm = \sigma_x \pm i\sigma_y$ for the qubit.

Within the RWA, we drop all fast oscillating terms $\sim e^{\pm i\omega_R t}$. Defining $g := g_0\cos\zeta$, we can then cast the Hamiltonian in the Jaynes-Cummings form [49]

$$H = \frac{1}{2}\Delta E\cdot\sigma_z + \hbar\omega_R a^\dagger a + \hbar g\left(\sigma_+ a + \sigma_- a^\dagger\right). \tag{2.4}$$

2.3 The master equation approach

The coherent evolution of the system, in absence of dissipation, is described by the Jaynes-Cummings Hamiltonian (2.4). Now we want to include the coupling of the qubit and the resonator to the environment, which manifests itself in the incoherent single-electron tunneling processes for the charge qubit and in incoherent relaxation and excitation processes for the resonator.

In the following subsection, we follow the route described, e.g, in Refs. [47] and [48], to show how we can include the effects of the coupling to the environment into the Liouville equation for the density matrix of the system.

2.3.1 Derivation of the master equation

We consider a system $\mathcal{A}$, which is our system of interest. The environment is modeled by a reservoir $\mathcal{R}$ which has a large number of degrees of freedom and whose macroscopic state is not perturbed by the small system $\mathcal{A}$. The Hamiltonian of the composite system is given by

$$H = H_A + H_R + V. \tag{2.5}$$

where the term V describes the coupling of the system $\mathcal{A}$ to the reservoir.

The Liouville equation for the density matrix of the composite system is given by

$$\frac{d}{dt}\rho(t) = -\frac{i}{\hbar}\left[H, \rho(t)\right], \tag{2.6}$$

with the Hamiltonian (2.5). We now move to the interaction picture with respect to the free Hamiltonian $H_A + H_R$, so that the new density matrix $\tilde{\rho}(t) = e^{i(H_A+H_R)t/\hbar}\rho(t)e^{-i(H_A+H_R)t/\hbar}$ evolves slowly and does not contain the fast free oscillations anymore. By integrating the Liouville equation in the time interval $[t\,,\, t+\Delta t]$, we obtain the equation

$$\tilde{\rho}(t+\Delta t) = \tilde{\rho}(t) - \frac{i}{\hbar}\int_t^{t+\Delta t} dt' \left[\tilde{V}(t'), \tilde{\rho}(t')\right]. \tag{2.7}$$

By iterating this equation, we can expand the expression for the density matrix $\tilde{\rho}$ at time $t+\Delta t$ to second order in the coupling V. In general, we are only interested in the dynamics of the small system $\mathcal{A}$ rather than the dynamics of the composite system. We therefore take the partial trace over the reservoir states, which leads to an equation for the reduced density matrix

$\tilde{\sigma}(t) = Tr_R\{\tilde{\rho}(t)\}$:

$$\begin{aligned}\Delta\tilde{\sigma}(t) &= -\frac{i}{\hbar}\int_t^{t+\Delta t} dt'\, Tr_R\left[\tilde{V}(t'), \tilde{\rho}(t)\right] \\ &\quad -\frac{1}{\hbar^2}\int_t^{t+\Delta t} dt' \int_t^{t'} dt''\, Tr_R\left[\tilde{V}(t'), \left[\tilde{V}(t''), \tilde{\rho}(t'')\right]\right], \qquad (2.8)\end{aligned}$$

where $\Delta\tilde{\sigma}(t) = \tilde{\sigma}(t+\Delta t) - \tilde{\sigma}(t)$ is the variation of the reduced density matrix within the time interval $[t\,,\, t+\Delta t]$.

We will now make several assumptions on the reservoir: first, we will assume that the coupling is linear, $V = -AR$, where A and R are operators of the system and the reservoir, respectively. The central assumption we make now is that the correlation time τ_c of the reservoir, i.e., the timescale on which correlations $\langle R(t')R(t)\rangle$ decay, is very short. Especially, we assume that the correlation time τ_c is short compared to the timescale T_R of the evolution of the reduced density matrix, $\tau_c \ll T_R$.

Based on this assumption, we can factorize the density-matrix of the composite system, $\tilde{\rho}(t) = \tilde{\sigma}(t) \otimes \sigma_R$ in the integrals in Eq. (2.8) if the timestep Δt is much larger than the correlation time τ_c. The justification for this step is that correlations between the system $\mathcal{A}$ and the reservoir decay fast and only lead to small contributions within the time interval $[t\,,\, t+\Delta t]$ [48].

Since the reservoir is unperturbed by the coupling to the small system, we can assume that the reduced density matrix σ_R of the reservoir is constant and describes a stationary state, so that $[H_R, \sigma_R] = 0$. Making these assumptions, the first term (linear in the coupling V) in Eq. 2.8 becomes proportional to the expression $Tr_R\{R\,\sigma_R\}$. This expression is constant in time and can be assumed to be 0. This is not a real restriction, since this condition can be always fulfilled by a redefinition of the system Hamiltonian H_A [48]. As a consequence, only the second term on the right side of Eq. 2.8 remains.

In addition to the first central assumption that the timestep Δt is much larger than the correlation time of the reservoir, we now make a second central assumption, namely that the timestep Δt is much shorter than the timescale T_R of the evolution of the reduced density matrix $\sigma(t)$. This allows us to replace the density matrix $\rho(t'')$ in the second integral of Eq. 2.8 by the density matrix at time at time t, $\rho(t'') \approx \tilde{\sigma}(t) \otimes \sigma_R$, so that we finally obtain the equation

$$\frac{\Delta\tilde{\sigma}}{\Delta t} = -\frac{1}{\hbar^2}\frac{1}{\Delta t}\int_t^{t+\Delta t} dt' \int_t^{t'} dt''\, Tr_R \left[\tilde{V}(t'), \left[\tilde{V}(t''), \tilde{\sigma}(t)\otimes\sigma_R\right]\right] \tag{2.9}$$

This equation now describes a Markovian process, since the time-evolution of the system $\mathcal{A}$ is completely determined by its present state $\tilde{\sigma}(t)$ and does not depend on its state at earlier times $t' < t$.

By inserting the coupling term $\tilde{V}(t) = -\tilde{A}(t)\tilde{R}(t)$, we can rewrite Eq. (2.9) as:

$$\begin{aligned}\frac{\Delta\tilde{\sigma}}{\Delta t} \;=\; & -\frac{1}{\hbar^2}\frac{1}{\Delta t}\int_0^{\Delta t} d\tau \int_{t+\tau}^{t+\Delta t} dt' \,\Big[g(\tau)\tilde{A}(t')\tilde{A}(t'-\tau)\tilde{\sigma}(t)\\ & -g(\tau)\tilde{A}(t'-\tau)\tilde{\sigma}(t)\tilde{A}(t') + g(-\tau)\tilde{\sigma}(t)\tilde{A}(t'-\tau)\tilde{A}(t')\\ & -g(-\tau)\tilde{A}(t)\tilde{\sigma}(t)\tilde{A}(t'-\tau)\Big]\,. \end{aligned} \tag{2.10}$$

Here we see the actual structure of the master equation: The variation rate $\Delta\tilde{\sigma}/\Delta t$ is determined by products of system operators A and the reduced density matrix $\tilde{\sigma}(t)$. The function $g(\tau) = Tr\{\sigma_R\tilde{R}(t')\tilde{R}(t'-\tau)\}$ appearing in the integral is the correlation function of the reservoir, and decays on the timescale τ_c.

The master equation (2.10) relates the matrix elements of the variation $\Delta\tilde{\sigma}_{ab}$ to the matrix elements of the density matrix $\tilde{\sigma}_{cd}$. By projecting the equation on the eigenstates $|i\rangle$ of the system $\mathcal{A}$, we get an equation of the form

$$\frac{\Delta\tilde{\sigma}_{ab}}{\Delta t} = \sum_{c,d} \gamma_{abcd}(t)\, \tilde{\sigma}_{cd}(t). \tag{2.11}$$

By doing a Rotating Wave Approximation (which is also called the secular approximation) in the system-reservoir coupling, we only keep slowly oscillating terms that satisfy the condition $|\omega_{ab} - \omega_{cd}| \ll 1/\Delta t$, where $\hbar\omega_{ij} = E_i - E_j$ is the energy difference between the two eigenstates i, j. Going back to the Schrödinger picture, $\sigma(t) = \exp(-iH_A t)\tilde{\sigma}(t)\exp(iH_A t)$, we then finally obtain a master equation of the form [48]:

$$\frac{d\,\sigma_{ab}(t)}{dt} = -i\omega_{ab}\sigma_{ab}(t) + \sum_{c,d} \mathcal{R}_{abcd}\,\sigma_{cd}(t)\,, \tag{2.12}$$

which is a linear linear differential equation with time-independent coefficients for the elements of the reduced density matrix σ of the system $\mathcal{A}$.

Here, the variation $\Delta\sigma/\Delta t$ of the density matrix has been replaced by the derivative $d\sigma/dt$, which is allowed if we investigate the evolution of the density matrix on a timescale that is much longer than the correlation time of the reservoir.

We close by remarking that in the remainder of this thesis, we will use the usual symbol $\rho(t)$ for the reduced density matrix of the system (instead of the symbol $\sigma(t)$ used in the derivation of the master equation).

2.3.2 Dissipation terms for the resonator and the qubit

As we showed in the previous subsection, the Liouville equation for the density matrix of a system coupled to the environment can be written in the form

$$\dot{\rho} = -\frac{i}{\hbar}\,[H,\rho] + L\,\rho\,, \tag{2.13}$$

where the Hamiltonian H describes the coherent evolution of the system, and the dissipation term $L\rho$ describes the coupling to the environment.

We now come back to our specific system. The Liouville equation we use to describe the coupled qubit-resonator system is given by

$$\dot{\rho} = -\frac{i}{\hbar}\,[H,\rho] + L_{\mathrm{R}}\,\rho + L_{\mathrm{Q}}\,\rho\,. \tag{2.14}$$

Here, H is the Hamiltonian (2.4) derived in Sec. 2.2, and $L_{\mathrm{R,Q}}$ are dissipation terms for the resonator and the qubit, respectively. We mention again that this form of the Liouville equation is only valid for Markovian noise, i.e., noise with a short correlation time. The influence of slow noise will be discussed later in chapter 4.

To describe dissipative processes of the resonator, we use the usual Lindblad terms [47]

$$\begin{aligned} L_{\mathrm{R}}\,\rho = \quad & \frac{\kappa}{2}\,(N_{\mathrm{th}}+1)\left(2a\rho a^{\dagger} - a^{\dagger}a\rho - \rho a^{\dagger}a\right) \\ & +\frac{\kappa}{2}N_{th}\left(2a^{\dagger}\rho a - aa^{\dagger}\rho - \rho aa^{\dagger}\right)\,, \end{aligned} \tag{2.15}$$

which are parametrized by the photon damping rate κ and the thermal photon number $N_{\mathrm{th}} = \left(\exp\left(\hbar\omega_R/k_BT\right) - 1\right)^{-1}$. More precisely, the terms in the first line describe the emission of photons to the environment, while the terms in the second line describe the absorption of photons by the resonator. This can be seen by projecting the equation on the photon number states of the resonator,

$$\begin{aligned}\frac{d}{dt}\langle n\,|\rho|\,n\rangle &= \kappa(N_{\rm th}+1)(n+1)\langle n+1\,|\rho|\,n+1\rangle + \kappa N_{\rm th} n\langle n-1\,|\rho|\,n-1\rangle \\ &- \left[\kappa(N_{\rm th}+1)n + \kappa N_{\rm th}(n+1)\right]\langle n\,|\rho|\,n\rangle\,. \qquad (2.16)\end{aligned}$$

Similarly, we describe the incoherent pumping of the qubit by the Lindblad term [47]

$$L_{\rm Q}\,\rho = \frac{\Gamma_0}{2}\left(2\sigma_-\rho\sigma_+ - \rho\sigma_+\sigma_- - \sigma_+\sigma_-\rho\right)\,. \qquad (2.17)$$

Here we do not specify the detailed mechanism of single-electron tunneling, but simply model it as an incoherent process which causes transitions of the charge qubit from level $|2\rangle$ to level $|0\rangle$ with an effective rate Γ_0.

In order to obtain the Hamiltonian (2.4), we moved to the eigenbasis of the charge qubit. If we apply the same unitary transformation on the Liouville operator $L_{\rm Q}$, we get a sum of three dissipation terms,

$$\begin{aligned}L_{\rm Q}\,\rho &= \frac{\Gamma_\downarrow}{2}\left(2\sigma_-\rho\sigma_+ - \rho\sigma_+\sigma_- - \sigma_+\sigma_-\rho\right) \\ &+ \frac{\Gamma_\uparrow}{2}\left(2\sigma_+\rho\sigma_- - \rho\sigma_-\sigma_+ - \sigma_-\sigma_+\rho\right) \\ &+ \frac{\Gamma_\varphi^*}{2}\left(\sigma_z\rho\sigma_z - \rho\right)\,, \qquad (2.18)\end{aligned}$$

which describe incoherent relaxation and excitation processes with rates $\Gamma_\downarrow = (\Gamma_0/4)\cdot(1-\sin\zeta)^2$ and $\Gamma_\uparrow = (\Gamma_0/4)\cdot(1+\sin\zeta)^2$, as well as pure dephasing processes with a rate $\Gamma_\varphi^* = (\Gamma_0/2)\cdot\cos^2\zeta$. The physical meaning of these rates becomes evident when we project the dissipation terms on the qubit eigenbasis,

$$\begin{aligned}\frac{d}{dt}\langle\downarrow|\rho|\downarrow\rangle &= \Gamma_\downarrow\langle\uparrow|\rho|\uparrow\rangle - \Gamma_\uparrow\langle\downarrow|\rho|\downarrow\rangle \\ \frac{d}{dt}\langle\uparrow|\rho|\uparrow\rangle &= \Gamma_\uparrow\langle\downarrow|\rho|\downarrow\rangle - \Gamma_\downarrow\langle\uparrow|\rho|\uparrow\rangle \\ \frac{d}{dt}\langle\uparrow|\rho|\downarrow\rangle &= -\left[\left(\Gamma_\uparrow+\Gamma_\downarrow\right)/2 + \Gamma_\varphi^*\right]\langle\uparrow|\rho|\downarrow\rangle\,. \qquad (2.19)\end{aligned}$$

If the charge qubit is operated in a regime where $\epsilon_{ch} > 0$, the sine function has positive values, $\sin\zeta > 0$, and the excitation rate becomes larger than the relaxation rate. This shows that the single-electron tunneling leads indeed to an incoherent pumping of the charge qubit.

For later purposes, we also introduce the rate $\Gamma_1 = \Gamma_\downarrow + \Gamma_\uparrow$, which is the sum of excitation and relaxation rates, and $\Gamma_\varphi = \Gamma_1/2 + \Gamma_\varphi^*$, the total dephasing rate, including pure dephasing due to longitudinal noise described by the rate Γ_φ^*. In contrast to relaxation and excitation processes, pure dephasing arises from processes with no energy exchange between qubit and environment and thus does not affect the population of the two qubit states. The parameter $D_0 = (\Gamma_\uparrow - \Gamma_\downarrow)/\Gamma_1$ denotes the stationary qubit polarization in the absence of the resonator. In the regime we consider, $\epsilon_{ch} > 0$, since the excitation rate is larger than the relaxation rate, we have $D_0 > 0$, which corresponds to a population inversion of the qubit.

The master equation approach has been used by several authors to investigate single-qubit lasing [51, 52, 54, 55, 56]. In our case, the specific mechanisms of incoherent pumping of the qubit and of the qubit-resonator coupling are not described explicitly, but only enter by means of the excitation/relaxation rates $\Gamma_{\uparrow,\downarrow}$ and the coupling strength g. This makes the model quite general, so that our results are not restricted to the SSET-laser. Another possible realization is, for example, a coherently driven flux qubit coupled to a low-frequency resonator [52, 53]. However, for the sake of clarity, we will focus here on lasing induced by a SSET.

2.3.3 The numerical solution of the master equation

The dynamics of the single-qubit-laser can be described by a master equation for the density matrix,

$$\dot{\rho} = -\frac{i}{\hbar}[H, \rho] + L_\mathrm{Q}\,\rho + L_\mathrm{R}\,\rho \;= G\,\rho \tag{2.20}$$

with the Jaynes-Cummings Hamiltonian (2.4) and the dissipation terms for the resonator (2.15) and the qubit (2.18). Here we formally introduced the superoperator G acting in the space of the system operators.

After projecting the equation on the basis formed by the product states $|\uparrow,\downarrow\, n\rangle = |\uparrow,\downarrow\rangle \otimes |n\rangle$, where $|\uparrow,\downarrow\rangle$ are the eigenstates of the qubit and $|n\rangle$ the Fock states of the resonator, we can recast the master equation in vector form

$$\dot{\vec{\rho}} = G \cdot \vec{\rho}. \tag{2.21}$$

The density matrix ρ is arranged as a vector $\vec{\rho}$, and the superoperator as a matrix acting on $\vec{\rho}$. This form is convenient for numerically solving the master equation.

The formal time-evolution of the density matrix is described by the equation $\rho(t) = \exp{(Gt)}\,\rho(0)$. Because of the presence of dissipation, after a sufficiently long time, the system will reach a stationary state which does not depend on the initial conditions, $\rho(t) \to \rho_{\mathrm{s}}$ for $t \to \infty$. We call ρ_{s} the stationary density matrix; it can be found by solving the equation

$$\dot{\vec{\rho}}_{\mathrm{s}} = G \cdot \vec{\rho}_{\mathrm{s}} = 0\,, \tag{2.22}$$

which means that we have to calculate the eigenvector of the matrix G corresponding to the eigenvalue $\lambda = 0$. The stationary density matrix gives access to the average value of any system operator $\hat{O}$ in the stationary state, $\langle \hat{O} \rangle = \mathrm{Tr}\{\hat{O}\rho_{\mathrm{s}}\}$, as well as to distribution functions, like the probability $P(n)$ to find n photons in the resonator, $P(n) = \mathrm{Tr}\{|n\rangle\langle n|\, \rho_{\mathrm{s}}\}$.

From the master equation equation (2.20), we can also derive expressions for time-dependent correlation functions [57] $\langle \hat{O}_1(t+\tau)\hat{O}_2(t)\rangle$, where $\hat{O}_{1,2}$ are arbitrary operators in the Heisenberg picture. In order to do so, we employ the quantum regression theorem [50, 47]

$$\langle \hat{O}_1(t+\tau)\hat{O}_2(t)\rangle = \mathrm{Tr}\{\hat{O}_1(0)e^{G\tau}[\hat{O}_2(0)\rho(t)]\}. \tag{2.23}$$

Here we are specifically interested in the field correlation function $\langle a^\dagger(t+\tau)a(t)\rangle$, which we need to calculate the emission spectrum of the resonator. If the system is in the stationary state, we get the following expression for the field correlation function:

$$\langle a^\dagger(t+\tau)a(t)\rangle = \mathrm{Tr}\{a^\dagger e^{G\tau} a\rho_{\mathrm{s}}\}. \tag{2.24}$$

To proceed, it is convenient to diagonalize the superoperator G and to express the product $a\rho_{\mathrm{s}}$ in terms of the eigenvectors of G, $a\rho_{\mathrm{s}} = \sum_k c_k \vec{v}_k$. Acting on the equation with the exponential $\exp(G\tau)$ leads to the expression

$$e^{G\tau} a\rho_{\mathrm{s}} = \sum_k c_k e^{\lambda_k \tau} \vec{v}_k, \tag{2.25}$$

where λ_k is the eigenvalue of G corresponding to the eigenvector $\vec{v}_k$. So once the eigenvalues λ_k and expansion coefficients c_k are known, we can easily obtain the correlation function for all times t. Combining Eqs. (2.24) and (2.25), we get

$$\langle a^\dagger(t+\tau)a(t)\rangle = \sum_k c_k e^{\lambda_k \tau}\, \mathrm{Tr}\{a^\dagger v_k\} = \sum_k \alpha_k e^{\lambda_k \tau} \tag{2.26}$$

by defining the coefficients $\alpha_k = c_k \cdot \mathrm{Tr}\{a^\dagger v_k\}$.

We can solve Eqs. (2.22) and (2.23) numerically using standard linear algebra methods. However, as numerics naturally can only deal with finite matrices, we have to truncate the Hilbert space of the resonator to a finite number N of photon number states. In this case the superoperator G is represented by a $4N^2 \times 4N^2$-matrix, growing fast with N, which limits the method in our case to $N \leq 30$. This puts some constraints to the parameters we can use in our simulations. As will be shown in Sec. 3.1, the average photon number $\langle n \rangle$ in the resonator obeys the relation $\langle n \rangle \lesssim \Gamma_1/(2\kappa)$. Hence the damping rate κ should not be too small, i.e., $\kappa \gtrsim \Gamma_1/N$. On the other hand, for the calculation of average steady state values, which are fully determined by the stationary density matrix ρ_s, the calculations reduce to solving a system of linear equations. In these cases, we can use a much higher number of photon number states, $N \lesssim 200$.

2.4 The semiclassical and semiquantum approximation

The master equation (2.20) allows us to determine completely the quantum state of the system. However, its full solution is numerically demanding in the experimental regime of parameters due to the high number of photons in the resonator (of the order of 10^2 for the SSET-laser). For this reason, we want to discuss different approximation schemes, namely the semiclassical and the semiquantum approximations, to calculate the physical quantities and their range of applicability. As it turns out, we can get good estimates for the average photon number in the resonator as well as for the lasing threshold.

The starting point for both approximation schemes are the equations for the average values, which can be directly obtained from the master equation for the density matrix. In both approaches, we use the factorization of average values to truncate the otherwise infinite hierarchy of moment equations, but the factorization is done on different levels for the semiclassical and the semiquantum approximation.

The semiclassical approximation

Here we start with the equations of motion for the average values $\langle a\rangle$, $\langle\sigma_+\rangle$ and $\langle\sigma_z\rangle$,

$$\begin{aligned}\frac{d}{dt}\langle a\rangle &= -\left(\frac{\kappa}{2}+i\omega_R\right)\langle a\rangle - ig\langle\sigma_-\rangle\,, &(2.27)\\ \frac{d}{dt}\langle\sigma_+\rangle &= -\left(\Gamma_\varphi - i\cdot\Delta E\right)\langle\sigma_+\rangle - ig\langle\sigma_z a^\dagger\rangle, &(2.28)\\ \frac{d}{dt}\langle\sigma_z\rangle &= -2ig\left(\langle\sigma_+ a\rangle - \langle\sigma_- a^\dagger\rangle\right) - \Gamma_1\left(\langle\sigma_z\rangle - D_0\right). &(2.29)\end{aligned}$$

In the semiclassical limit, we completely neglect fluctuations, so that all average values factorize, e.g., $\langle\sigma_+ a\rangle = \langle\sigma_+\rangle\langle a\rangle$. This approximation provides the Maxwell-Bloch equations for the classical variables $\alpha = \langle a\rangle\exp(i\omega_R t)$, $s_\pm = \langle\sigma_\pm\rangle\exp(\mp i\omega_R t)$ and $s_z = \langle\sigma_z\rangle$ [58]:

$$\begin{aligned}\frac{d}{dt}\alpha &= -\frac{\kappa}{2}\alpha - igs_-, &(2.30)\\ \frac{d}{dt}s_+ &= -\left(\Gamma_\varphi - i\Delta\right)s_+ - igs_z\alpha^*, &(2.31)\\ \frac{d}{dt}s_z &= -2ig\left(s_+\alpha - s_-\alpha^*\right) - \Gamma_1\left(s_z - D_0\right). &(2.32)\end{aligned}$$

Here we introduced the detuning $\Delta = \Delta E - \omega_R$ between the qubit and the resonator; by our definitions of the variables α and $s_\pm$ we got rid of the fast oscillations $\sim \exp(i\omega_R t)$. For a single-qubit laser, the dephasing of the qubit is usually much larger than the damping of the resonator, $\Gamma_\varphi \gg \kappa/2$, which means that the qubit variables will evolve much faster than the resonator variable α. This allows us to adiabatically eliminate the qubit's degrees of freedom:

$$\begin{aligned}s_+ &= \frac{-ig}{\Gamma_\varphi - i\Delta}s_z\alpha^*, &(2.33)\\ s_z &= \frac{D_0}{1+|\alpha|^2/\tilde{n}_0}, &(2.34)\end{aligned}$$

where $\tilde{n}_0$ is the photon saturation number, $\tilde{n}_0 = \Gamma_1\Gamma_\varphi/\left(4g^2\right)\cdot\left(1+\Delta^2/\Gamma_\varphi^2\right)$. Inserting these results into the equation for the variable α, we obtain a closed equation of motion:

$$\dot{\alpha} = -\left[\frac{\kappa}{2} - \frac{g^2\Gamma_\varphi}{\Gamma_\varphi^2+\Delta^2}s_z^{st} + i\frac{g^2\Delta}{\Gamma_\varphi^2+\Delta^2}s_z^{st}\right]\cdot\alpha. \qquad (2.35)$$

Here, $s_z^{st} = D_0/\left(1+|\alpha|^2/\tilde{n}_0\right)$ is the stationary population inversion of the qubit.

The stationary solution

We can use Eq. (2.35) to find an equation for the number of photons $\bar{n} = |\alpha|^2$ in the resonator:

$$\dot{\bar{n}} = \dot{\alpha} \cdot \alpha^* + \alpha \cdot \dot{\alpha}^* = - \left[\kappa - \frac{2g^2 \Gamma_\varphi}{\Gamma_\varphi^2 + \Delta^2} \cdot \frac{D_0}{1 + \bar{n}/\tilde{n}_0} \right] |\alpha|^2 . \tag{2.36}$$

In the stationary case, $\dot{\bar{n}} = 0$, we obtain a simple equation for the number of photons:

$$\bar{n}^2 + \left(\tilde{n}_0 - \frac{\Gamma_1 D_0}{2\kappa} \right) \bar{n} = 0. \tag{2.37}$$

In the parameter regime where $\tilde{n}_0 > \Gamma_1 D_0/(2\kappa)$. this equation has only one non-negative solution $\bar{n} = 0$. If the condition $\tilde{n}_0 < \Gamma_1 D_0/(2\kappa)$ is fulfilled, it has one additional non-negative solution $\bar{n} = \Gamma_1 D_0/(2\kappa) - \tilde{n}_0 > 0$, which describes the lasing state. This condition can thus be used to obtain an estimate for the lasing threshold.

The semiquantum approximation

Like the semiclassical approximation, the semiquantum approximation can be derived from the equations of motion for the average values of system operators, but with a different choice of operators [59]. Here we consider the average values of the photon number $\langle n \rangle$, the qubit inversion $\langle \sigma_z \rangle$ and the product $\langle \sigma_+ a \rangle$:

$$\begin{aligned}
\frac{d}{dt}\langle n \rangle &= ig \left(\langle \sigma_+ a \rangle - \langle \sigma_- a^\dagger \rangle \right) - \kappa \left(\langle n \rangle - N_{\text{th}} \right), && (2.38) \\
\frac{d}{dt}\langle \sigma_z \rangle &= -2ig \left(\langle \sigma_+ a \rangle - \langle \sigma_- a^\dagger \rangle \right) - \Gamma_1 \left(\langle \sigma_z \rangle - D_0 \right), && (2.39) \\
\frac{d}{dt}\langle \sigma_+ a \rangle &= - \left(\Gamma_\varphi + \frac{\kappa}{2} - i\Delta \right) \langle \sigma_+ a \rangle - ig \langle \sigma_z n \rangle && (2.40)
\end{aligned}$$

As we are interested in the stationary solution, we can set the left sides of the equations to 0, $d/dt\langle \ldots \rangle = 0$. The equation for the product $\langle \sigma_+ a \rangle$ leads then to the relation $\langle \sigma_+ a \rangle = -ig\langle \sigma_z \rangle / \left(\Gamma_\varphi - i\Delta \right)$, where we used the fact that $\Gamma_\varphi + \kappa/2 \approx \Gamma_\varphi$, since the qubit dephasing is assumed to be much larger than the resonator damping. Inserting this relation into the equations for the average photon number and the qubit inversion then leads then to the following two equations:

$$\langle n\rangle = N_{\rm th} + \frac{2g^2}{\kappa}\frac{\Gamma_\varphi}{\Gamma_\varphi^2+\Delta^2}\left(\langle\sigma_z n\rangle + \frac{1}{2}\left(\langle\sigma_z\rangle+1\right)\right), \tag{2.41}$$

$$\langle\sigma_z\rangle = D_0 - \frac{4g^2}{\Gamma_1}\frac{\Gamma_\varphi}{\Gamma_\varphi^2+\Delta^2}\left(\langle\sigma_z n\rangle + \frac{1}{2}\left(\langle\sigma_z\rangle+1\right)\right). \tag{2.42}$$

By factorizing $\langle\sigma_z n\rangle = \langle\sigma_z\rangle\langle n\rangle$, we obtain a closed set of two equations, which can be turned into a quadratic equation for the average photon number in the resonator:

$$\langle n\rangle^2 + \left(\tilde{n}_0 - \frac{\Gamma_1 D_0}{2\kappa} - N_{\rm th} + \frac{1}{2}\right)\langle n\rangle - \left(N_{\rm th}\tilde{n}_0 + \frac{N_{\rm th}}{2} + \frac{\Gamma_1}{4\kappa}\left(D_0+1\right)\right) = 0 \tag{2.43}$$

This equation has always one single positive solution $\langle n\rangle > 0$. In contrast to the semiclassical theory, the semiquantum approximation contains the effects of spontaneous emission, as expressed by the terms proportional to $(\langle\sigma_z\rangle + 1)$ in Eqs. (2.41) and (2.42). As noticed in Ref. [60], spontaneous emission is especially relevant for the dynamics of single-atom lasers; we will also show that spontaneous emission processes lead to a smoothening of the lasing transition.

Chapter 3

The lasing transition and the emission spectrum

In this chapter we use the master equation approach discussed in chapter 2 to describe the properties of single-qubit lasers. We start by investigating the transition of the system from the non-lasing to the lasing regime. Due to spontaneous emission processes, there is no sharp transition like in conventional lasers, but a transition region, which can be rather broad for strong coupling. This transition is especially interesting for a circuit QED setup, since a single-qubit laser can be easily driven in and out of the lasing regime by tuning the qubit frequency.

In sections. 3.2-3.5, we discuss the emission spectrum of a single-qubit-laser, which can be directly measured in circuit QED experiments [13, 61]. We especially focus on the linewidth, since a very narrow linewidth is one of the typical features of a conventional laser. In a single-qubit laser, due to the presence of only one "atom" and the relatively low photon number, the linewidth is relatively broad. Since the coupling between the qubit and the resonator in circuit QED can become very strong, a single-qubit laser can be driven far above the lasing threshold. In this regime, the emission spectrum shows some interesting features, namely an increase of the linewidth with the coupling strength and a non-monotonous dependence on the detuning between qubit and resonator.

Usually, far above or below the lasing threshold, the emission spectrum of a single-qubit laser is well described by a Lorentzian curve. However, for strong qubit-resonator-coupling, the spectrum can show a deviation from the simple Lorentzian shape in vicinity of the lasing transition. This is discussed in Sec. 3.6.

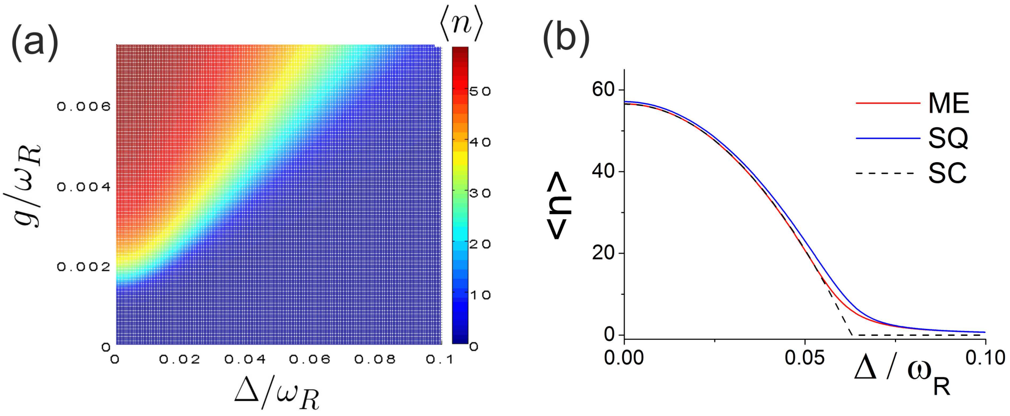

Figure 3.1: (a) Average photon number $\langle n \rangle$ in the resonator as function of the coupling strength g and the detuning Δ. (b) Average photon number as function of the detuning for a fixed coupling strength $g/\omega_R = 5 \times 10^{-3}$, calculated by using the master equation (ME), the semiclassical approximation (SC) and the semiquantum approach (SQ). The other parameters are $\Gamma_1/\omega_R = 2.5 \times 10^{-2}$, $D_0 = 0.975$, $\Gamma_\varphi^*/\omega_R = 5 \times 10^{-3}$, $\kappa = 2 \times 10^{-4}$, and $N_{\text{th}} = 0$.

3.1 The lasing transition

In this section we investigate the stationary properties of single-qubit lasers for different values of the qubit-resonator coupling g and the detuning Δ, while the other parameters, like the bare qubit inversion or the resonator damping rate, are kept constant. We also assume zero temperature, $N_{\text{th}} = 0$ throughout the chapter. The detuning is the parameter which can usually be easily changed in circuit QED experiments and which can be used in a single-qubit laser to cross the lasing transition. On the other hand, depending the coupling strength, a single-qubit laser can be operated in a regime just slightly above the lasing threshold (for moderate coupling) or deep in the lasing regime (for strong coupling). We will see in later sections that especially the spectral properties of single-qubit-laser depend strongly on the coupling strength.

In Fig. 3.1a, we plot the average photon number $\langle n \rangle$ in the resonator as a function of the coupling strength g and the detuning Δ. Fig. 3.1b shows a cut through the plane $g/\omega_R = 5 \times 10^{-3}$ and displays the results obtained by the numerical solution of the master equation as well as the results from the semiclassical and semiquantum approximations. At large detuning, the average photon number is rather low; this is the non-lasing regime. When the detuning is decreased, at a certain point the average photon number will show a pronounced increase, as the system undergoes a transition to the lasing state.

The curve $\langle n(\Delta)\rangle$ runs smoothly between the lasing and non-lasing regime, which means that there is no sharp boundary between the two regimes; the change of behavior rather occurs in a certain range of the detuning; in the following, we will refer to this region of the parameter space as the transition region. The smoothening of the curve $\langle n(\Delta)\rangle$ is a consequence of spontaneous emission processes, i.e., of transitions of the qubit from the excited state to the ground state in absence of photons in the resonator [62, 63, 64].

We see that the semiquantum approximation gives quite accurate results, even in the transition region, since spontaneous emission is accounted for in this approach. We will therefore use it later in Sec. 4.2 for the discussion of few-qubit-lasing. The predictions from the semiclassical theory also coincide well with the numerical results for small and large detuning. On the other hand, the semiclassical approach predicts a sharp transition between the lasing and the non-lasing regime.

While it does not give an accurate description of the average photon number, it can still be used to obtain a good estimate for the location of the transition region. From Eq. (2.37) and the condition $\tilde{n}_0 < \Gamma_1 D_0/(2\kappa)$ we obtain the expression

$$\Delta_{\mathrm{thr}} = \Gamma_\varphi \sqrt{\frac{2g^2 D_0}{\kappa\Gamma_\varphi} - 1} \tag{3.1}$$

for the detuning at which the transition occurs.

We will in the following refer to this value as the lasing threshold. As confirmed by Fig. 3.1, the value Δ_{thr} grows with the coupling strength. In order to reach the lasing regime, the coupling between the qubit and the resonator has to exceed a certain value. The semiclassical equations predict the relation

$$g > \sqrt{\frac{\kappa\Gamma_\varphi}{2D_0}} \tag{3.2}$$

as the condition to obtain lasing behavior at the full resonance ($\Delta = 0$).

A further insight to the behavior of the system can be obtained by looking at the photon distribution function $P(n) = \langle n\,|\rho_{\mathrm{s}}|\,n\rangle$ and the Fano factor $F = \left(\langle n^2\rangle - \langle n\rangle^2\right)/\langle n\rangle$. Fig. 3.2a shows the function $P(n)$ for fixed coupling strength and different values of the detuning. For large detuning, below the lasing threshold, the distribution is simply a Bose distribution, and, since $N_{\mathrm{th}} = 0$, the Fano factor equals 1. For small detuning, in the lasing

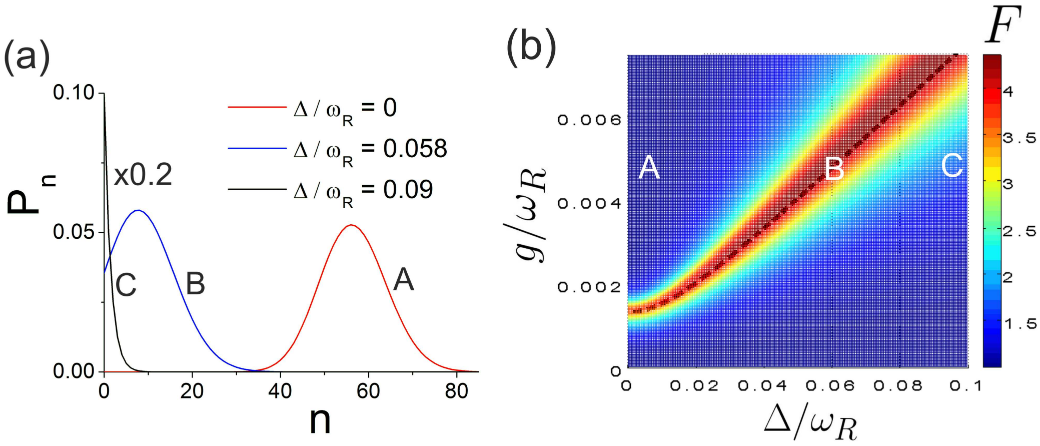

Figure 3.2: (a) The photon distribution function $P(n)$ for 3 values of the detuning and a fixed coupling strength $g/\omega_R = 5 \times 10^{-3}$. (b) The Fano Factor F as function of the coupling strength and the detuning. The 3 points A, B, C correspond to the values used in the plot of the distribution functions. Other parameters like in Fig. 3.1.

regime, the resonator field is in a coherent state, characterized by a Poisson distribution, also with Fano Factor $F = 1$.

Around the lasing transition however, due to large fluctuations in the photon number, the Fano factor is strongly enhanced. This is demonstrated in Fig. 3.2b, which shows the Fano factor as function of the coupling strength and the detuning. There is a wide region in the (Δ, g)-plane where F is significantly larger than 1. In this region, the resonator field is not yet in a coherent state. The Fano factor is thus a useful quantity for describing the position and the width of the transition region.

We observe that for increasing coupling, the transition region is significantly broadened. We also plotted the semiclassical lasing threshold and observe that it coincides well with the maximum of the Fano factor. This demonstrates that the semiclassical lasing threshold can be used to obtain an accurate estimate of the position of the lasing transition even in the strong coupling regime, where quantum effects become important.

Average photon number and fluctuations

In. Fig. 3.3a we plot the average value $\langle n \rangle$ and the fluctuations $\Delta n = \sqrt{\langle n^2 \rangle - (\langle n \rangle)^2}$ of the photon number in the resonator as functions of the coupling strength g. We also show the semiclassical lasing threshold, as defined by Eq. (3.2). We observe that for strong coupling, deep in the lasing

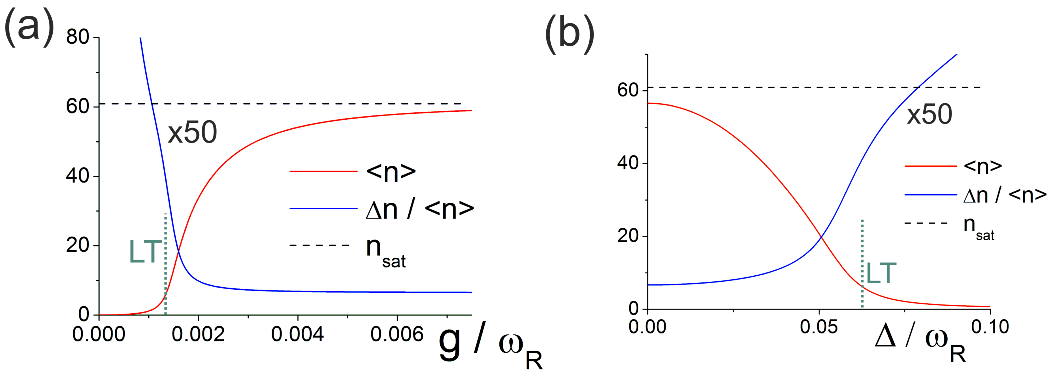

Figure 3.3: (a) Average photon number $\langle n \rangle$ and relative fluctuations $\Delta n/\langle n \rangle$ as functions of the coupling strength g at full resonance ($\Delta = 0$). (b) Average photon number $\langle n \rangle$ and fluctuations $\Delta n/\langle n \rangle$ as functions of the detuning Δ for fixed coupling $g/\omega_R = 5 \times 10^{-3}$. In both plots, we also show the semiclassical lasing threshold (LT) and the saturated photon number $\bar{n}_{\text{sat}}$. Other parameters like in Fig. 3.1.

regime, the average photon number and the fluctuations saturate. We can find an estimate for the asymptotic value of $\langle n \rangle$ by looking at the semiclassical solution $\bar{n} = \Gamma_1 D_0/(2\kappa) - \tilde{n}_0 > 0$; for large coupling, the parameter $\tilde{n}_0$ becomes very small, so that the average photon number approaches the value

$$\bar{n}_{\text{sat}} = \frac{\Gamma_1 D_0}{2\kappa}. \tag{3.3}$$

Fig. 3.3b shows a similar plot for fixed coupling strength $g/\omega_R = 5 \times 10^{-3}$ and variable detuning.

The relative fluctuations $\Delta n/\langle n \rangle$ will be of interest in the following sections about the emission spectrum. Above the lasing threshold, they become quite small, as expected for the lasing state, but still stay finite. Although they are weak, they have important effects on the linewidth, as will be discussed. We also see that in the lasing transition region, the average photon number can be relatively large, while the relative fluctuations are still quite strong. We will show that especially in this regime, we can observe interesting effects like a strong increase of the linewidth and a non-Lorentzian shape of the emission spectrum.

3.2 The emission spectrum: Introduction

In the following, we will investigate the emission spectrum of single-qubit lasers. There is a twofold interest in the emission spectrum: First, it is a quantity which can be directly measured in experiments, like demonstrated for the SSET-laser [13]. Therefore it is interesting to see which kind of information about the system is contained in the characteristics of the emission spectrum, like the linewidth or the lineshape.

Secondly, a very narrow linewidth is one of the typical features of the lasing state for a conventional, many-atom laser. On the other hand, a single-qubit laser works in a completely different parameter regime. In the previous section we have showed that the stationary properties, like the average photon number, saturate in the lasing regime of a single-qubit-laser. As we will show, this is not the case for the linewidth, which shows a strong dependence on the coupling strength and the detuning. Investigating the linewidth allows us to further characterize the state of the system above the lasing threshold, e.g., by showing that strong coupling increases the linewidth and thus leads to a deterioration of the lasing state.

The emission spectrum $S(\omega)$ is given by the Fourier transform of the correlation function $\langle a^\dagger(t+\tau)a(t)\rangle$,

$$S(\omega) = 2\mathrm{Re}\int_0^\infty dt\, e^{-i\omega\tau}\langle a^\dagger(t+\tau)a(t)\rangle \tag{3.4}$$

Using Eq. (2.26), we directly get the following expression for the emission spectrum:

$$\begin{aligned} S(\omega) &= 2\mathrm{Re}\sum_k \frac{\alpha_k}{i\omega - \lambda_k} \\ &= 2\sum_k \frac{-\mathrm{Re}(\alpha_k)\mathrm{Re}(\lambda_k) + \mathrm{Im}(\alpha_k)[\omega - \mathrm{Im}(\lambda_k)]}{[\mathrm{Re}(\lambda_k)]^2 + [\omega - \mathrm{Im}(\lambda_k)]^2}, \end{aligned} \tag{3.5}$$

where we decomposed the eigenvalues λ_k of the superoperator G and the coefficients α_k into their real and imaginary parts.

Integrating the spectrum $S(\omega)$ over the whole frequency range leads to the equation

$$\int_{-\infty}^{\infty} S(\omega)d\omega = 2\pi\,\mathrm{Re}\sum_k \alpha_k = 2\pi\,\mathrm{Re}\langle a^\dagger(t)a(t)\rangle = 2\pi\langle n\rangle, \tag{3.6}$$

which means that the surface below the spectral curve $S(\omega)$ is proportional to the average photon number in the resonator.

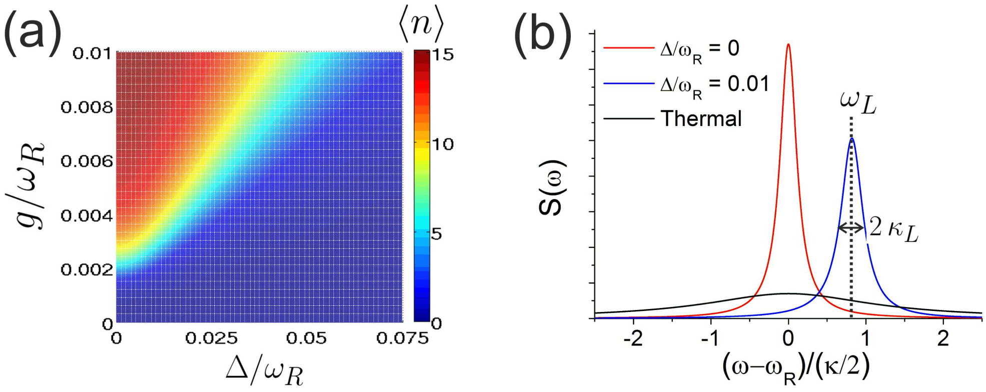

Figure 3.4: (a) Average photon number $\langle n \rangle$ in the resonator as function of the coupling strength g and the detuning Δ. (b) Emission Spectrum $S(\omega)$ for two different values of the detuning and a fixed coupling strength $g/\omega_R = 4 \times 10^{-3}$. For comparison we also show the spectrum of a thermal distribution with the same average photon number as the lasing state for $\Delta = 0$. The other parameters are $\Gamma_1/\omega_R = 1.6 \times 10^{-2}$, $D_0 = 0.975$, $\Gamma^*_\varphi/\omega_R = 4 \times 10^{-3}$, $\kappa = 5 \times 10^{-4}$, and $N_{\text{th}} = 0$.

In Fig. 3.4, we plot the emission spectrum $S(\omega)$ for different values of the detuning. As we mentioned in the previous chapter, diagonalizing the superoperator is numerically much more demanding than the calculation of the stationary density matrix. For this reason, we have to restrict the number of photon number states used in the numerics; in our case we use a basis of $N = 30$ photon number states. To ensure convergence, we have to make sure that the average photon number $\langle n \rangle$ stays much smaller than N. This is done by choosing a larger value for the resonator damping rate κ and a smaller value for the qubit pumping rate Γ_1.

The red line in Fig. 3.4 shows the emission spectrum in the lasing state for zero detuning, while the black line shows the spectrum for a thermal distribution. By comparing the two curves, we see a clear narrowing of the emission peak in the lasing regime, as expected. The blue line show the spectrum for the case that qubit and resonator are off-resonant, but still in the lasing regime. We see that the peak is shifted away from the natural frequency ω_R of the resonator; we also observe a slight broadening of the spectrum.

Once we have calculated the emission spectrum for a certain set of parameters, we can extract the linewidth κ_L, which we define as the half width at half maximum (HWHM) of the emission peak [65], as well as the frequency shift $\delta\omega_R = \omega_L - \omega_R$. The discussion in sections 3.3-3.5 focuses on these two quantities. In Sec. 3.6 we also investigate the lineshape.

3.3 The emission spectrum: Dependence on the coupling strength

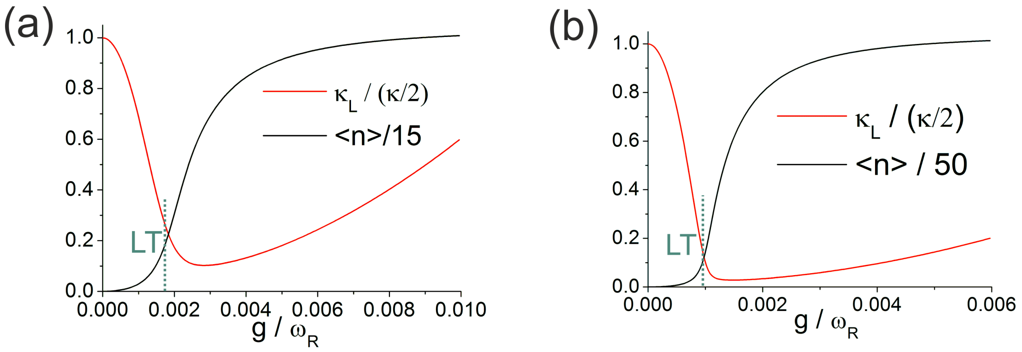

Figure 3.5: (a) Average photon number $\langle n \rangle$ and linewidth κ_L as functions of the coupling strength at full resonance ($\Delta = 0$) for a damping rate $\kappa/\omega_R = 5 \times 10^{-4}$. (b) Average photon number $\langle n \rangle$ and linewidth κ_L as functions of the coupling strength at full resonance ($\Delta = 0$) for a smaller damping rate $\kappa/\omega_R = 1.5 \times 10^{-4}$. In the picture (b), the linewidth was calculated by using Eq. (3.12). Other parameters like in Fig. 3.4.

Fig. 3.5a shows the linewidth κ_L and the average photon number $\langle n \rangle$ at full resonance (detuning $\Delta = 0$) as functions of the coupling strength between the qubit and the resonator. We see that, while the photon number rapidly increases at the lasing transition and then saturates, the linewidth shows a non-monotonic behavior. For increasing but still weak coupling we observe the linewidth narrowing which is typical for lasers. However, in the lasing regime, the linewidth grows again with coupling strength, leading to a deterioration of the lasing state.

In Sec. 3.6 we will show that at resonance, $\Delta = 0$, generally only a single eigenvalue λ contributes to the spectrum, so that Eq. (3.5) simplifies to $S(\omega) = 2\kappa_L \langle n \rangle / \left([\omega - \omega_R]^2 + \kappa_L^2 \right)$, where we used the relation $\langle a^\dagger(t) a(t) \rangle = \langle n \rangle = \alpha$. In this case, the height of the emission peak is given by the ratio

$$S_{\max} = S(\omega = \omega_R) = \frac{2\langle n \rangle}{\kappa_L}. \tag{3.7}$$

By looking at Fig. 3.5a, we note that in the transition region there is an "optimal" value of the qubit-oscillator coupling where the height of the spectral line is maximum. This interesting feature is due to the fact that in single-qubit lasers far above the lasing transition an increase of the coupling has little effect on the average photon number, but leads to a pronounced increase of the linewidth. This means that, in order to obtain the sharpest emission curve, a single-qubit-laser should be operated slightly above the lasing threshold.

Fig. 3.5b shows again the linewidth and the average photon number as functions of the coupling strength, but this time for a smaller damping rate κ, which leads to a larger value of the saturated photon number $\bar{n}_{sat}$ and a smaller value of the lasing threshold. Because of the high average photon number, we cannot perform a diagonalization of the superoperator anymore; we therefore make use of an approximation scheme which can be used for zero detuning, $\Delta = 0$, and which will be discussed below.

By comparing both plots in Fig. 3.5, we see that the minimum linewidth, slightly above the lasing threshold, diminishes for a decreasing damping rate. This behavior is similar to the case of conventional, many-atom lasers, where the linewidth in the lasing regime is inversely proportional to the intensity, $\kappa_L^{\text{many-atom}} \sim 1/\bar{n}$ [65]. For large resonator damping κ, the linewidth is relatively large and, above threshold, quickly grows and can even become larger than the bare linewidth of the resonator, $\kappa_L > \kappa_L|_{g=0} = \kappa/2$.

In this regime of strong coupling and large damping, the single-qubit laser is still in a state characterized by a photon distribution function $P(n)$ with a maximum around $n \approx \langle n \rangle$ (see Fig. 3.2, red curve) and which clearly differs from a thermal distribution with an monotonically decreasing function $P(n)$. So the state of resonator can be identified as a lasing state. On the other hand, the system is lacking one of the typical features of a conventional laser, namely the linewidth narrowing.

3.4 Approximation schemes for the linewidth and the frequency shift

Like we mentioned before, the calculation of the spectrum is numerically very demanding, since it requires a diagonalization of the superoperator G. For this reason, it would be helpful to use a factorization scheme like the semiclassical or the semiquantum approach that we described earlier and that we used for the discussion of the average photon number. However, for the case of the spectrum, this is generally not possible, since correlations play an important role and a factorization thus may lead to qualitatively wrong results.

Still, we can derive an expression for the linewidth κ_L which gives accurate results in the case of zero detuning between the qubit and the resonator, $\Delta = 0$, and which only depends on the average values $\langle n\rangle$, $\langle \sigma_z\rangle$ and $\langle \sigma_z n\rangle$. We also obtain an expression for the frequency ω_L around which the emission peak is centered and which can be used for a wide range of parameters. Additionally, our results will help us to discuss the role of quantum fluctuations in later sections.

We start by writing down the equations of motion for the correlation functions $\langle \tilde{a}^\dagger(t+\tau)\tilde{a}(t)\rangle$ and $\langle \tilde{\sigma}_+(t+\tau)\tilde{a}(t)\rangle$, where we defined $\tilde{a} = a \cdot e^{i\omega_R t}$ and $\tilde{\sigma}_+ = \sigma_+ \cdot e^{-i\omega_R t}$. Using the quantum regression theorem [47], we obtain:

$$\begin{aligned} \frac{d}{d\tau}\langle \tilde{a}^\dagger(t+\tau)\tilde{a}(t)\rangle &= -\frac{\kappa}{2}\langle \tilde{a}^\dagger(t+\tau)\tilde{a}(t)\rangle + ig\langle \tilde{\sigma}_+(t+\tau)\tilde{a}(t)\rangle, \qquad (3.8) \\ \frac{d}{d\tau}\langle \tilde{\sigma}_+(t+\tau)\tilde{a}(t)\rangle &= -\left(\Gamma_\varphi - i\Delta\right)\langle \tilde{\sigma}_+(t+\tau)\tilde{a}(t)\rangle \\ &\quad -ig\langle \sigma_z(t+\tau)\tilde{a}^\dagger(t+\tau)\tilde{a}(t)\rangle. \qquad (3.9) \end{aligned}$$

Since in a single-qubit laser the qubit decoherence is much larger than the resonator damping rate, $\Gamma_\varphi \gg \kappa/2$, we can adiabatically eliminate the qubit, i.e., using Eq. (3.9), make the approximation $\langle \tilde{\sigma}_+(t+\tau)\tilde{a}(t)\rangle \approx -ig/\left(\Gamma_\varphi - i\Delta\right)\langle \sigma_z(t+\tau)\tilde{a}^\dagger(t+\tau)\tilde{a}(t)\rangle$. Inserting this result into Eq. (3.8) leads to the new equation

$$\frac{d}{d\tau}\langle \tilde{a}^\dagger(t+\tau)\tilde{a}(t)\rangle = -\frac{\kappa}{2}\langle \tilde{a}^\dagger(t+\tau)\tilde{a}(t)\rangle + \frac{g^2}{\Gamma_\varphi - i\Delta}\langle \sigma_z(t+\tau)\tilde{a}^\dagger(t+\tau)\tilde{a}(t)\rangle. \qquad (3.10)$$

This equation is not closed however; in order to close it, we have to factorize the correlation function $\langle \sigma_z(t+\tau)\tilde{a}^\dagger(t+\tau)\tilde{a}(t)\rangle$.

Separation of phase and amplitude

The finite linewidth of a single-qubit-laser results from the fact that, while the amplitude of the electrical field in the resonator is rather well defined, its phase is not fixed, but diffuses. This means that the phase information gets lost after a certain time $t_L \sim 1/\kappa_L$, leading to the decay of the field correlation function $\langle \tilde{a}^\dagger(t+\tau)\tilde{a}(t)\rangle$ on this timescale and to a finite width κ_L of the emission line. On the other hand, Fig. 3.3 shows that the fluctuations Δn of the average photon number, and thus the fluctuations of the field amplitude are rather small in the lasing state, $\Delta n/\langle n\rangle \ll 1$.

In our derivation of an expression for the linewidth we will now make the central assumption that amplitude and phase fluctuations are not coupled. The procedure is described in Ref. [62] and leads to the following factorization scheme:

$$\langle\sigma_z(t+\tau)\tilde{a}^\dagger(t+\tau)\tilde{a}(t)\rangle \simeq \frac{1}{2}\left(\langle\sigma_z\rangle + \frac{\langle\sigma_z n\rangle}{\langle n\rangle}\right)\langle\tilde{a}^\dagger(t+\tau)\tilde{a}(t)\rangle \tag{3.11}$$

The factorization leads to a closed equation for the field correlation function, $d/d\tau\langle\tilde{a}^\dagger(t+\tau)\tilde{a}(t)\rangle = -\left(\kappa_L^{\mathrm{fac}} - i\delta\omega_L^{\mathrm{fac}}\right)\langle\tilde{a}^\dagger(t+\tau)\tilde{a}(t)\rangle$, where κ_L^{fac} and $\delta\omega_L^{\mathrm{fac}}$ are defined by

$$\begin{aligned} \kappa_L^{\mathrm{fac}} &= \frac{\kappa}{2} - \frac{g^2\Gamma_\varphi}{\Gamma_\varphi^2+\Delta^2}\cdot\frac{1}{2}\left(\langle\sigma_z\rangle + \frac{\langle\sigma_z n\rangle}{\langle n\rangle}\right), & (3.12)\\ \delta\omega_L^{\mathrm{fac}} &= \frac{g^2\Delta}{\Gamma_\varphi^2+\Delta^2}\cdot\frac{1}{2}\left(\langle\sigma_z\rangle + \frac{\langle\sigma_z n\rangle}{\langle n\rangle}\right). & (3.13) \end{aligned}$$

Our approximations predict a Lorentzian spectrum

$$S(\omega) = \frac{2\kappa_L^{\mathrm{fac}}\langle n\rangle}{\left(\kappa_L^{\mathrm{fac}}\right)^2 + \left(\omega - \left[\omega_R + \delta\omega_L^{\mathrm{fac}}\right]\right)^2} \tag{3.14}$$

with a linewidth κ_L, and which is centered around the frequency $\omega = \omega_R + \delta\omega_L^{\mathrm{fac}}$.

Finally, in analogy to the semiquantum approach discussed in Sec. 2.4, we can factorize the correlator $\langle\sigma_z n\rangle \approx \langle\sigma_z\rangle\langle n\rangle$ to obtain the even simpler expressions

$$\kappa_L^{\mathrm{SQ}} = \frac{\kappa}{2} - \frac{g^2\Gamma_\varphi}{\Gamma_\varphi^2+\Delta^2}\langle s_z^{\mathrm{SQ}}\rangle, \qquad \delta\omega_L^{\mathrm{SQ}} = \frac{g^2\Delta}{\Gamma_\varphi^2+\Delta^2}\langle s_z^{\mathrm{SQ}}\rangle \tag{3.15}$$

where s_z^{SQ} is the average value of the operator σ_z obtained by solving the equations (2.42) and (2.41) within the semiquantum approach.

Discussion

In Fig. 3.6a we compare the linewidth obtained by three methods: by diagonalizing the superoperator, by using Eq. (3.12), and by using Eq. (3.15). We see that the linewidth κ_L^{fac} provides quite accurate results, and it can thus be used in parameter regimes that are not accessible with our standard method, i.e, when the average photon number is too large.

Using Eq. (2.41), for zero detuning, the expression for κ_L^{fac} can be cast in the form

$$\kappa_L^{\mathrm{fac}} = \frac{\kappa}{2}\frac{N_{\mathrm{th}}}{\langle n\rangle} + \frac{g^2}{\Gamma_\varphi}\frac{\langle\sigma_z\rangle+1}{2\langle n\rangle} + \frac{g^2}{\Gamma_\varphi}\frac{\langle\sigma_z n\rangle - \langle\sigma_z\rangle\langle n\rangle}{2\langle n\rangle} \tag{3.16}$$

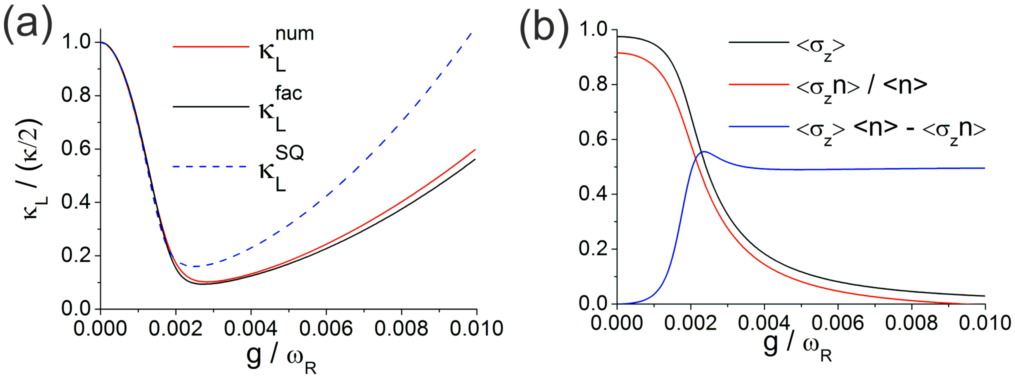

Figure 3.6: (a) Comparison of the linewidth obtained by diagonalizing the superoperator (κ_L^{num}), by using Eq. (3.12) (κ_L^{fac}) and by using Eq. (3.15) (κ_L^{SQ}). (b) Comparison of $\langle\sigma_z\rangle$ and the ratio $\langle\sigma_z n\rangle/\langle n\rangle$. The detuning is zero, $\Delta = 0$, other parameters like in Fig. 3.4.

As wee see in Fig. 3.6b, the correlations $\langle\delta\sigma_z\,\delta n\rangle \equiv \langle\sigma_z n\rangle - \langle\sigma_z\rangle\langle n\rangle$ can be of order 1, $\langle\delta\sigma_z\,\delta n\rangle \sim \mathcal{O}(1)$, so that the third term in Eq. (3.16) is of comparable size as the second term. This explains the quantitative differences between the linewidth κ_L^{SQ} calculated via the semiquantum approach and the numerical result in Fig. 3.6a. On the other hand, the semiquantum approach still provides the correct qualitative behavior, the main difference being a constant factor 1/2 between the numerical and approximative result in the lasing regime.

The semiquantum result overestimates the linewidth, so that $\kappa_L^{\mathrm{num,lasing}}|_{\Delta=0} \approx 1/2 \cdot \kappa_L^{\mathrm{SQ,lasing}}|_{\Delta=0}$. In the deep lasing regime, the qubit inversion approaches 0, $\langle\sigma_z\rangle \approx 0$. For zero temperature, $N_{\mathrm{th}} = 0$, we then obtain the following estimate for the linewidth at resonance:

$$\kappa_L^{\mathrm{lasing}}|_{\Delta=0} \approx \frac{1}{2} \cdot \frac{g^2}{\Gamma_\varphi} \cdot \frac{1}{2\langle n\rangle} \approx \frac{g^2\kappa}{2\Gamma_1\Gamma_\varphi D_0}, \tag{3.17}$$

which clearly demonstrates the quadratic increase of the linewidth with the coupling strength g.

We should note that this method for calculating the linewidth only works at full resonance, $\Delta = 0$. Using an approach based on a Fokker-Planck equation for the resonator, it can be shown that amplitude and phase fluctuations are indeed decoupled for $\Delta = 0$ [64]. On the other hand, in the off-resonant situation, they are not decoupled, and, more importantly, this coupling can not be neglected, so that our approximation would lead to qualitatively wrong results.

The general difficulty with factorization schemes relies on the fact that the qubit inversion $\langle\sigma_z\rangle$ tends to 0 above the lasing threshold, as shown in Fig. 3.6b. This means that correlations, e.g., $\langle\delta\sigma_z\,\delta n\rangle$, can become large and generally can not be neglected. On the other hand, below threshold correlations are quite small, so that there all approaches are in very good agreement.

3.5 The emission spectrum: Dependence on the detuning

In the following, we investigate the dependence of the spectral properties on the detuning Δ between the qubit and the resonator. This corresponds to the usual situation in circuit QED experiments, where the qubit frequency can be tuned easily. We should note that typically also the coupling strength g and the dissipation rates for the qubit depend on the qubit frequency. For the case of the SSET-laser, this can be seen from the Hamiltonian (2.4) and the dissipation terms (2.18), which all depend on the angle ζ. However, the dependence of these quantities on the qubit frequency leads to rather small effects compared to the change of the detuning itself; for this reason, we will assume them to be constant throughout the chapter.

As stated in the introduction and as shown in Fig. 3.4b, the detuning will not only affect the linewidth of the emission peak, but also shift the peak away from the natural frequency ω_R of the resonator . We will start by discussing the frequency shift before we turn our discussion to the dependence of the linewidth on the detuning.

The frequency-shift

Here we investigate the frequency shift $\delta\omega_L = \omega_L - \omega_R$, i.e., the difference between the frequency ω_L at which the emission peak reaches its maximum value, and the natural frequency ω_R of the resonator. Fig. 3.7a shows the frequency shift $\delta\omega_L = \omega_L - \omega_R$ of the emission peak as function of the detuning for different values of the coupling strength g. We observe that near the full resonance, the frequency shift grows linearly with the detuning and does not depend on the coupling strength. We also observe that the frequency shift increases until the system reaches the lasing transition, and then decreases monotonically.

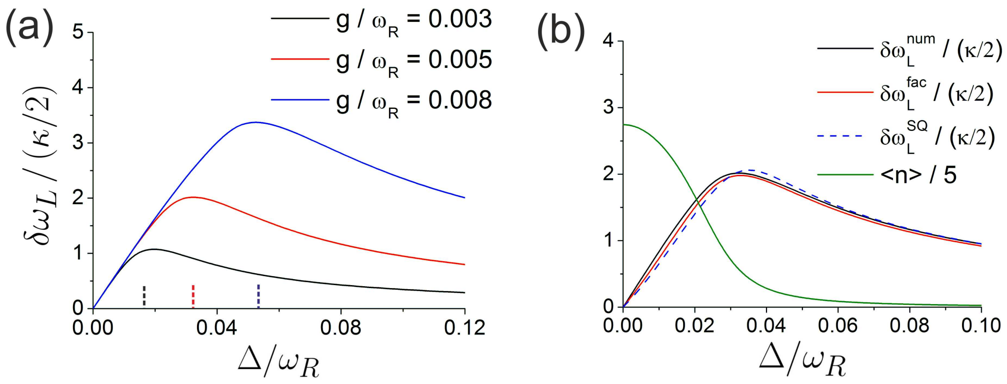

Figure 3.7: (a) Frequency shift $\delta\omega_L$ as function of the detuning for different values of the coupling strength g. The dashed lines mark the position of the lasing threshold. (b) Comparison of the frequency shift for a fixed coupling strength $g/\omega_R = 0.005$, obtained by diagonalizing the superoperator ($\delta\omega_L^{\text{num}}$), by using Eq. (3.13) ($\delta\omega_L^{\text{fac}}$) and by using Eq. (3.15) ($\delta\omega_L^{\text{SQ}}$). Other parameters like in Fig. 3.4.

In Fig. 3.7b we compare different methods to calculate the frequency shift, namely the diagonalization of the superoperator, the factorization scheme presented in Sec. 3.4, and the semiquantum approximation. We see that there is a good agreement between all results.

Using Eq. (2.41), the approximative expression (3.13) for the frequency shift can be cast in the following form for zero temperature, $N_{\text{th}} = 0$:

$$\delta\omega_L^{\text{fac}} = \frac{\Delta\kappa}{2\Gamma_\varphi} - \frac{g^2\Delta}{\Gamma_\varphi^2 + \Delta^2}\frac{\langle\sigma_z\rangle + 1}{2\langle n\rangle} + \frac{g^2\Delta}{\Gamma_\varphi^2 + \Delta^2}\frac{\langle\sigma_z n\rangle - \langle\sigma_z\rangle\langle n\rangle}{2\langle n\rangle} \tag{3.18}$$

In the lasing regime, if the coupling strength is not too strong, $g < \Gamma_\varphi$, the first term is larger than the other 2 terms, and we get the simple estimate

$$\delta\omega_L^{\text{lasing}} \approx \frac{\Delta\kappa}{2\Gamma_\varphi}, \tag{3.19}$$

which confirms that the frequency shift increases linearly with the detuning around the resonance and does not depend on the coupling strength. Furthermore, as the second and third term are rather small, the error made by factorization $\langle\sigma_z n\rangle = \langle\sigma_z\rangle\langle n\rangle$ is also quite small, which explains the good working of the semiquantum approach even in the lasing regime.

In the non-lasing regime, for large detuning, we can approximate $\langle\sigma_z\rangle = D_0$ and, based on the semiquantum approach, obtain the simple expression $\delta\omega_L \approx g^2\Delta D_0/\left(\Gamma_\varphi^2 + \Delta^2\right) \approx g^2 D_0/\Delta$. So, below the lasing threshold, the

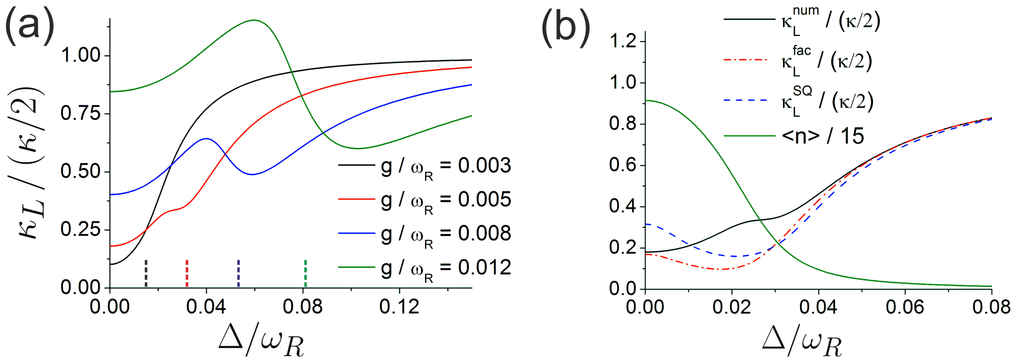

Figure 3.8: (a) The linewidth κ_L as function of the detuning for different values of the coupling strength g. The dashed lines mark the position of the lasing threshold. (b) Comparison of the linewidth for a fixed coupling strength $g/\omega_R = 0.005$, obtained by diagonalizing the superoperator (κ_L^{num}), by using Eq. (3.12) (κ_L^{fac}) and by using Eq. (3.15) (κ_L^{SQ}). Other parameters like in Fig. 3.4.

frequency shift is proportional to g^2 and inversely proportional to the detuning.

The linewidth

We now turn our discussion to the linewidth. Fig. 3.8a shows the linewidth κ_L as function of the detuning for different values of the coupling strength g. Around the full resonance, $\Delta = 0$, all curves show a quadratic increase of the linewidth with the detuning Δ.

It is interesting to compare the numerical data with the results obtained within the factorization scheme discussed in Sec. 3.4; this is done in Fig. 3.8b. We see that the factorization method predicts the wrong behavior around the resonance, namely a decrease of the linewidth with detuning rather than an increase. The biggest quantitative differences between the exact and approximative results are reached around the lasing transition. On the other hand, below the lasing threshold, for large detuning, the approximations are valid; based on the semiquantum result (3.15), we can get the estimate $\kappa_L \approx \kappa/2 - g^2\Gamma_\varphi D_0/(\Gamma_\varphi^2 + \Delta^2)$ for the linewidth of the emission peak in the non-lasing regime.

In Ref. [64] it has been shown that the failing of the factorization scheme in the off-resonant lasing regime is due to the coupling between phase and amplitude fluctuations. As mentioned before, the finite linewidth is a consequence of fluctuations of the phase of the electrical field in the resonator. In our approximation, we made the assumption that phase and amplitude fluctuations are decoupled. But in Ref. [64] it was demonstrated, using a Fokker-Planck equation approach, that the dynamics of phase and amplitude are coupled and that the coupling increases linearly with the detuning Δ. On resonance, this coupling vanishes, which means that the approximation is valid. On the other hand, in off-resonance, the amplitude fluctuations of the electrical field, although being relatively small, qualitatively influence the linewidth and can thus not be neglected.

In Fig. 3.8a we see that for relatively small values of the coupling strength, $g/\omega_R = 0.003$, the linewidth increases monotonically with the detuning. For stronger coupling strength, $g/\omega_R = 0.005$, we observe some structure in the lasing transition. Finally, for even stronger coupling, $g/\omega_R = 0.008$, the linewidth shows a non-monotonic dependence on the detuning in the transition region: Starting from the far-off-resonant regime, reducing the detuning first leads to a reduction of the linewidth; this is well described by the equation $\kappa_L \approx \kappa/2 - g^2\Gamma_\varphi D_0/(\Gamma_\varphi^2 + \Delta^2)$, valid in the non-lasing case. But as the detuning is further reduced and the system enters the lasing regime, the linewidth shows a pronounced increase. Finally, outside the lasing transition region, a reduction of the detuning lowers the linewidth, which then approaches its value at resonance, $\kappa_L(\Delta = 0) \sim \kappa_L^{\mathrm{SQ}} \approx g^2\kappa/\left(\Gamma_1\Gamma_\varphi\right)$.

Again, the counter-intuitive enhancement of the linewidth around the lasing transition is a consequence of the coupling of phase and amplitude fluctuations. In Fig. 3.3 we have shown that the relative amplitude fluctuations $\delta n/\langle n\rangle$ are decreasing when the system enters the lasing regime and the average photon number increases. The absolute fluctuations δn however get larger and contribute to the diffusion of the phase, thus enhancing the linewidth.

In Ref. [64] it was shown that the coupling v between phase and amplitude near the lasing transition has the form $v \sim a_1\langle n\rangle/\bar{n}_{\mathrm{sat}}$ with the coefficient

$$a_1 = \frac{\sqrt{4\xi - 1}}{4\xi}\left(1 + \xi\right), \quad \xi = \frac{g^2}{\kappa\Gamma_1}. \tag{3.20}$$

These expressions show that the coupling between phase and amplitude fluctuations increases with the coupling strength. This is confirmed by the plot of the linewidth in Fig. 3.8a. For very large coupling strength, $g/\omega_R = 0.012$, the linewidth around the lasing transition even becomes larger than the bare linewidth of the resonator.

So far we only discussed the case of positive detuning, $\Delta > 0$. But all results can be generalized to negative values of the detuning: The numerical results show that both the linewidth and the frequency shift are symmetric in the detuning:

$$\kappa_L(-|\Delta|) = \kappa_L(|\Delta|)\,, \qquad \delta\omega_L(-|\Delta|) = -\delta\omega_L(-|\Delta|). \tag{3.21}$$

Condition for non-monotonic behavior of the linewidth

Here we want to discuss the condition to find a non-monotonic dependence of the linewidth as function of the detuning, like observed for coupling strengths $g/\omega_R = 0.008$ and $g/\omega_R = 0.012$ in Fig. 3.8. One sufficient condition is that the linewidth just below the lasing threshold is smaller than the linewidth at zero detuning (see Fig. 3.8). As the linewidth increases quadratically around the resonance, this means that there will be a non-monotonic behavior in the lasing transition region. For simplicity, we will assume $D_0 = 1$ and $N_{\mathrm{th}} = 0$ in the following.

The linewidth just below the lasing threshold can be calculated using the semiquantum approach. At the lasing threshold, $\Delta = \Delta_{\mathrm{thr}}$, Eq. (2.43) simplifies to $\langle n\rangle^2 + 1/2\langle n\rangle - \bar{n}_{\mathrm{sat}}$ with the solution $\langle n\rangle = -1/4 + 1/2\sqrt{\bar{n}_{\mathrm{sat}} + 1/16}$. Since the qubit pumping rate Γ_1 is assumed to be much larger than the resonator damping rate κ, we can approximate:

$$\langle n\rangle|_{\mathrm{thr}} \approx \sqrt{\bar{n}_{\mathrm{sat}}} \tag{3.22}$$

Using the expression (3.15) for the linewidth below the lasing threshold and the relation $\langle\sigma_z\rangle = D_0 - \langle n\rangle/\bar{n}_{\mathrm{sat}}$, we obtain the following estimatefor the linewidth just below the lasing threshold:

$$\kappa_L^{\mathrm{below-thr}} \approx \frac{\kappa}{2}\frac{1}{\sqrt{\bar{n}_{\mathrm{sat}}}}. \tag{3.23}$$

For an estimate of the linewidth $\kappa_L|_{\Delta=0}$ at full resonance, we can use Eq. (3.17). The condition $\kappa_L|_{\Delta=0} > \kappa_L^{\mathrm{below-thr}}$ then leads to

$$g^2 > \Gamma_\varphi\sqrt{2\Gamma_1\kappa}. \tag{3.24}$$

For the set of parameters used in the plots, i.e., $\Gamma_1/\omega_R = 1.6\times10^{-2}$, $\Gamma_\varphi/\omega_R = 1.2\times10^{-2}$ and $\kappa/\omega_R = 5\times10^{-4}$, we obtain the condition $g > 6.9\times10^{-3}$, which is consistent with our results shown in Fig. 3.8.

3.6 Non-Lorentzian lineshape

In the previous sections we investigated the width and position of the emission peak. Here we want to investigate whether the spectrum can be described by a simple Lorentzian curve or whether it has a more complicated form.

Relative weight of different eigenvalues

The general expression for the emission spectrum reads:

$$S(\omega) = 2\mathrm{Re}\sum_k \frac{\alpha_k}{i\omega - \lambda_k} \tag{3.25}$$

We should note that all eigenvalues λ have a negative real part, since a positive real part would lead to an exponential growth of the correlation function $\langle a^\dagger(t+\tau)a(t)\rangle$ and thus be unphysical. In the simplest case, only one term, corresponding to the eigenvalue whose real part is closest to zero, (denoted as λ_1), contributes to the spectrum. In this case, the correlation function $\langle a^\dagger(t+\tau)a(t)\rangle$ decays exponentially, and the emission spectrum has a Lorentzian form. In the general case however, more than one eigenvalue will contribute to the sum. To investigate the deviation of the spectrum from a Lorentzian form, we order the eigenvalues λ_i with respect to their real part (starting with the smallest real part) and calculate the relative weight

$$W_i = \frac{|\alpha_i|^2}{\sum_k |\alpha_k|^2} \tag{3.26}$$

of the eigenvalue λ_i in the sum (3.25).

Fig. 3.9a-c shows the weight of the first eigenvalues $\lambda \neq \lambda_1$ as function of the detuning for different values of coupling strength. We observe that the weight of these eigenvalues is very small around the full resonance and for large detuning. This means that deep in the lasing regime and below the lasing threshold, the spectrum is well described by a single eigenvalue λ_1 and has a Lorentzian form. On the other hand, the weight of the additional eigenvalues reaches its maximum value slightly above the lasing threshold, i.e, in the transition region.

For not too strong coupling, $g/\omega_R = 5 \times 10^{-3}$, the weight of the second eigenvalue λ_2 is still relatively small, and the other eigenvalues can be neglected. For stronger coupling however, the weight W_2 of the second eigenvalue can become quite large. There is even a significant contribution from the third eigenvalue λ_3.

In Fig. 3.9d-f we plot the real part of the first eigenvalues. For a coupling strength $g/\omega_R = 0.008$, we see that there is a point where the difference between the real parts of the eigenvalues λ_2 and λ_3 becomes small. This

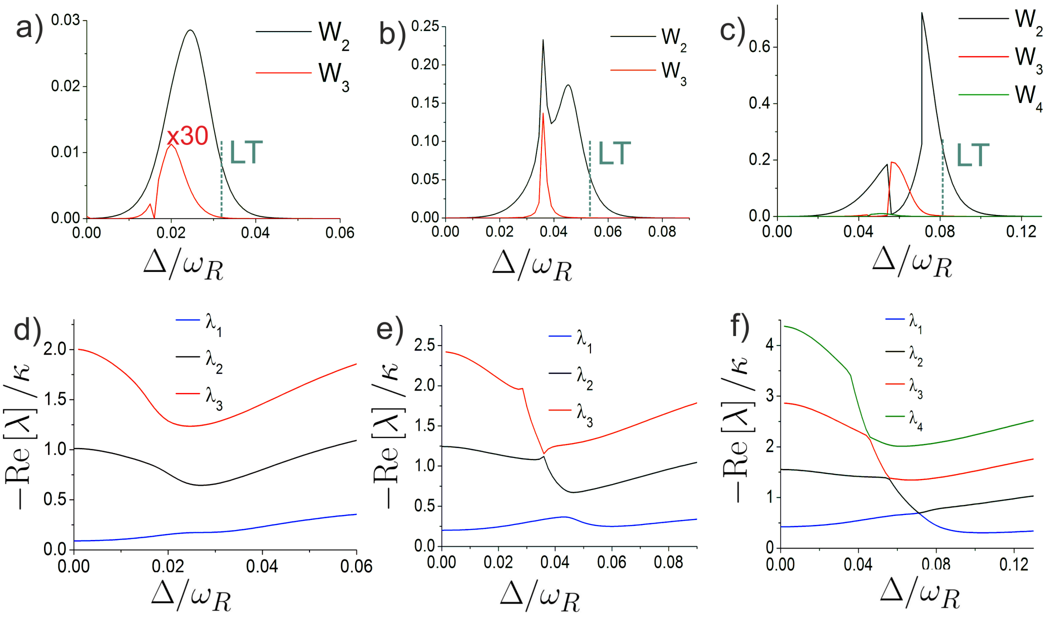

Figure 3.9: Top row: Relative weight of the eigenvalues as function of the detuning for different values of the coupling strength (a: $g/\omega_R = 5 \times 10^{-3}$, b: $g/\omega_R = 8 \times 10^{-3}$, c: $g/\omega_R = 12 \times 10^{-2}$). The dashed lines mark the position of the lasing threshold. Bottom row: Real part of the eigenvalues as function of the detuning for different values of the coupling strength (d: $g/\omega_R = 5 \times 10^{-3}$, e: $g/\omega_R = 8 \times 10^{-3}$, f: $g/\omega_R = 1.2 \times 10^{-2}$). Other parameters like in Fig. 3.4.

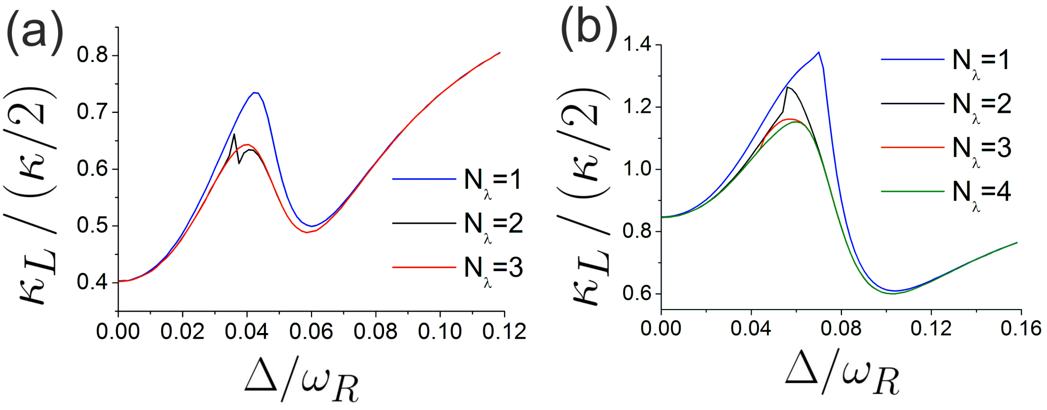

Figure 3.10: Linewidth of the spectrum obtained by only including N_λ eigenvalues in the sum (3.25) as function of the detuning (a) for a coupling strength $g/\omega_R = 8 \times 10^{-3}$ and (b) for a coupling strength $g/\omega_R = 1.2 \times 10^{-2}$. Other parameters like in Fig. 3.4.

is the region where the eigenvalue λ_3 gives a significant contribution to the spectrum.

This behavior becomes more pronounced for even stronger coupling strength, $g/\omega_R = 1.2 \times 10^{-2}$. In this regime, the largest contribution to the spectrum can come from the eigenvalue λ_2. Again, this happens in the lasing transition region, where the spectrum is characterized by a strong increase of the linewidth, as discussed in the previous chapter. Looking at the real parts of the eigenvalues, as shown in Fig. 3.9f, we also see that there are now several points where the curves touch. At these points, the weight of the additional eigenvalues becomes quite large.

Consequences for the spectrum

Our results hint at the fact that we need to include several eigenvalues in our calculation to obtain the correct results for the spectrum in all parameter regimes. The use of the smallest eigenvalue λ_1 alone would provide accurate results deep in the lasing regime and below the lasing threshold, but not in the lasing transition region. To demonstrate this, we truncate the sum (3.25) by only including a fixed number N_λ of eigenvalues:

$$S_{N_\lambda} = 2\mathrm{Re}\sum_{k=1}^{N_\lambda} \frac{\alpha_k}{i\omega - \lambda_k} \tag{3.27}$$

and then calculate the linewidth of the spectrum S_{N_λ}.

The results are shown in Fig. 3.10. For strong coupling, $g/\omega_R = 8 \times 10^{-3}$, we see that there are important quantitative differences between the different lines in the lasing transition region. Including only the smallest eigenvalue would lead to overestimating the linewidth. To obtain a good agreement with the numerical result (where we include all eigenvalues) for all values of the detuning, we would have to include at least the first 3 eigenvalues. On the other hand, deep in the lasing regime and below the lasing threshold, we get the expected result that already the smallest eigenvalue λ_1 describes the linewidth very well, since the weight $W_{i\neq 1}$ of the other eigenvalues is quite small.

For stronger coupling, $g/\omega_R = 1.2 \times 10^{-2}$, the quantitative difference between the smallest eigenvalue and the exact linewidth becomes even bigger. As we see, we need to include at least 4 eigenvalues in this case for the results to converge. Also, the parameter space where the eigenvalue λ_1 is not sufficient to provide the correct linewidth, becomes larger.

Deviation from a Lorentzian lineshape

We are now interested in obtaining a measure on how much the spectrum deviates from a simple Lorentzian form. For this, we recall that for a Lorentzian spectrum, $S(\omega) = 2\text{Re}\{\alpha/\left(i\omega - \lambda\right)\}$, the linewidth is given by $\kappa_L = -\text{Re}\lambda$, and the spectrum reaches its maximum value at the frequency $\omega_L = \text{Im}\lambda$. This leads to the following relations:

$$S_{\max} = S(\omega = \omega_L) = S(\omega = \text{Im}\,\lambda) = 2\frac{\text{Re}\,\alpha}{-\text{Re}\,\lambda} = \frac{2\langle n\rangle}{\kappa_L}, \tag{3.28}$$

This equation relates the maximum value of the spectrum with the linewidth and the average photon number, which itself is proportional to the surface below the spectral curve (see Eq. (3.6)).

We can now define a rate $\bar{\kappa}_L$:

$$\bar{\kappa}_L := \frac{2\langle n\rangle}{S(\omega_L)}, \tag{3.29}$$

which can be obtained by calculating the average photon number $\langle n\rangle$ and the frequency-shift $\delta\omega_L = \omega_L - \omega_R$ of the spectrum for a fixed set of parameters. If the spectrum is Lorentzian, the rate $\bar{\kappa}_L$ is equal to the linewidth; in the general case however, the two rates can be different. We now define the quantity γ as the relative distance between the two rates,

$$\gamma := \frac{|\bar{\kappa}_L - \kappa_L|}{\kappa_L}. \tag{3.30}$$

In Fig. 3.11 we plot γ as function of the detuning for different values of the coupling strength g. The curves confirm our earlier results: Around the full resonance, $\Delta = 0$, the parameter γ increases and reaches its maximum value slightly above the semiclassical lasing threshold, in the lasing transition region. For even larger detuning, it decreases again and tends to 0, like expected for the far off-resonant, non lasing regime. We also see that the deviation between the rates $\bar{\kappa}_L$ and κ_L increases with the coupling strength.

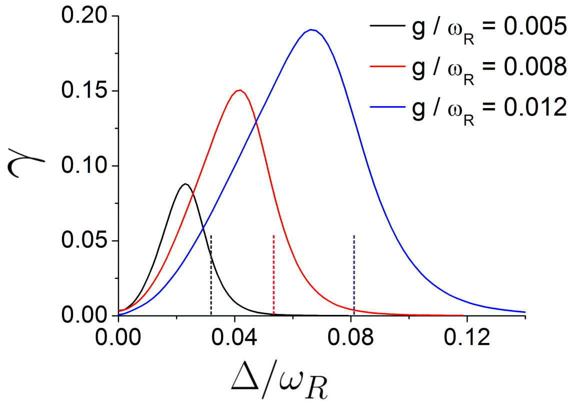

Figure 3.11: Relative distance γ between the rates $\bar{\kappa}_L$ and κ_L as function of the detuning for different values of the coupling strength g. The dashed lines mark the position of the lasing threshold. Other parameters like in Fig. 3.4.

Chapter 4

Few-qubit lasing and effects of slow noise

In this chapter, we generalize the model presented in the previous chapter. In Secs. 4.1 and 4.2, we consider the case of several qubits that are coupled to one resonator. We generalize the semiclassical and semiquantum equations from chapter 2 and use them to discuss the scaling of the lasing properties with the number N_q of qubits. Especially, going to large numbers N_q allows us to understand some of the qualitative differences between a single-qubit laser and a many-atom laser. Using a master equation approach, we can determine the stationary density matrix for the case of a small number of qubits ($N_q \leq 4$) and investigate qubit-field and qubit-qubit-correlations.

In Sec. 4.3 we introduce a simple model to include the effects of low-frequency noise for a single-qubit laser. Low-frequency noise has been shown to be present in many kinds of superconducting circuits [66, 67, 68], and can strongly affect the coherence properties of superconducting qubits. However, since it is non-Markovian, it can not be treated by the usual Lindblad dissipation terms. Here, we will use the assumption that the correlation time of the noise is larger than the typical timescale of the system. We then discuss the effects of slow noise on the emission spectrum in Sec. 4.4.

4.1 Few-qubit lasing: Methods

We generalize the Hamiltonian (2.4) in order to describe N_q qubits coupled to a resonator,

$$H = \hbar\omega_R a^\dagger a + \frac{1}{2}\Delta E \cdot \sum_{\mu=1}^{N_q} \sigma_z^\mu + \hbar g \sum_{\mu=1}^{N_q} \left(\sigma_+^\mu a + \sigma_-^\mu a^\dagger\right) . \tag{4.1}$$

We label the different qubits by using the index μ. Similarly, we generalize the dissipation terms (2.18) to the case of N_q qubits:

$$\begin{aligned} L_{\mathrm{Q}}\,\rho &= \sum_{\mu=1}^{N_q}\left[\frac{\Gamma_\downarrow}{2}\left(2\sigma_-^\mu\rho\sigma_+^\mu-\rho\sigma_+^\mu\sigma_-^\mu-\sigma_+^\mu\sigma_-^\mu\rho\right)\right. \\ &\quad+\frac{\Gamma_\uparrow}{2}\left(2\sigma_+^\mu\rho\sigma_-^\mu-\rho\sigma_-^\mu\sigma_+^\mu-\sigma_-^\mu\sigma_+^\mu\rho\right) \\ &\quad\left.+\frac{\Gamma_\varphi^*}{2}\left(\sigma_z^\mu\rho\sigma_z^\mu-\rho\right)\right]. \end{aligned} \tag{4.2}$$

In general, the qubit frequency, the coupling strength and the dissipation rates can be different for every qubit. In order to get analytical results however, we have to assume them to be equal for all qubits. On the other hand, in a fully numerical approach based on the master equation, this restriction does not have to be made, so that we can also treat the most general case.

The semiclassical approximation

We write down the semiclassical equations for the variables $\alpha=\langle a\rangle\exp\left(i\omega_R t\right)$, $s_\pm^\mu=\langle\sigma_\pm^\mu\rangle\exp\left(\mp i\omega_R t\right)$ and $s_z^\mu=\langle\sigma_z^\mu\rangle$:

$$\frac{d}{dt}\alpha = -\frac{\kappa}{2}\alpha-ig\sum_\mu s_-^\mu, \tag{4.3}$$

$$\frac{d}{dt}s_+^\mu = -\left(\Gamma_\varphi-i\Delta\right)s_+^\mu-igs_z^\mu\alpha^*, \tag{4.4}$$

$$\frac{d}{dt}s_z^\mu = -2ig\left(s_+^\mu\alpha-s_-^\mu\alpha^*\right)-\Gamma_1\left(s_z^\mu-D_0\right). \tag{4.5}$$

Repeating the steps described in Sec. 2.4, we obtain the following equation for the variable α:

$$\dot\alpha=-\left[\frac{\kappa}{2}-\frac{g^2N_q\Gamma_\varphi}{\Gamma_\varphi^2+\Delta^2}s_z^{st}+i\frac{g^2N_q\Delta}{\Gamma_\varphi^2+\Delta^2}s_z^{st}\right]\cdot\alpha\,, \tag{4.6}$$

with the photon saturation number $\tilde n_0=\Gamma_1\Gamma_\varphi/\left(4g^2N_q\right)\cdot\left(1+\Delta^2/\Gamma_\varphi^2\right)$ and the stationary qubit population inversion $s_z^{st}=D_0/\left(1+\left|\alpha\right|^2/\left(\tilde n_0N_q\right)\right)$.

The next step is to calculate the average photon number $\bar n=\left|\alpha\right|^2$. This can be done in the same way as shown in Sec. 2.4 for the case of a single qubit. It is now convenient to introduce the scaled photon number $\tilde n=\left|\alpha\right|^2/N_q$, i.e., the average photon number per qubit. This yields the equation:

$$\tilde n^2+\left(\tilde n_0-\frac{\Gamma_1D_0}{2\kappa}\right)\tilde n=0, \tag{4.7}$$

which is identical to the equation (2.37) that we derived for a single-qubit laser. Again, the threshold condition reads $\tilde{n}_0 < \Gamma_1 D_0/(2\kappa)$, and the scaled photon number above the lasing threshold is given by $\tilde{n} = \Gamma_1 D_0/(2\kappa) - \tilde{n}_0 > 0$.

From these first results we can see that a few-qubit laser, where N_q qubits are coupled to a resonator with coupling strength g, will be characterized by the same scaled photon number as a single-qubit laser with an effective coupling strength $g\sqrt{N_q}$. This means for example that the minimal coupling strength to obtain a lasing state decreases with the number of qubits. On the other hand, the average photon number increases linearly with the number of qubits, $\langle n\rangle = N_q \cdot \tilde{n}$.

The semiquantum approximation

In our discussion of the single-qubit laser we have seen that the semiclassical approach is useful to obtain an estimate for the lasing threshold, while the semiquantum approach can used to calculate the average photon number with a good accuracy.

The equations for the average values $\langle n\rangle$, $\langle\sigma_z^\mu\rangle$ and $\langle\sigma_+^\mu a\rangle$ are given by:

$$
\begin{aligned}
\frac{d}{dt}\langle n\rangle &= ig\sum_\mu \left(\langle\sigma_+^\mu a\rangle - \langle\sigma_-^\mu a^\dagger\rangle\right) - \kappa\left(\langle n\rangle - N_{\text{th}}\right), && (4.8)\\
\frac{d}{dt}\langle\sigma_z^\mu\rangle &= -2ig\left(\langle\sigma_+^\mu a\rangle - \langle\sigma_-^\mu a^\dagger\rangle\right) - \Gamma_1\left(\langle\sigma_z^\mu\rangle - D_0\right), && (4.9)\\
\frac{d}{dt}\langle\sigma_+^\mu a\rangle &= -\left(\Gamma_\varphi - i\Delta\right)\langle\sigma_+^\mu a\rangle - ig\langle\sigma_z^\mu n\rangle - ig\sum_\nu\langle\sigma_+^\mu\sigma_-^\nu\rangle && (4.10)
\end{aligned}
$$

Again, we can eliminate the products $\langle\sigma_+^\mu a\rangle$ to obtain equations for the average photon number $\langle n\rangle$ and the mean qubit inversion $\langle S_z\rangle = \left(\sum_\mu\langle\sigma_z^\mu\rangle\right)/N_q$:

$$
\begin{aligned}
\langle n\rangle &= N_{\text{th}} + \frac{2g^2N_q}{\kappa}\frac{\Gamma_\varphi}{\Gamma_\varphi^2+\Delta^2}\left(\langle S_z n\rangle + \frac{1}{2}\left(\langle S_z\rangle + 1\right) + C_{\text{QQ}}\right), && (4.11)\\
\langle S_z\rangle &= D_0 - \frac{4g^2}{\Gamma_1}\frac{\Gamma_\varphi}{\Gamma_\varphi^2+\Delta^2}\left(\langle S_z n\rangle + \frac{1}{2}\left(\langle S_z\rangle + 1\right) + C_{\text{QQ}}\right). && (4.12)
\end{aligned}
$$

We can now turn these expressions into a closed system of equations by factorizing $\langle S_z n\rangle = \langle S_z\rangle\langle n\rangle$ and by neglecting qubit-qubit-correlations, $C_{\text{QQ}} = \left(\sum_{\mu\neq\nu}\langle\sigma_+^\mu\sigma_-^\nu\rangle\right)/N_q \approx 0$. This finally leads to the following equation for the

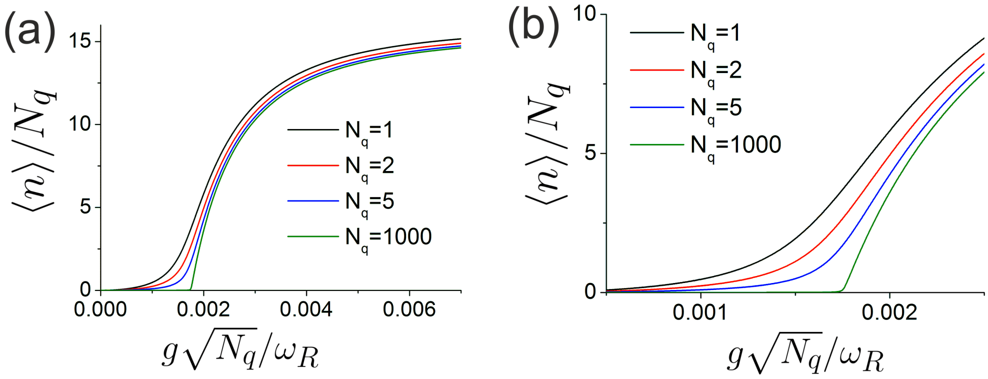

Figure 4.1: (a) Scaled photon number as function of the scaled coupling strength for zero detuning, $\Delta = 0$, and different numbers of qubits. (b) Scaled photon number in the transition region. Other parameters like in Fig. 3.4.

scaled photon number $\langle\tilde{n}\rangle = \langle n\rangle/N_q$:

$$\langle\tilde{n}\rangle^2 + \left(\tilde{n}_0 - \frac{\Gamma_1 D_0}{2\kappa} - \frac{N_{\mathrm{th}}}{N_q} + \frac{1}{2N_q}\right)\langle\tilde{n}\rangle - \left(\frac{N_{\mathrm{th}}\tilde{n}_0}{N_q} + \frac{N_{\mathrm{th}}}{2N_q^2} + \frac{\Gamma_1}{4\kappa}\frac{D_0+1}{N_q}\right) = 0 \tag{4.13}$$

4.2 Few-qubit lasing: Results

In this section we will investigate the scaling behavior of few-qubit-lasers. We start by discussing the average photon number and the linewidth on resonance, which can be calculated using the semiquantum approach. We then also investigate qubit-field-correlations and qubit-qubit-correlations, which we obtain by solving the master equation numerically.

Scaling in the semiquantum approximation

Average photon number

In Fig. 4.1, we plot the scaled average photon number $\langle n\rangle/N_q$ as function of the scaled coupling $g\sqrt{N_q}$ at full resonance for different values of the number N_q of qubits. We observe that all curves show the same asymptotic behavior and only differ in the lasing transition region. To understand this, we can take a look at the semiquantum equation for the scaled photon number at zero temperature, $N_{\text{th}} = 0$:

$$\langle \tilde{n} \rangle^2 + \left(\tilde{n}_0 - \frac{\Gamma_1 D_0}{2\kappa} + \frac{1}{2N_q} \right) \langle \tilde{n} \rangle - \frac{\Gamma_1}{4\kappa} \frac{D_0 + 1}{N_q} = 0 \tag{4.14}$$

This equation is quite similar to the semiclassical equation (4.7) except for the additional terms $\sim 1/N_q$, which describe spontaneous emission. As already mentioned, the semiclassical equations predict that a few-qubit-laser behaves similarly like a single-qubit laser with an effective coupling strength $g_{\text{eff}} = g\sqrt{N_q}$. This explains that all curves show the same asymptotic behavior below and above the lasing threshold.

On the other hand, spontaneous emission leads to a smoothening of the lasing transition. The corresponding terms $\sim 1/N_q$ decrease with the number of qubits, so that the effects of spontaneous emission should become smaller for larger numbers N_q. For very large numbers of qubits, the terms disappear, and the solution of the semiquantum equation approaches the semiclassical solution, characterized by a sharp transition between the lasing and the non-lasing regime. This is demonstrated by plotting the average photon number for $N_q = 1000$ in Fig. 4.1.

The threshold condition $\tilde{n}_0 < \Gamma_1 D_0/(2\kappa)$ at resonance, $\Delta = 0$, now leads to the equation

$$g > \frac{1}{\sqrt{N_q}} \cdot \sqrt{\frac{\kappa \Gamma_\varphi}{2D_0}}, \tag{4.15}$$

which means that the coupling between the qubits and the resonator needed to support a lasing state in the resonator is proportional to $N_q^{-1/2}$. The saturation photon number, i.e., the average photon far above the lasing threshold, is proportional to the number of qubits:

$$\bar{n}_{\text{sat}} = N_q \cdot \frac{\Gamma_1 D_0}{2\kappa}. \tag{4.16}$$

Linewidth on resonance and frequency shift

In analogy to the derivation presented in Sec. 3.4, we can also obtain an expression for the linewidth at resonance, $\kappa_L(\Delta = 0)$, for the case of several qubits coupled to the resonator:

$$\kappa_L^{\text{SQ}}(\Delta = 0) = \frac{\kappa}{2} - \frac{g^2 N_q}{\Gamma_\varphi} \langle S_z^{\text{SQ}} \rangle = \frac{\kappa}{2} \frac{N_{\text{th}}}{\langle n \rangle} + \frac{g^2 N_q}{\Gamma_\varphi} \cdot \frac{\langle S_z \rangle + 1}{2\langle n \rangle} \tag{4.17}$$

Like we discussed earlier, this expression provides the correct qualitative behavior of the linewidth for zero detuning between the qubits and the resonator.

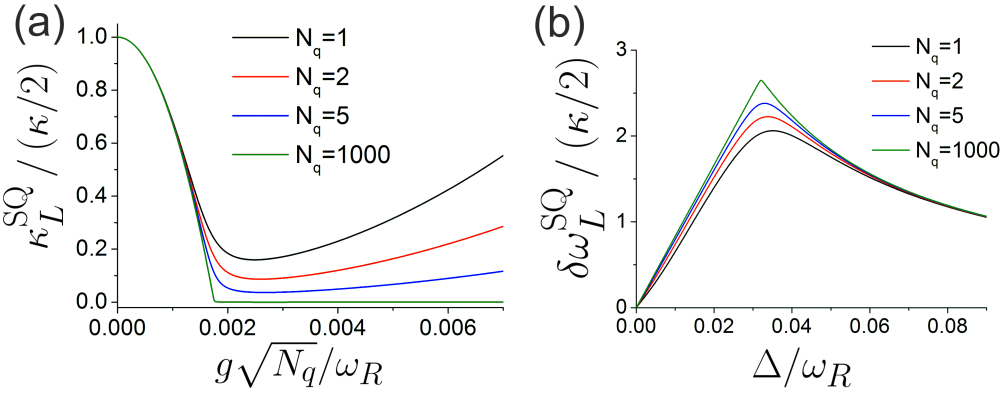

Figure 4.2: (a) Linewidth as function of the scaled coupling strength at resonance, $\Delta = 0$, calculated within the semiquantum approach. (b) Frequency shift as function of the detuning for a fixed value $g\sqrt{N_q}/\omega_R = 5 \times 10^{-3}$ of the scaled coupling strength. Other parameters like in Fig. 3.4.

In Fig. 4.2a, we show the linewidth at resonance calculated within the semiquantum approach. For small numbers of qubits, $N_q = 1, 2$, we observe a strong increase of the linewidth in the lasing regime. For larger numbers, $N_q = 5$, the increase is still present, but becomes less pronounced, so that deep in the lasing regime, the linewidth is still much smaller than the bare linewidth of the resonator. Finally, for large numbers of qubits, $N_q = 1000$, the curve becomes relatively flat, although the linewidth still increases above the lasing threshold.

This behavior can be understood by looking at Eq. (4.17), which predicts that for the same values of the scaled coupling $g\sqrt{N_q}$ and different numbers of qubits, the linewidth scales as $\kappa_L^{\mathrm{SQ}}(\Delta = 0) \sim 1/\langle n \rangle$. Since the average photon number is proportional to the number of qubits, $\langle n \rangle \sim N_q$, this means that the linewidth at resonance is inversely proportional to the number N_q: $\kappa_L^{\mathrm{SQ}}(\Delta = 0) \sim 1/N_q$.

As discussed for the case of a single-qubit laser, the semiquantum approach gives accurate results for the frequency shift in all parameter regimes. For the case of N_q qubits coupled to the resonator, we obtain the following expression for the frequency shift for zero temperature, $N_{\mathrm{th}} = 0$:

$$\delta\omega_L^{\mathrm{SQ}} = \frac{g^2 N_q \Delta}{\Gamma_\varphi^2 + \Delta^2} \cdot \langle S_z \rangle = \frac{\Delta\kappa}{2\Gamma_\varphi} - \frac{g^2 N_q \Delta}{\Gamma_\varphi^2 + \Delta^2} \cdot \frac{\langle S_z \rangle + 1}{2\langle n \rangle} \tag{4.18}$$

Fig. 4.2 shows the frequency shift as function of the detuning for a fixed value of the scaled coupling strength, $g\sqrt{N_q}/\omega_R = 5 \times 10^{-3}$. The curves

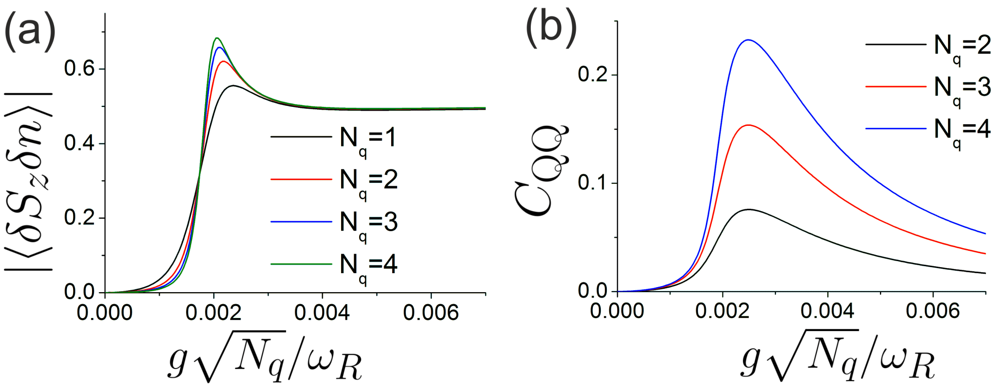

Figure 4.3: (a) Qubit-field correlations $\langle \delta S_z \delta n \rangle = \langle S_z n \rangle - \langle S_z \rangle \langle n \rangle$ as function of the scaled coupling for different numbers of qubits. (b) Qubit-qubit-correlations $C_{\text{QQ}} = \left(\sum_{\mu \neq \nu} \langle \sigma_+^{\mu} \sigma_-^{\nu} \rangle \right) / N_q$ as function of the scaled coupling. Other parameters like in Fig. 3.4.

for different numbers of qubit look quite similar and only differ in the lasing transition region. This means that the position of the emission peak is almost independent of the number of qubits. For small detuning, deep in the lasing regime, the frequency shift depends linearly on the detuning, $\delta\omega_L \approx \kappa\Delta / (2\Gamma_\varphi)$. Below the lasing threshold, for large detuning, where the qubit inversion is given by $\langle S_z \rangle \approx D_0$, the frequency shift can be expressed as $\delta\omega_L \approx g^2 N_q D_0 / \Gamma_\varphi$. Around the lasing threshold, for increasing numbers N_q qubits, we observe the sharpening of the curves which we already observed when discussing the average photon number and the linewidth.

Qubit-field and qubit-qubit correlations

We are now interested in the correlations between the qubits and the resonator and between the qubits themselves. In order to obtain these correlations, we have to numerically determine the stationary solution ρ_{s} of the master equation defined by the Hamiltonian (4.1) and the dissipation terms (4.2). As mentioned earlier, obtaining the stationary density matrix is not as numerically demanding as diagonalizing the superoperator (which would be needed for the spectral properties), which allows us to deal with up to $N_q = 4$ qubits and $N \approx 100$ photons in the resonator.

Fig. 4.3a shows the correlations between the qubits and the resonator, $\langle \delta S_z \delta n \rangle = \langle S_z n \rangle - \langle S_z n \rangle$ as function of the scaled coupling. Although the average photon number increases with the number the quits, the correlations only show a small dependence on N_q. In the lasing transition region, the product $\langle S_z\rangle\langle n\rangle \sim N_q$ is still relatively large (see Fig. 3.6). This means that the correlations $\langle \delta S_z \delta n\rangle$ become smaller with respect to the product $\langle S_z\rangle\langle n\rangle$ for increasing numbers of qubits. As a consequence, for larger number N_q, quantum effects should play a smaller role around the lasing threshold. This is confirmed by our results presented in the previous sections, which demonstrated the sharpening of the lasing transition.

We show the qubit-qubit correlations $C_{\mathrm{QQ}} = \left(\sum_{\mu\neq\nu}\langle\sigma_+^\mu\sigma_-^\nu\rangle\right)/N_q$ as function of the scaled coupling in Fig. 4.3b. Since there is no direct coupling between the qubits, the correlations are mediated via the resonator field. Here we observe that the correlations C_{QQ} increase with the number of qubits.

The sum $\sum_{\mu\neq\nu}$ contains $N_q\cdot(N_q-1)$ terms. In our case, where all qubits have the same frequency and dissipation rates, the sum simplifies to $\sum_{\mu\neq\nu}\langle\sigma_+^\mu\sigma_-^\nu\rangle = N_q\cdot(N_q-1)\,\langle\sigma_+^1\sigma_-^2\rangle$, so that we get the simple expression $C_{\mathrm{QQ}} = (N_q-1)\cdot\langle\sigma_+^1\sigma_-^2\rangle$. If we compare this to our numerical results, we see that the correlations $\langle\sigma_+^\mu\sigma_-^\nu\rangle = \langle\sigma_+^1\sigma_-^2\rangle$ between two single qubits are nearly independent of the number N_q and only depend on the scaled coupling strength $g\sqrt{N_q}$.

4.3 Effects of slow noise: Introduction

In this section we turn our discussion back to the case of a single-qubit laser and investigate the influence of slow noise, i.e., low-frequency fluctuations of the qubit level spacing, on the properties of a single-qubit laser. To illustrate the problem, we first focus on the case of an SSET-laser, which consists of a pumped charge qubit coupled to a resonator (see Sec. 2.1). One of the major sources of decoherence in a charge qubit is 1/f charge noise [66], which is caused by background charges and which leads to slow fluctuations of the gate voltage. To include this effect in our model, we rewrite the qubit terms in the Hamiltonian 2.2 in the form

$$H = -\frac{1}{2}\left(\epsilon_{\mathrm{ch}}^0 + \epsilon_{\mathrm{ch}}(t)\right)\tau_z - \frac{1}{2}E_J\,\tau_x. \tag{4.19}$$

The electrostatic energy $\epsilon_{ch} = 4E_C\,(C_gV_g/e-1)$ is now the sum of a controlled part ϵ_{ch}^0 and of fluctuations $\epsilon_{\mathrm{ch}}(t)$. Moving to the diagonal basis of the Hamiltonian at the time t, we obtain $H = 1/2\cdot\sqrt{\left(\epsilon_{\mathrm{ch}}^0+\epsilon_{\mathrm{ch}}(t)\right)^2+E_J^2}\cdot\sigma_z$. Now, assuming that the fluctuating part of the electrostatic energy is small compared to the level spacing without fluctuations, $|\epsilon_{\mathrm{ch}}(t)| \ll \sqrt{\left(\epsilon_{\mathrm{ch}}^0\right)^2+E_J^2}$, we can expand the Hamiltonian up to first order in $\epsilon_{\text{ch}}(t)$:

$$\begin{aligned} H &\approx \frac{1}{2}\left(\sqrt{\left(\epsilon_{\text{ch}}^0\right)^2+E_J^2}+\frac{\epsilon_{\text{ch}}^0}{\sqrt{\left(\epsilon_{\text{ch}}^0\right)^2+E_J^2}}\epsilon_{\text{ch}}(t)\right)\cdot\sigma_z \\ &= \frac{1}{2}\left(\Delta E_0+\delta\Delta(t)\right)\sigma_z. \end{aligned} \tag{4.20}$$

The fluctuations of the gate voltage thus lead to fluctuations of the qubit level spacing.

So far, dissipation on the qubit and the resonator was described by Lindblad terms in the master equation for the density-matrix of the system. However, this is only allowed if the noise is Markovian, i.e, if the correlation time of the noise is much smaller than the typical timescale of the system. Thus, we have to treat slow fluctuations in a different manner.

We now introduce our general model: The idea is to split up the noise into a high-frequency, Markovian contribution and a low-frequency, non-Markovian part. Like before, we use the Lindblad terms (2.15) and (2.18) to describe Markovian noise, e.g., incoherent single-electron tunneling or damping of the resonator.

On the other hand, we describe the slow fluctuations by including them in the Jaynes-Cummings-Hamiltonian

$$H=\frac{1}{2}\Delta E(t)\cdot\sigma_z+\hbar\omega_R a^\dagger a+\hbar g\left(\sigma_+ a+\sigma_- a^\dagger\right), \tag{4.21}$$

where we split up the level spacing into a controlled and a fluctuating part, $\Delta E=\Delta E_0+\Delta(t)=\omega_R+\Delta_0+\delta\Delta(t)$. We now make two assumptions for the non-Markovian noise:

1. Slow noise: We assume that the correlation time τ_c of the noise is much longer than the typical timescale of the system, which is the linewidth κ_L, so that the relation $\tau_c \gg \kappa_L^{-1}$ is fulfilled.

2. Gaussian noise: We assume that the fluctuations of the detuning $\Delta(t)$ are characterized by a distribution function $P(\Delta)=1/\left(\sigma\sqrt{2\pi}\right)\cdot\exp\{-(\Delta-\Delta_0)^2/\left(2\sigma^2\right)\}$, i.e., by a Gaussian distribution with a width σ centered around the detuning Δ_0.

The first assumption makes sure that the system evolves on a much faster timescale than the detuning. The noise is then called quasi-static [69]. As a consequence, we can assume that at a fixed time t, the system will be in a

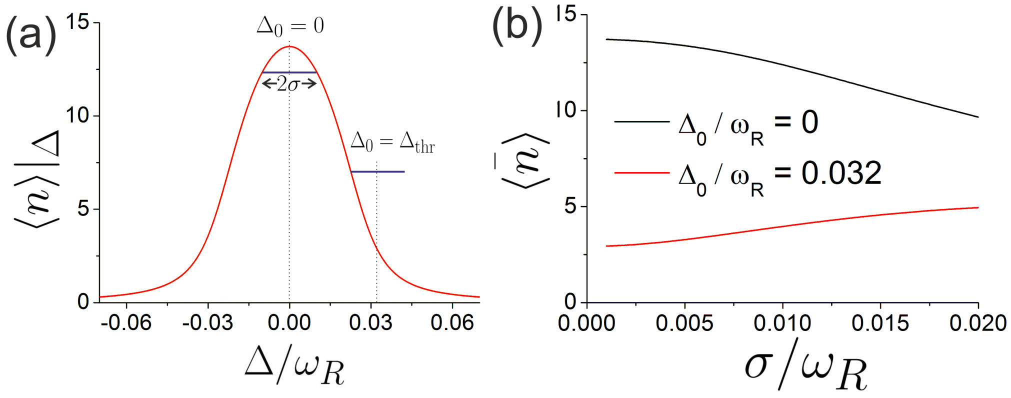

Figure 4.4: (a) Stationary photon number $\langle n\rangle|_\Delta$ as function of the detuning. The blue lines mark a region of width $2\sigma/\omega_R = 2 \times 10^{-2}$ around the two values of Δ_0 used in the second plot. (b) Average photon number as function of the width σ for two values of the detuning, $\Delta_0 = 0$ and $\Delta_0/\omega_R = \Delta_{\rm thr}/\omega_R = 0.032$. The coupling strength has a value $g/\omega_R = 5 \times 10^{-3}$, other parameters like in Fig. 3.4.

state defined by the actual value of the detuning $\Delta(t)$.

The outcome of a single measurement of a physical quantity at certain time t will in general depend on the actual value $\Delta(t)$ of the detuning. If the measurement is repeated at a different time, with another value of the detuning, also the outcome will be different. Thus, when a large number of measurements are performed, there will be contributions from all possible values of the detuning, weighted with the probability $P(\Delta)$.

As an example, a measurement of the number of photons in the resonator will yield the result

$$\langle \bar{n}\rangle = \int d\Delta \, P(\Delta) \, \langle n\rangle|_\Delta \,, \tag{4.22}$$

where $\langle n\rangle|_\Delta$ is the average photon number obtained by calculating the stationary density matrix for a fixed value Δ of the detuning.

In Fig. 4.4b we plot the average photon number $\langle \bar{n}\rangle$ as function of the width σ of the fluctuations and for two fixed values of the detuning Δ_0. In the first case, $\Delta_0 = 0$, $\langle \bar{n}\rangle$ decreases with σ. This can be understood by looking at Fig. 4.4a, where the stationary photon number $\langle n\rangle|_\Delta$ (in absence of slow noise) is plotted.

The main contribution to the integral (4.22) results from values of the detuning fulfilling the condition $|\Delta - \Delta_0| \lesssim \sigma$. For increasing values of the width σ, the system has a higher probability of being in a state characterized

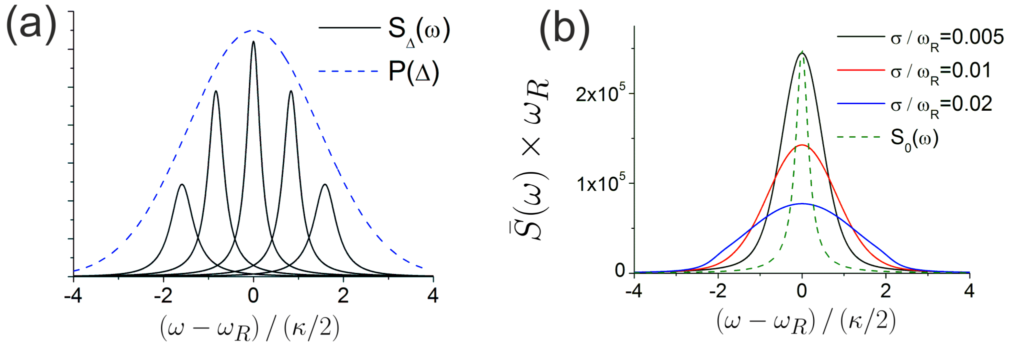

Figure 4.5: (a) Illustration of the averaging: We show the spectral function $S_\Delta(\omega)$ for several values of the detuning. $P(\Delta)$ is the weight of these peaks in the expression for $\bar{S}(\omega)$. (b) The spectrum $\bar{S}(\omega)$ for different values of the width σ for a fixed value of $\Delta_0 = 0$. For comparison, we also show the spectral function $S_0(\omega)$ in absence of slow noise. The coupling strength has a value $g/\omega_R = 5 \times 10^{-3}$, other parameters like in Fig. 3.4.

by a larger detuning and a smaller stationary photon number $\langle n\rangle|_\Delta$. Thus, a growing number of single measurements will record low values for the photon number, which leads to a decrease of the average $\langle \bar{n}\rangle$.

The second curve shows the average photon number $\langle \bar{n}\rangle$ for a situation where the single-qubit laser is operated in the lasing transition regime, $\Delta_0 = \Delta_{\text{thr}}$. This time, the average $\langle \bar{n}\rangle$ increases with the width σ. This can be understood in analogy to the case $\Delta_0 = 0$: For increasing width σ, we get more contributions from values of the detuning which are closer to the resonance $\Delta = 0$ and which correspond to states with a higher stationary photon number. These contributions near the resonance are responsible for the growth of the integral (4.22).

4.4 Effects of slow noise: Broadening of the emission spectrum

Here we are interested in the emission spectrum in the presence of slow noise. The approach used here is similar to the one presented in the previous section for the case of the average photon number and is illustrated in Fig. 4.5a. Due to the slow fluctuations, the detuning $\Delta(t)$ is varying on a timescale which is slow compared to the dynamics of the qubit-resonator system.

A measurement of the spectrum at a certain time t will yield the spectral function $S_{\Delta(t)}(\omega)$, which we define as the spectral function calculated with our usual method in absence of slow noise and for a fixed value of the detuning $\Delta(t)$. If the measurement is repeated many times, the system will go through many possible values of the detuning. The main effect of a finite detuning, apart from changing the linewidth, is a shift of the emission peak $S_\Delta(\omega)$. Thus, measurements of the spectrum at different times will provide emission peaks at different positions on the frequency axis.

To describe the outcome of many measurements, we have to integrate over all possible values of the detuning, weighted with the probability $P(\Delta)$:

$$\bar{S}(\omega) = \int d\Delta \, P(\Delta) \, S_\Delta(\omega). \tag{4.23}$$

Like before, we will assume a Gaussian distribution of width σ and centered around the detuning Δ_0, $P(\Delta) = 1/\left(\sigma\sqrt{2\pi}\right) \cdot \exp\{-(\Delta - \Delta_0)^2/\,(2\sigma^2)\}$.

In Fig. 4.5b, we show the spectrum $\bar{S}(\omega)$ for several values of the width σ and for a fixed value $\Delta_0 = 0$. The values we used for the width are typical for superconducting circuits: for a resonator frequency of $\omega_R = 10\,\mathrm{GHz}$, they lie in the range $\sigma = 50 - 200\,\mathrm{MHz}$. We see that the spectrum is much broader than the width of a single emission peak $S_\Delta(\omega)$. Also, as expected, the width of the spectrum increases with the parameter σ.

Estimate of the linewidth

Here we derive an approximative expression for the width of the spectrum $\bar{S}(\omega)$. We start by explicitly writing down the integral (4.23):

$$\bar{S}(\omega) = \frac{1}{\sigma\sqrt{2\pi}} \int d\Delta \, \exp\{-\frac{(\Delta - \Delta_0)^2}{2\sigma^2}\} \, S_\Delta(\omega). \tag{4.24}$$

We now assume that the width σ is much larger than the linewidth of a single emission peak $S_\Delta(\omega)$. This condition is usually fulfilled for typical circuit QED parameters. In this case, using the relation $\int d\omega \, S_\Delta(\omega) = 2\pi\langle n\rangle|_\Delta$, we can approximate the single emission peaks as delta functions, $S_\Delta(\omega) \approx 2\pi\langle n\rangle|_\Delta \, \delta(\omega - \omega_L(\Delta))$, where $\omega_L(\Delta)$ is the position of the respective peak.

The validity of this approximation can be checked if we assume a Lorentzian shape for the emission peaks, $S_\Delta(\omega) \approx 2\langle n\rangle|_\Delta \, \kappa_L(\Delta) \,/\, (\kappa_L^2 + (\omega - \omega_L(\Delta))^2)$, which is justified for not too strong coupling strength. Here we see that indeed $S_\Delta(\omega)$ approaches a delta function in the limit $\kappa_L(\Delta) \to 0$.

Our approximation yields the expression

$$\bar{S}(\omega) = \frac{\sqrt{2\pi}}{\sigma} \int d\Delta \, \langle n\rangle|_\Delta \, \delta(\omega - \omega_L(\Delta)) \, \exp\{-\frac{(\Delta - \Delta_0)^2}{2\sigma^2}\}. \tag{4.25}$$

As we demonstrated in Sec. 3.5, the position of the emission peaks depends linearly on the detuning in a wide range around the resonance, $\omega_L \approx \omega_R + \Delta\kappa / (2\Gamma_\varphi)$. This means that the delta function in Eq. (4.25) has its peak at the detuning $\Delta = 2\Gamma_\varphi \cdot (\omega - \omega_R)/\kappa$. We can now evaluate the integral and obtain the expression

$$\bar{S}(\omega) = \frac{\sqrt{2\pi}}{\sigma}\frac{2\Gamma_\varphi}{\kappa}\left[\langle n\rangle|_\Delta \exp\{-\frac{(\Delta-\Delta_0)^2}{2\sigma^2}\}\right]_{\Delta=2\Gamma_\varphi\cdot(\omega-\omega_R)/\kappa}. \qquad (4.26)$$

Around the resonance, the stationary photon number can be estimated as $\langle n\rangle|_\Delta \approx \Gamma_1/(2\kappa)$. This finally gives us the following approximative expression for the spectrum:

$$\bar{S}(\omega) = \frac{\sqrt{2\pi}}{\sigma}\frac{\Gamma_1\Gamma_\varphi}{\kappa^2}\cdot\exp\left[-\frac{(\omega-(\omega_R+\kappa\Delta_0/(2\Gamma_\varphi)))^2}{2(\kappa\sigma/(2\Gamma_\varphi))^2}\right]. \qquad (4.27)$$

Thus, within our approximations, the spectrum $\bar{S}(\omega)$ in the presence of slow noise has a Gaussian shape and is centered around the frequency $\bar{\omega}_L = \omega_R + \kappa\Delta_0/(2\Gamma_\varphi)$. For simplicity, we slightly change here our definition of the linewidth and define it now via the equation: $\bar{S}(\omega_{\max} \pm \tilde{\kappa}_L) = \exp\{-1/2\} \cdot \bar{S}(\omega_{\max}) \approx 0.607 \cdot \bar{S}(\omega_{\max})$ (our former definition had a factor 0.5 instead of 0.607).

The linewidth of the spectrum is then given by:

$$\tilde{\kappa}_L = \frac{\kappa\sigma}{2\Gamma_\varphi}. \qquad (4.28)$$

In Fig. 4.6a we compare numerical results for the linewidth $\tilde{\kappa}_L$ with the analytical formula (4.28). While the analytical results predicts a linear increase of the linewidth with the parameter σ, the numerical results also predict an increase, but with decreasing slope. We see that for small values of the width σ, there is a good agreement between both results. For larger values of σ, the analytical expression tends to overestimate the linewidth. In this regime, the fluctuations of the detuning become so large that the system can leave the lasing regime, so that the approximation $\langle n\rangle \approx \Gamma_1/(2\kappa)$ is not valid any more.

Fig. 4.6b shows a comparison of the numerical result for the spectrum $\bar{S}(\omega)$ and the analytical expression (4.26); in the latter, in contrast to Eq. (4.27), the stationary photon number is not assumed to be constant, which provides better results for large values of the width σ. Again, we see that the analytical expression gives a good estimate for the spectrum. The agreement

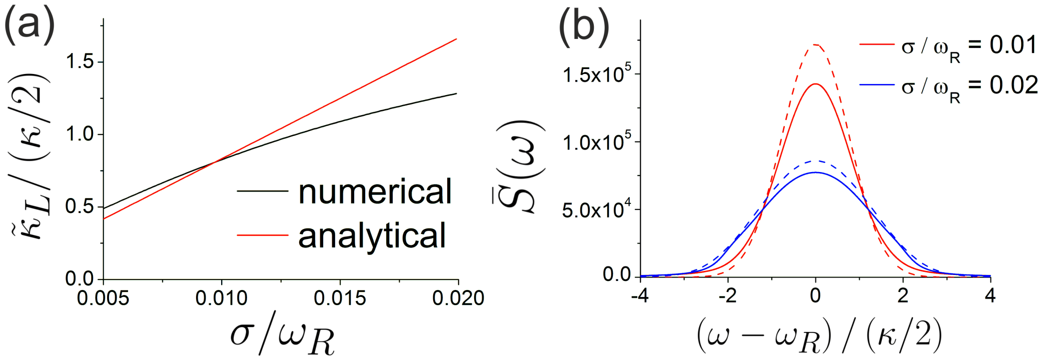

Figure 4.6: (a) Linewidth of the spectrum $\bar{S}(\omega)$ calculated numerically and by using Eq. (4.28). (b) Comparison of the numerical result for the spectrum $\bar{S}(\omega)$ (solid lines) and the analytical expression (4.26) (dashed lines) for two values of the width σ of the slow noise. The coupling strength has a value $g/\omega_R = 5 \times 10^{-3}$, other parameters like in Fig. 3.4.

between both results becomes even better for larger values of σ; we can attribute this to the approximation $\kappa_L(\Delta) \ll \sigma$ that we made in the derivation of our analytical expressions and which is better fulfilled for large values of σ.

Chapter 5

The driven nonlinear resonator: Methods

Several recent experiments based on superconducting circuits including Josephson junctions have been concerned with the properties of driven nonlinear resonators [70, 71]. One of the most interesting applications for these resonators is their use as a Josephson bifurcation amplifier (JBA), a high-contrast readout device for superconducting qubits [72]. A number of experiments have investigated the use of JBAs based on different setups, like a Josephson junction coupled to a capacitor [73, 74, 75], a Josephson junction placed in the middle of a microwave resonator [7, 8, 76, 77] or a SQUID resonator [6, 78], and have demonstrated non-demolition measurements with a readout contrast of up to 90%.

A driven nonlinear resonators can display bistability, which leads to the existence of two metastable states of low- and high-amplitude oscillations [16]. Fluctuations play an important role in this system, since they give rise to switching phenomena between these two solutions. The use of Josephson junctions makes it possible to engineer large nonlinearities, which can lead to pronounced effects already for a low number of photons in the resonator. By using a master equation approach, we can describe the behavior of a driven nonlinear resonator in the limit of low temperature, which is typically reached in circuit QED systems and where the classical fluctuations vanish and quantum noise dominates.

In this chapter, we start by introducing the system as well as some of its basic properties. In Sec. 5.2, we introduce the Hamiltonian that we use to describe the system. We then move to a description in a rotating frame and shortly discuss the concept of quasi-energy, which will be helpful for the interpretation of our later results. In Sec. 5.3 we present the master equation

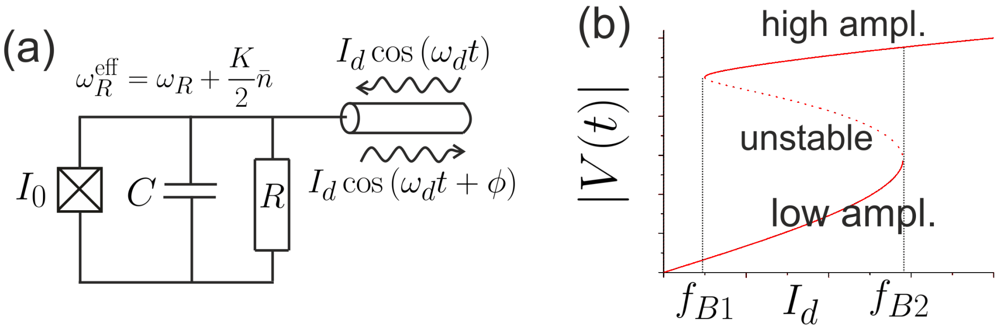

Figure 5.1: (a) Basic setup of the system: The circuit consists of a parallel combination of a Josephson junction with critical current I_0 and a capacitor C. The resistance R models damping of the current. The circuit is coherently driven, and the phase difference of the reflected signal is measured. (b) Classical solutions for the amplitude $|V(t)|$ of the voltage oscillations in the circuit as function of the driving current. We also show the bifurcation points $f_{B1,B2}$.

approach which we use to describe the dynamics of the system, and which is similar to the approach used for the single-qubit laser.

5.1 Introduction

In this second part of the thesis, we are interested in the dynamics of driven nonlinear resonators realized by superconducting circuits. Fig. 5.1a shows the basic setup, which is similar to the JBA that was used as a readout circuit in the experiment presented in Ref. [75]. The circuit consists of a Josephson junction which is coupled to a capacitor and driven by an external coherent field. The current through the Josephson junction depends on the phase difference φ across the Josephson junction, $I(t) = I_0 \sin\varphi(t)$, and the phase difference itself obeys the relation $\hbar\dot{\varphi}(t) = 2eV(t)$, where V is the voltage across the junction [79]. Using Kirchhoff's rule for the electrical current through the circuit, we obtain the following classical equation of motion:

$$C\varphi_0\,\ddot{\varphi}(t) + \frac{\varphi_0}{R}\,\dot{\varphi}(t) + I_0\,\sin\varphi(t) = I_d \cos(\omega_d t)\,, \tag{5.1}$$

where $\varphi_0 = \hbar/(2e)$ is the flux quantum and $I_d(t) = I_d \cos(\omega_d t)$ is the driving current. By expanding the sine function up to third order in φ, we get the equation of motion of a Duffing oscillator [72, 80],

$$\ddot{\varphi}(t) + \frac{1}{RC}\,\dot{\varphi}(t) + \frac{I_0}{C\varphi_0}\,\varphi(t)\left(1 - \frac{1}{6}\varphi^2(t)\right) = \frac{I_d}{C\varphi_0}\cos(\omega_d t)\,, \tag{5.2}$$

where the nonlinear term results from the nonlinear inductance of the Josephson junction. Under coherent driving, the phase $\varphi(t)$, as well as the voltage $V(t)$ across the junction, will oscillate with the driving frequency, $V(t) = V_0 \cdot \cos(\omega_d t + \phi)$.

Due to the nonlinearity, the resonance frequency of the circuit is not a constant, but depends on the amplitude of the voltage oscillations. The effective frequency of the resonator can be written as $\omega_R^{\mathrm{eff}} = \omega_R + K/2 \cdot \bar{n}$, where ω_R is the natural resonance frequency in the absence of driving and $\bar{n} \sim |V(t)|^2$ is the number of photons in the resonator.

As a consequence, the system can become bistable, like shown in Fig. 5.1b. In a certain parameter regime, between the so-called bifurcation points f_{B1} and f_{B1}, the equations of motion for the phase and the voltage have two stable solutions, corresponding to oscillations with low and high amplitude (there is also a third solution, which is unstable , and which is denoted by the dotted line in the plot).

The Josephson bifurcation amplifier

A widely used measurement scheme in coupled qubit-resonator systems is the dispersive readout. When the resonator is sufficiently detuned from the qubit, the exchange of excitations is suppressed; however, the natural frequency of the resonator will experience a shift which depends on the qubit state, $\bar{\omega}_R = \omega_R \pm \xi$ [81]. This Stark shift is then detected by coherently driving the resonator and measuring the phase of the reflected or transmitted signal.

Since the qubit state is not affected by this procedure, it is a quantum non-demolition (QND) measurement. However, the measurement time is limited by the decoherence time of the qubit, and the phase uncertainty is usually too large to clearly distinguish between the two states, which limits the readout contrast of these devices. The problem can be overcome by using a Josephson junction to make the resonator nonlinear; the device is then called a Josephson bifurcation amplifier (JBA).

For the readout, the nonlinear resonator is driven near the second bifurcation point f_{B2} (the driving strength at which the low amplitude solution ceases to exist, see Fig. 5.1b). As a consequence of thermal and quantum fluctuations, the resonator will switch from low-amplitude to high-amplitude oscillations. The time that the resonator needs to switch is very sensitive to even small changes of the characteristics of the resonator, like the natural resonance frequency and the temperature. As a consequence, the frequency shift induced by the qubit can have a very strong effect on the switching time.

The idea is now to operate the device in a way that, during the measurement time, the resonator will switch if the qubit is in the excited state, or stay in the state of low-amplitude oscillations if the qubit is in the ground state. In this way, the state of the qubit is mapped onto the state of the driven resonator [72]. This is sometimes referred to as "digital readout". We will discuss the switching process in more detail in Sec. 6.2.

To determine the state of the resonator, the phase difference ϕ between the incoming and the reflected signal is measured. Since low- and high-amplitude oscillations can be easily distinguished by their amplitude and their phase, this provides a readout method of the qubit state with a high contrast. On the other hand, the method relies on the fact that the resonator only switches if the qubit is in the ground state and stays locked to the low-amplitude state otherwise.

5.2 The Hamiltonian

We now present our model. We use the Hamiltonian

$$H = \hbar\omega_r \, a^\dagger a + \frac{\hbar K}{12}\left(a + a^\dagger\right)^4 - \hbar f \cos\left(\omega_d t\right)\left(a + a^\dagger\right), \tag{5.3}$$

to describe a resonator with natural frequency ω_r and a nonlinearity parametrized by the constant K. The strength and frequency of the coherent driving are defined by the parameters f and ω_d.

To get rid of the time-dependence resulting from the driving term, it is convenient to move to a frame rotating with the driving frequency. We therefore apply a unitary transformation $U = \exp\left(i\omega_d a^\dagger a\, t\right)$ on the Hamiltonian. The creation and annihilation operators are transformed according to $UaU^\dagger = a\exp\left(-i\omega_d t\right)$, $Ua^\dagger U^\dagger = a^\dagger \exp\left(i\omega_d t\right)$. The Hamiltonian in the rotating frame is now given by:

$$\begin{aligned} \tilde{H} &= UHU^\dagger - \hbar\delta\omega_d a^\dagger a \\ &= -\hbar\delta\omega_d a^\dagger a + \frac{1}{2}\hbar K\left(ae^{-i\omega_d t} + a^\dagger e^{i\omega_d t}\right)^4 \\ &- \frac{1}{2}\hbar f\left(ae^{-i\omega_d t} + a^\dagger e^{i\omega_d t}\right)\cdot\left(e^{i\omega_d t} + e^{i\omega_d t}\right), \end{aligned} \tag{5.4}$$

where we introduced the detuning $\delta\omega_d = \omega_d - \omega_r$ between the driving and the natural frequency of the resonator.

We will now assume that the detuning $\delta\omega_d$, the driving strength f and the nonlinearity K are much smaller than the driving frequency ω_d. These conditions are usually satisfied in circuit QED experiments [8, 74]. This allows us to drop the oscillating terms within the Rotating Wave Approximation and to obtain the time-independent Hamiltonian

$$\tilde{H} = -\hbar\delta\omega_d a^\dagger a + \frac{1}{2}\hbar K a^\dagger a \left(a^\dagger a + 1\right) - \frac{1}{2}\hbar f \left(a + a^\dagger\right). \tag{5.5}$$

5.2.1 The quasi-energy spectrum

For the interpretation of our later results, it will be useful to express the Hamiltonian (5.5) in terms of the operators $Q = \sqrt{\lambda/2}\left(a + a^\dagger\right)$ and $P = -i\cdot\sqrt{\lambda/2}\left(a - a^\dagger\right)$ [16, 80]. The two operators obey the commutation relation $[Q, P] = i\lambda$, with the effective Planck constant $\lambda = K/\left(2\delta\omega_d\right)$.

Physically, Q and P represent the amplitude of the coherent oscillations of the resonator. We can see this directly from the relation between the operators Q, P and the operator $a + a^\dagger$ in the laboratory (non-rotating) frame :

$$\left(a + a^\dagger\right)|_{\text{lab frame}} = \sqrt{\frac{2}{\lambda}}\left[Q\cos\left(\omega_d t\right) + P\sin\left(\omega_d t\right)\right] \tag{5.6}$$

In terms of these operators, the Hamiltonian (5.5) now has the form

$$\tilde{H} = -\frac{\hbar}{\lambda}\delta\omega_d\,\hat{g}, \tag{5.7}$$

$$\hat{g} = -\frac{1}{4}\left(Q^2 + P^2 - 1\right)^2 + \sqrt{\beta}\,Q, \tag{5.8}$$

with the scaled driving strength $\beta = f^2 K/\left(4\delta\omega_d^3\right)$. In this thesis, we will look at the case where both the detuning $\delta\omega_d$ and the nonlinearity K are negative, so that we get a minus sign in the definition of the operator $\hat{g}$ with respect to the case discussed in Ref. [80].

Fig. 5.2 shows the function $\tilde{H}(P, Q)$ as well as a cut through the plane $P = 0$. The shape of $\tilde{H}(Q, P)$ only depends on the scaled driving strength β. In the second row of the figure, we plot the function $\tilde{H}(Q, 0)$, which we will refer to as the quasi-potential, for different values of β. If the latter lies in the range $0 < \beta < 4/27$, the function $\tilde{H}(Q, 0)$ has three extrema, while for larger driving, $\beta > 4/27$, the function has only a single extremum [80].

We can obtain the eigenvalues of $\tilde{H}$ by numerically diagonalizing the Hamiltonian (5.5). We should keep in mind that, since we use a description in a rotating frame, the eigenvalues represent quasi-energies instead of real energies. In Fig. 5.2b we show the positions of some of the quasi-eigenlevels with respect to the quasi-potential $\tilde{H}(Q, 0)$. Here we only show the eigenlevels which are closest to the minimum and the local maximum of

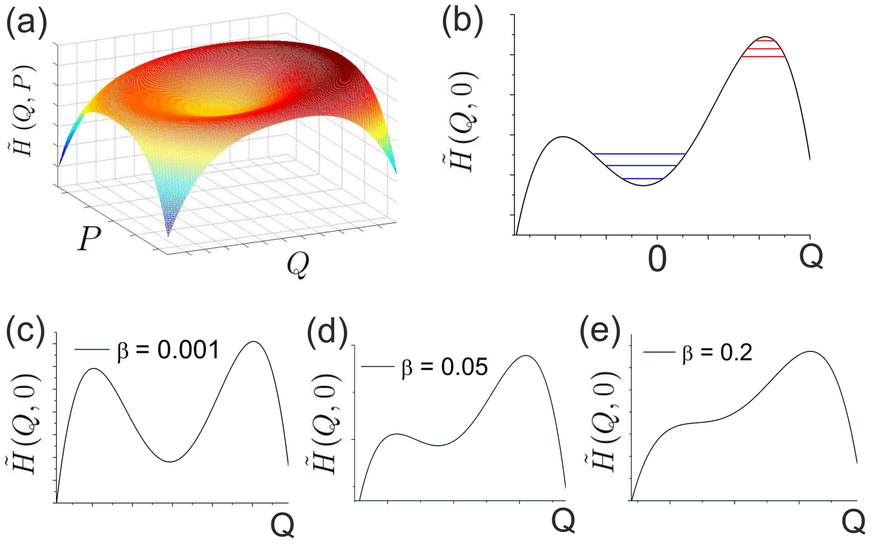

Figure 5.2: (a) Plot of the function $\tilde{H}(P,Q)$ (b) Cut through the plane $P = 0$ and position of the first 3 eigenlevels around the local minimum and the global maximum. (c)-(e) Shape of the quasi-potential for three different values of the scaled driving β. The parameters are $K/\delta\omega_d = 0.04$, $f/\delta\omega_d = 1.33$; we look at the case $\delta\omega_d < 0$.

the quasi-potential and which represent low-and high-amplitude oscillations, respectively.

To understand the physical meaning of the quasi-energy levels, it is helpful to plot the corresponding wavefunctions $\Psi_n(Q)$, i.e., the probability amplitude with respect to the variable Q. For a quasi-energy-state n, the probability to measure a value of the oscillation amplitude in the interval $[Q, Q+dQ]$ is given by $|\Psi_n(Q)|^2\, dQ$. The wavefunctions for some of the quasi-eigenlevels are shown in Fig. 5.3.

We start by discussing the quasi-energy levels that are nearest to the local minimum of the quasi-potential. Around this local minimum, the potential $\tilde{H}(Q,0)$ is approximatively of harmonic form, and the level spacing between the eigenlevels is approximatively given by the detuning $|\delta\omega_d|$; however, the eigenlevels are not equidistant due to the nonlinearity of the system.

Accordingly, the corresponding wavefunctions, which are shown in the upper row of Fig. 5.3, are very similar to the eigenfunctions of a harmonic oscillator in real space. For these states, the wavefunction $|\Psi_n(Q)|$ is nonzero only for small values of Q. Thus, for the quasi-energy states near the local minimum, the oscillation amplitude fluctuates around a small $\langle Q\rangle$, so that

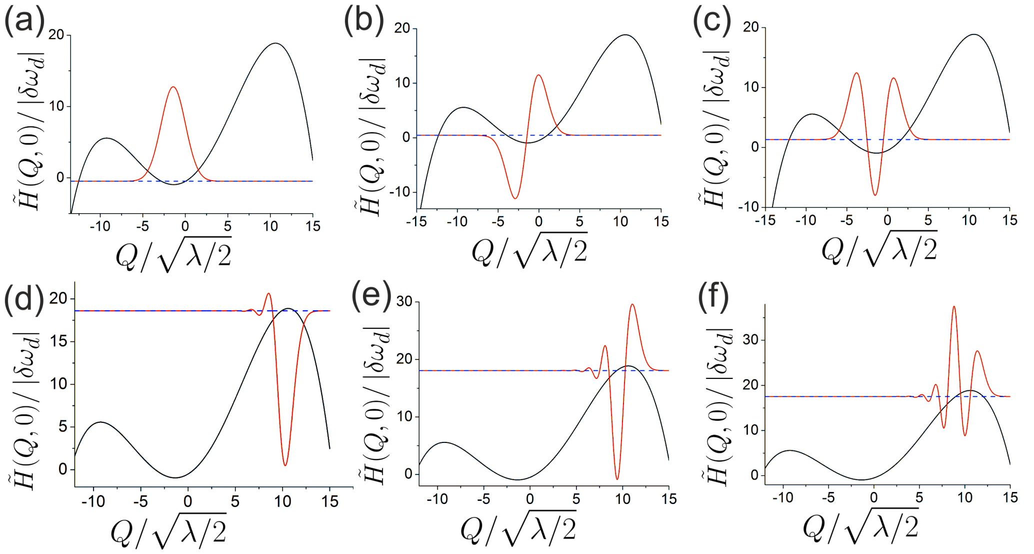

Figure 5.3: (a)-(c) Wavefunctions of the first three eigenlevels around the local minimum. The red lines show the wavefunctions $\Psi_n(Q)$, the dashed blue lines show the position of the corresponding quasi-energy levels in the quasi-potential $\tilde{H}(Q,0)$. (d)-(f) Wavefunctions of the first three levels around the global maximum. Parameters like in Fig. 5.2.

these states describe the low-amplitude oscillations of the driven nonlinear resonator.

On the other hand, the eigenlevels near to the global maximum of the quasi-potential represent high-amplitude oscillations. Again, the potential is approximatively of harmonic form around the maximum, but here the deviation from this simple form is larger than around the minimum.

This has a visible effect on the wavefunctions of the quasi-energy states, shown in the lower row of Fig. 5.3, which are now different from the eigenfunctions of a harmonic oscillator. The corresponding probability density $|\Psi_n(Q)|^2$ is only nonzero for large values of the amplitude Q. Thus, for these quasi-energy states, the oscillation amplitude fluctuates around a large value $\langle Q\rangle$.

We finally note that the second (left) maximum of the quasi-potential is related to the unstable solution, as it is known from the classical analysis of the system [82].

The shape of the quasi-potential is determined by the function $g(Q,0)$, defined in Eq. 5.8, and only depends on the scaled driving strength β. For the function $g(Q,0)$, the height of the right "inversed well" (which contains the quasi-energy states related to high-amplitude oscillations, see Fig. 5.1b) is of order 1. The Hamiltonian $\tilde{H}$ of the system is proportional to the operator $\hat{g}$, with an additional factor $-\hbar\delta\omega_d/\lambda = \hbar\left|\delta\omega_d\right|/\lambda$.

Accordingly, the height of the inversed well of the quasi-potential $\tilde{H}(Q,0)$ is of the order $\hbar\left|\delta\omega_d\right|/\lambda$. On the other hand, the level spacing between the quasi-eigenlevels is approximatively given by $\hbar\left|\delta\omega_d\right|$. This allows us to estimate the number N_{rw} of eigenlevels in the right well as $N_{\mathrm{rw}} \approx 1/\lambda$. This means that for small values of the effective Planck constant λ, i.e., for small values of the nonlinearity K, there is a dense distribution of eigenlevels (on the scale of the height of the well) around the local maximum. This is the semiclassical regime.

On the other hand, for large values of the effective Planck constant, there is a small number of quasi-eigenlevels in the inversed right well. In this regime, the level spacing is relatively large compared to the height of the inversed well, so that the eigenlevels are located at a bigger distance from the global maximum, where the deviation of the quasi-potential from a simple harmonic form becomes significant. Thus, in the quantum regime, defined by larger values of K and λ, we expect some qualitative differences in the behavior of the system with respect to the case of low-amplitude oscillations.

5.3 The master equation approach

We describe the dynamics of the system, including dissipation, by using a master equation for the density matrix, which we then solve numerically. This method is very similar to the approach that we used to investigate single-qubit lasing (see Sec. 2.3) and has been used by several authors to investigate the properties of driven nonlinear resonators [83, 84, 85]. A similar approach consists of using a Fokker-Planck-equation for the Wigner function of the resonator [86, 87].

The Liouville equation for the reduced density matrix of the resonator in the rotating frame is given by:

$$\dot{\tilde{\rho}} = -\frac{i}{\hbar}\left[\tilde{H},\tilde{\rho}\right] + L_R\tilde{\rho} = G\tilde{\rho}\,, \tag{5.9}$$

where the dissipation term $L_R\tilde{\rho}$ contains the effect of dissipation on the resonator:

$$\begin{aligned} L_R\tilde{\rho} &= \frac{\kappa}{2}\left(N_{\mathrm{th}}+1\right)\left(2a\tilde{\rho}a^\dagger - a^\dagger a\tilde{\rho} - \tilde{\rho}a^\dagger a\right) \\ &+ \frac{\kappa}{2}N_{\mathrm{th}}\left(2a^\dagger\tilde{\rho}a - aa^\dagger\tilde{\rho} - \tilde{\rho}aa^\dagger\right) \end{aligned} \tag{5.10}$$

The terms in the first and second line describe the emission and absorption of photons by the resonator, parametrized by the damping rate κ and the thermal photon number $N_{\text{th}} = (\exp(\hbar\omega_R/k_B T) - 1)^{-1}$.

5.3.1 The numerical solution of the master equation

Like for the case of the single-qubit laser, we can obtain the stationary density matrix by solving the equation

$$\frac{d}{dt}\tilde{\rho}_{\text{s}} = G\tilde{\rho}_{\text{s}} = 0, \tag{5.11}$$

where the superoperator G is defined by the equations (5.9) and (5.10).

We can calculate correlation functions by using the procedure described in Sec. 2.3. Like for the case of the single-qubit laser, we are specifically interested in the correlation function $\langle a^\dagger(t+\tau)a(t)\rangle$, which is related to the emission spectrum of the resonator.

Additionally, we want to calculate the time-dependence of average values $\langle \hat{O}(t)\rangle = \text{Tr}\{\hat{O}\rho(t)\}$, starting from an initial state $\rho(0)$. This gives us access to the behavior of the system before it reaches the stationary state, e.g, allows us to investigate the switching from low-amplitude to high-amplitude oscillations. The most interesting quantity for our purposes is the average photon number in the resonator:

$$\langle n(t)\rangle = \text{Tr}\{a^\dagger a\,\tilde{\rho}(t)\} = \text{Tr}\{a^\dagger a\, e^{Gt}\tilde{\rho}(0)\}. \tag{5.12}$$

The method used to calculate average values is very similar to the calculation of correlation functions. We first diagonalize the superoperator G and express the initial density matrix in terms of eigenvectors of G, $\tilde{\rho}(0) = \sum_k \bar{c}_k \vec{v}_k$. Acting on the equation with the exponential $\exp(Gt)$ leads to the expression

$$e^{Gt}\tilde{\rho}(0) = \sum_k \bar{c}_k e^{\lambda_k t}\vec{v}_k, \tag{5.13}$$

where λ_k is the eigenvalue of G corresponding to the eigenvector $\vec{v}_k$. By multiplying this expression with the operator $a^\dagger a$ and then taking the trace, we obtain

$$\langle n(t)\rangle = \sum_k \bar{c}_k e^{\lambda_k t}\,\text{Tr}\{a^\dagger a\, v_k\} = \sum_k \bar{\alpha}_k e^{\lambda_k t} \tag{5.14}$$

by defining the coefficients $\bar{\alpha}_k = \bar{c}_k \cdot \text{Tr}\{a^\dagger a\, v_k\}$.

To solve Eqs. (5.11) and (5.12) numerically, we have to truncate the Hilbert space of the resonator to a finite number N of photon number states. In our calculations, the number of basis states that we used is given by $N = 60$. As we will show later, the average photon number for the high-amplitude state is inversely proportional to the effective Planck constant. Therefore λ must not be too small, in order to ensure that the condition $\langle n \rangle \ll N$ is fulfilled.

We can also use the quasi-energy states of the Hamiltonian $\tilde{H}$ as basis states. This is advantageous in a situation where the system is locked in a state of high-amplitude oscillations. In this case, only a few quasi-eigenlevels around the local maximum (see Fig. 5.2) have a finite occupation probability, so that it is sufficient to only include these states as basis states. This allows us to treat the case of smaller values of the parameter λ, where the average photon number for the high amplitude state can become larger than $N = 60$.

Finally, we remark that for the calculation of average steady state values, which are fully determined by the stationary density matrix $\tilde{\rho}_{\mathrm{s}}$, the calculations reduce to solving a system of linear equations. In these cases, we can cover a much higher number of photon number states, $N \lesssim 400$.

Chapter 6

The switching rate and spectral properties

In this chapter, we want to discuss the behavior of coherently driven nonlinear resonators in the regime of large nonlinearities, low photon number and low temperature, which are typical for a circuit QED setup. We start by investigating some stationary properties of the driven nonlinear resonator and then turn our discussion to the switching time. This will be useful for our discussion in 7, where we investigate the effects of an (unwanted) two-level fluctuator on the driven resonator.

As we mentioned, driven nonlinear resonators are used in circuit QED as high-contrast readout devices; at the same time, they form an interesting system to study the effect of fluctuations on a nonlinear system in a non-equilibrium state. The fluctuations of the electrical field in the resonator give rise to broad side-peaks in the emission spectrum. By studying these side-peaks, we can thus obtain detailed information about the fluctuations and find some qualitatively new behavior for large nonlinearities, which can be reached in circuit QED systems.

In Sec. 6.1, we use the master equation approach to calculate the stationary properties of the driven nonlinear resonator. In Sec. 6.2, we then focus on the switching of the resonator from low- to high- amplitude oscillations by using the time-dependent solution of the master equation.

In Secs. 6.3-6.5 we then discuss the emission spectrum of a driven nonlinear resonator for the case that the system is locked to low- or high- amplitude oscillations. We will show that the large nonlinearity leads to qualitatively new features in the spectrum, most notably the appearance of second-order side peaks.

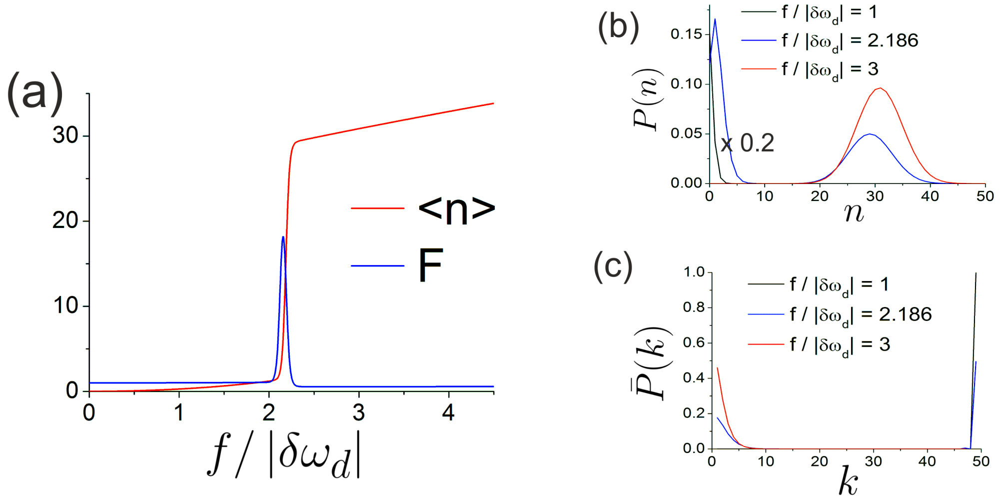

Figure 6.1: (a) Average photon number $\langle n \rangle$ in the resonator and Fano factor F in the resonator as function of the driving strength. (b), (c): Photon Distribution function $P(n)$ and the occupation probability $\bar{P}(k)$ of the quasi-energy states, for different values of the driving strength. The other parameters are $K/\delta\omega_d = 0.04$, $\kappa/\left|\delta\omega_d\right| = 0.133$ and $N_{\text{th}} = 0$. We choose the detuning to be negative, $\delta\omega_d < 0$.

6.1 Stationary properties

We start by discussing the stationary properties, which we obtain by finding the steady-state solution of the master equation, $G\tilde{\rho}_{\text{s}} = 0$, which we refer to as the stationary density matrix. Fig. 6.1a shows the average photon number $\langle n \rangle$ in the resonator and the Fano factor $F = \left(\langle n^2 \rangle - \langle n \rangle^2\right) / \langle n \rangle$ as functions of the driving strength. We observe a sharp increase of the photon number occurring at a certain value of the driving strength, which is accompanied by a maximum of the Fano factor.

In order to get a better understanding of our numerical results, it is useful to make a connection to the classical equation (5.2) for the Duffing oscillator in absence of fluctuations. The latter has two solutions, describing low- and high-amplitude oscillations. In the quantum-mechanical picture, these solutions are represented by the quasi-energy levels around the local minimum and the global maximum of the quasi-potential (see Sec. 5.2).

In the presence of fluctuations, which result from the coupling to the environment, the two solutions become metastable [88]. The fluctuations can lead to a switching of the driven resonator from a the low-amplitude to the high-amplitude state and vice versa. Thus, in the stationary state, for $t \to \infty$, the driven resonator has in general certain probability to be in the low-amplitude regime and a certain probability to be in the high-amplitude regime; the corresponding probabilities depend on the switching rates between the two metastable solutions.

In the following, we will at several points plot the occupation probability $\bar{P}(k) = \langle k \,|\tilde{\rho}_\mathrm{s}|\, k\rangle$ of the quasi-energy states k. Here we have to precise how we number these states: We start from large values of the quasi-energy and with increasing number k go to lower values of the quasi-energy. Thus, low numbers k describe the states located near the global maximum of the quasi-potential, corresponding to high-amplitude oscillations, while large numbers describe the states corresponding to low-amplitude oscillations.

We now turn back to the discussion of the average photon number, shown in Fig. 6.1a. For small values of the driving, the photon number is rather small and increases quadratically with the driving, like for a linear resonator. On the right side of Fig. 6.1, wee also show the photon distribution function $P(n)$, i.e., the probability that n photons are in the resonator, for different values of the driving strength f. The distribution function has its maximum at low values of n. In this regime of low-amplitude oscillations, the Fano factor has a value $F = 1$, which means that the function $P(n)$ describes a Poisson distribution, like in the case of a coherently driven linear resonator.

Fig. Fig. 6.1c shows the occupation probability of the quasi-energy states. For our choice of the parameters, $k = 49$ describes the quasi-energy level which is nearest to the local minimum of the quasi-potential. As we can see, only this level has a significant occupation probability. Due to the nonlinearity, the occupation of the neighboring levels is not zero (like it would be for a driven linear resonator at zero temperature), but still very small.

For large values of the driving, the curve becomes relatively flat; in this regime, the photon number shows a linear increase with the driving. The corresponding photon distribution function $P(n)$ is centered around large values of n. Here, the Fano factor has a value $F < 1$, which corresponds to a Sub-Poissonian distribution This already shows that in the regime of high-amplitude oscillations, the driven nonlinear resonator can not simply be described as a linear resonator with a modified effective frequency. In our later discussion of the emission spectrum, we will observe some further qualitative differences as compared to the linear case.

Moving to the basis of quasi-energy levels, we now observe a broad distribution of the occupation probability over many of the quasi-energy levels located around the global maximum. In the regime of high-amplitude-oscillations, the resonator thus is characterized by an finite effective temperature, even if the physical temperature is 0; this phenomenon is called quantum heating [84, 89] .

Finally, the plot of the average photon number displays a narrow region where the average photon number shows a sharp increase. The blue line in Fig. 6.1c shows the distribution function $P(n)$ for a value of the driving strength in the middle of this region (we chose f such that $\langle n \rangle \approx 15$). The function $P(n)$ now has two peaks, centered around low and high photon numbers, respectively. In this case, the system is not locked to a state of low-amplitude or high-amplitude oscillations, but has a finite probability of being in each of these states. The bistability of the system is reflected by large values of the Fano factor, $F \gg 1$.

Like the photon distribution function, the occupation probability $\bar{P}(k)$ of the quasi-energy states splits up into two peaks. The system switches between low and high-amplitude oscillations; for our specific choice of the driving strength, $f/\left|\delta\omega_d\right| = 2.186$, the resonator has equal probability to be in either of the two states.

To summarize our numerical results, we have seen that for weak driving, the driven resonator will relax to the low-amplitude solution, while for strong driving, it will relax to the high-amplitude solution. There is a narrow region of the driving where in the stationary state, the resonator will switch between the two solutions. Naturally, the stationary density matrix provides no information about the timescales involved; we will address this question in Sec. 6.2 for the special case of switching from the low- to the high-amplitude solution.

The influence of damping and temperature

So far, we discussed the role of the driving strength on the stationary properties of the driven nonlinear resonator. Since in chapter 7 we want to study the effects of a two-level-fluctuator on the resonator, it is useful to understand how the behavior of the driven resonator is depends on the coupling to the environment. For this reason, we shortly discuss the role of the damping rate κ and the thermal photon number N_{th}.

We start with the discussion of the damping rate. In Fig. 6.2a, we plot the average photon number in the resonator as function of the driving strength for different values of the damping. We see that for larger values of the damping rate, the transition from low-amplitude to high-amplitude oscillations occurs at a higher driving strength. Also, for large driving, the average photon

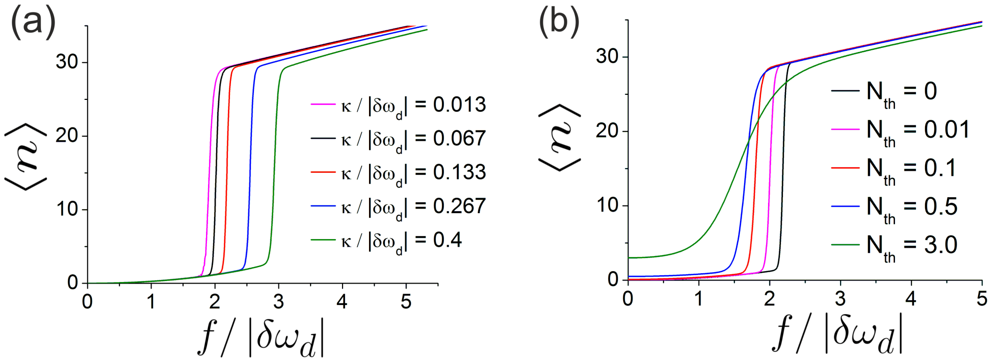

Figure 6.2: (a) Average photon number in the resonator for different values of the damping rate κ. (b) Average photon number in the resonator for different values of the thermal photon number N_{th}. Other parameters like in Fig. 6.1.

number becomes slightly smaller.

This behavior can be understood in a simple way. Generally, there is a balance between the coherent driving and the damping: While the driving provides energy to the resonator, the damping leads to a loss of energy. If now the damping rate κ is increased, also the loss rate becomes larger, which leads to a stationary state with a lower average photon number.

When the system is operated in the regime of high-amplitude oscillations and near the transition region, the driving strength is just sufficient to compensate the loss of energy, which is relatively large due to the high number of photons in this regime. If now the damping rate is increased, the driving can become too small to sustain the state of high-amplitude oscillations, so that the system switches to stationary state of low-amplitude oscillations.

We now turn to the discussion of the temperature. Fig. 6.2b shows the average photon number as function of the driving strength for different values of the thermal photon number $N_{\text{th}} = (\exp{(\hbar\omega_R/k_BT)} - 1)^{-1}$. For increasing temperature (which corresponds to an increase of N_{th}), the transition from the regime of low-amplitude to the regime of high-amplitude oscillations occurs at a lower driving strength.

By comparing the curves for $N_{\text{th}} = 0$ and $N_{\text{th}} = 0.01$, we see that already a small increase of the temperature can lead to a relatively large shift of the curves. In order to provide a feeling for the temperature scale, we note that for a typical natural frequency $\omega_R = 10\,\text{GHz}$ of the resonator, a thermal photon number $N_{\text{th}} = 1$ corresponds to a physical temperature of $T \approx 75\text{mK}$. We also see that for finite temperatures, the region in which there is a finite probability to find the resonator in a state of low-amplitude and of high-amplitude oscillations, becomes broader.

Finally, an increase of the temperature also leads to a broadening of the distribution functions. This is especially significant for weak driving, when the resonator is locked to low-amplitude oscillations. Like we have shown, only the quasi-energy level which is closest to the local minimum of the quasi-potential has a finite occupation probability at zero temperature. For finite temperature however, also the occupation probability for the neighboring levels becomes finite. As we will see in Sec. 6.4, this leads to qualitative changes in the emission spectrum.

6.2 The switching rate

Introduction and motivation

In the last section we have discussed the stationary state that the system reaches after a sufficiently long time, $t \to \infty$. In this context, we have mentioned that fluctuations can lead to a switching between the two metastable oscillation states. However, the stationary density matrix provides no information about the timescale on which the switching occurs; like we will see, the latter can vary over many orders of magnitude.

Here we focus on the switching from low- to high-amplitude oscillations. We will assume strong driving, so that the system will relax to the high-amplitude state. Solving the Liouville equation numerically, we will calculate the time-evolution of the system starting from an initial state of low-amplitude oscillations.

This corresponds to the situation encountered in experiments with Josephson bifurcation amplifiers (JBAs) [73, 6, 8]. In these experiments, the driving strength of the resonator is quickly increased and then kept constant for a certain measurement time. If the switching time is smaller than the measurement time, the resonator will switch to high-amplitude oscillations. On the other hand, if the switching time is much larger, the resonator will stay in the low-amplitude regime.

The JBA can be coupled to a qubit and be used for readout of the qubit state. For this purpose, the system is operated in the dispersive regime of circuit QED, where the detuning between qubit and resonator is larger than the coupling strength [4]. In this regime, due to the Stark shift, the natural frequency of the resonator depends on the state of the qubit: $\omega_R^{\mathrm{eff}} = \omega_R \pm \chi$. Since already a rather small shift of the resonator frequency can strongly

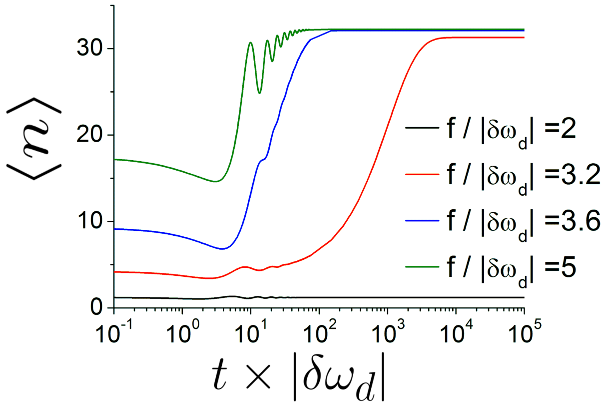

Figure 6.3: Average photon number in the resonator as function of time for different values of the driving strength. Other parameters like in Fig. 6.1.

increase or decrease the switching rate, the Josephson bifurcation amplifier can be tuned in a way so that, depending on the qubit state, it will switch or stay in the initial state. In this way, the state of the qubit is mapped onto the state of the resonator, which can then be read out without perturbing the qubit itself.

There are several physical processes which can cause the switching of the resonator. It was shown that switching of the resonator can be described in analogy to the thermal escape of a particle from the potential well around the local minimum of the quasi-potential [90]. Since the driving gives rise to an effective temperature, the switching, caused by relaxation processes of the resonator, even occurs at zero physical temperature. The corresponding switching rate has been calculated near the bifurcation points [86]. Another process which can be responsible for the switching is macroscopic quantum tunneling out of the quasi-potential well [91].

The switching process

We now want to investigate the time-evolution of the average photon number in the resonator. Fig. 6.3 shows the average photon number $\langle n \rangle$ as function of the time t for different values of the driving strength. Since the timescale of the switching can vary over many orders of magnitude, we used a logarithmic scale for the time-axis.

For low driving strength, $f/\,|\delta\omega_d| = 2$, the resonator will not switch, but stays locked to low-amplitude oscillations. For larger driving, we observe a transition of the resonator from low to high average photon numbers, which

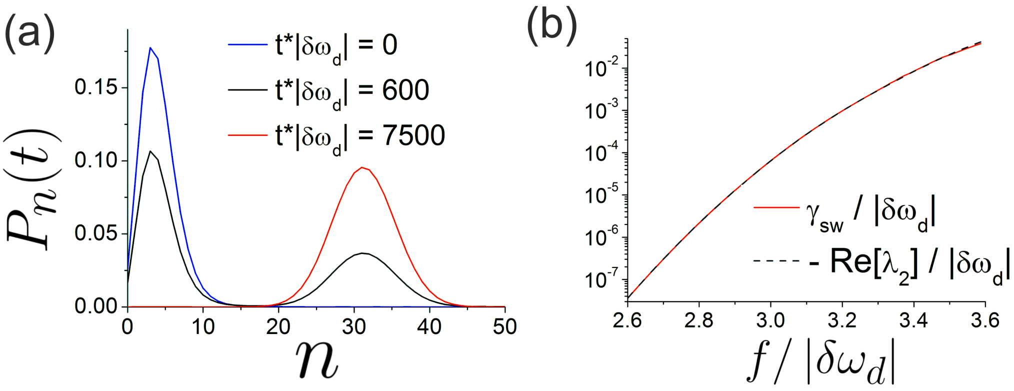

Figure 6.4: (a) Photon distribution function $P_n(t)$ for different times and a fixed driving strength $f/\,|\delta\omega_d| = 3.2$. (b) Switching rate $\gamma_{\rm sw}$ and real part of the eigenvalue λ_2. Other parameters like in Fig. 6.1.

corresponds to the switching from low- to high-amplitude oscillations. We see that the switching occurs faster for larger driving. By comparing the curves for $f/\,|\delta\omega_d| = 3.2$ and $f/\,|\delta\omega_d| = 3.6$, we can also see that a relatively small increase of the driving can decrease the switching time over some orders of magnitude.

When we calculate the time-dependent solution of the master equation, we have to specify the initial state of the system, described by the density matrix $\tilde{\rho}(0)$ at time $t = 0$. Since we are interested in the switching from low- to high-amplitude oscillations, we define the initial state as $\tilde{\rho}(0) = |k_0\rangle\langle k_0|$, where k_0 is the index of the quasi-energy level which is closest to the local minimum of the quasi-potential.

Outside the region of bistability, for scaled driving strength $\beta > 4/27$, the quasi-potential only has a single maximum, but no minimum, and accordingly only one stable solution [80]. In this case, we define the initial state by only populating the quasi-energy level with the lowest expectation value for the photon number n (this case is represented by the curve with $f/\,|\delta\omega_d| = 5$).

The switching rate

To illustrate the switching process, we show in Fig. 6.4a the photon distribution function $P(n)$ for different times t and for a fixed value of the driving strength. In the initial state, $t = 0$, only photon states with a low photon number n have a finite occupation probability, which means that system is in a state of low-amplitude oscillations.

At time $t \times |\delta\omega_d| = 600$, the function $P(n)$ has two peaks, centered around low and high numbers of photons. In the specific case shown here, the system has equal probability of being in a state of low-amplitude or high-amplitude oscillations, which means that it has equal probability of having switched or still being in the low-amplitude state.

Finally, for long times, $t \times |\delta\omega_d| = 7500$, only photon states with a large photon number n are populated. Accordingly, the probability for the system being in a state of high-amplitude oscillations, or in other words, for the system having switched, is 1.

We now define the sum

$$P_l(t) = \sum_{n=0}^{N_l} P_n(t) \tag{6.1}$$

as the probability that the driven resonator is in a low-amplitude state. The sum tends over all photon numbers $n \leq N_L$ which we can attribute to the low-amplitude oscillations. For the parameters used in Fig. 6.4a, we can set $N_l = 15$.

Using Eq. (5.13) for the time-dependent solution of the master equation, $\tilde{\rho}(t) = \sum_k \bar{c}_k \exp\{\lambda_k t\}\, \hat{v}_k$, we obtain the expression

$$P_l(t) = \sum_k \beta_k^l \, e^{\lambda_k t} \quad , \quad \beta_k^l = \bar{c}_k \sum_{n=0}^{N_l} \langle n \,|\hat{v}_k|\, n\rangle \tag{6.2}$$

for the probability $P_l(t)$.

If the function $P_l(t)$ decays exponentially (if only one eigenvalue λ_k contributes to the sum), $P_l(t) \sim e^{-\gamma t}$, we obtain the relation $P_(t_2)/P_(t_1) = \exp\{-\gamma(t_2 - t_1)\}$ for the probabilities at two different times $t_{1,2}$. This leads us to the definition of the switching rate:

$$\gamma_{\mathrm{sw}} = -\frac{\ln\{P_l(t_2)/P_l(t_1)\}}{t_2 - t_1} |_{P_l(t_1)=P_1,\, P_l(t_2)=P_2}, \tag{6.3}$$

which can also be used in the general case that several eigenvalues contribute to the sum. We calculate the switching rate in the following way: we fix the values for $P_{1,2}$, e.g., $P_1 = 0.8$, $P_1 = 0.2$, and then for each set of parameters determine the times $t_{1,2}$ for which the equations $P_l(t_1) = P_1$, $P_l(t_1) = P_2$ are fulfilled.

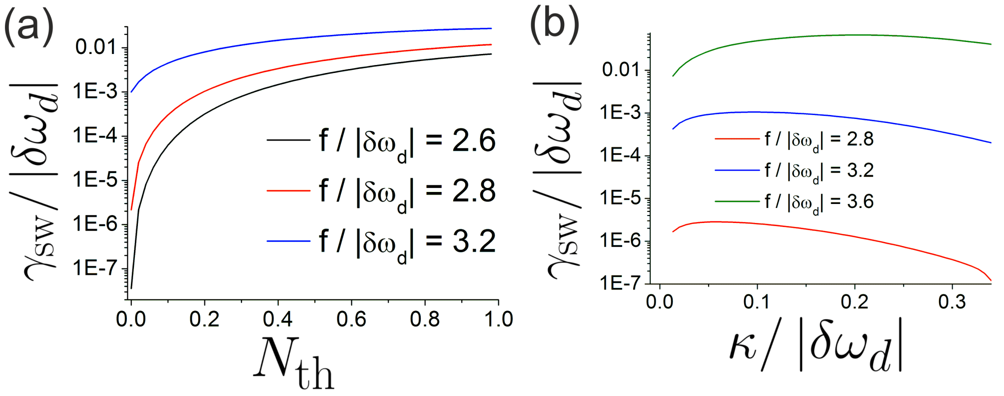

Figure 6.5: (a) Switching rate as function of the thermal photon number for different values of the driving strength. (b) Switching rate as function of the damping rate for different values of the driving strength.. Other parameters like in Fig. 6.1.

In general, the sum in Eq. (6.2) is dominated by a single eigenvalue, namely the non-zero eigenvalue of the superoperator G which has the smallest real part. We denote this eigenvalue as λ_2 ($\lambda_1 = 0$ is the eigenvalue whose corresponding eigenvector is the stationary density matrix $\tilde{\rho}_{\rm s}$).

Fig. 6.4b shows the rate $\gamma_{\rm sw}$ for different values of the driving strength f. As we have seen for the above examples, the switching rate increases with the driving strength and varies over many orders of magnitude. We observe a very good agreement between the rates γ_{sw} and $\mathrm{Re}\,[\lambda_2]$, which confirms our statement that the sum (6.2) is dominated by a single eigenvalue λ_2. For strong driving strength the discrepancy becomes a bit larger, which however cannot be seen on the logarithmic scale used in the plot.

The influence of damping and temperature

We want now to discuss the influence of the temperature and the damping rate on the switching rate of the resonator. Fig. 6.5a shows the switching rate as function of the thermal photon number $N_{\rm th} = \left(\exp\left(\hbar\omega_R/k_B T\right) - 1\right)^{-1}$. The most striking feature is that already a small finite value for $N_{\rm th}$ can lead to an increase of the switching rate over several orders of magnitude with respect to the value at zero temperature ($N_{\rm th} = 0$).

For higher temperatures, the curves become more flat. In this regime, the switching rate increases linearly with the thermal photon number, as can be seen by using a linear scale for the y-axis. The monotonic behavior of the curves $\gamma_{\rm sw}(N_{\rm th})$ is consistent with the analogy of a thermal escape out of the well around the local minimum of the quasi-potential. As the effective temperature increases with the physical temperature T, the escape rate out of the well, i.e., the switching rate, grows with the thermal photon number [90].

The temperature has also on the influence on the relative distance of the curves in Fig. 6.5a. For small temperatures, the switching rates for the three values of the driving strength shown in the plot differ by several orders of magnitude. However, for higher temperatures, the switching rates have values within the same order of magnitude so that here, the influence of the driving strength on the γ_{sw} is less pronounced.

Fig. 6.5b shows the switching rate as function of the resonator damping rate κ. Although the damping rate has an influence on the switching rate, the effect is not so strong as for the temperature. For all three values of the driving strength shown in the plot, we observe a non-monotonic dependence of γ_{sw} on the damping rate.

Again, the initial increase of the switching rate can be understood by the analogy of thermal escape out of a potential well. Since the processes leading to the escape are caused by a combination of coherent driving and dissipation [90], it can be expected that the switching rate increases with the coupling of the resonator to the dissipative environment, and hence with the damping rate κ.

On the other hand, damping is associated with the emission of photons from the resonator to the environment; this means that damping processes also tend to reduce the switching rate, since they lead to a reduction of the oscillation amplitude of the resonator rather than an increase. This explains the decrease of the switching rate observed for larger values of the damping rate κ.

6.3 The emission spectrum: Introduction

In the last part of this chapter, we investigate the emission spectrum

$$S(\omega) = 2\text{Re} \int_0^\infty dt\, e^{-i\omega\tau} \langle a^\dagger(t+\tau)a(t)\rangle \tag{6.4}$$

of a coherently driven nonlinear resonator. The use of Josephson junctions in circuit QED makes it possible to engineer large nonlinearities, which can lead to pronounced effects already for a low number of photons in the resonator. At the same time, the damping rate of the resonator can be made relatively strong while still fulfilling the condition $\kappa/\left|\delta\omega_d\right|$, which is necessary to observe well-defined peaks. As the emission power of the resonator

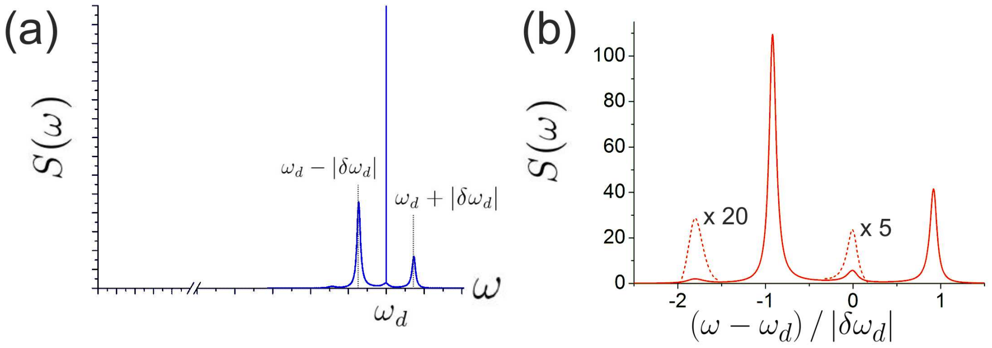

Figure 6.6: (a) Emission spectrum of the driven nonlinear resonator in the regime of high-amplitude oscillations. (b) Side-peaks around the frequency ω_d. We used $f/\,|\delta\omega_d| = 4$, $N_{\mathrm{th}} = 1$; Other parameters like in Fig. 6.1.

increases with the damping rate, a large value for κ should is advantageous for measurements of the emission spectrum.

While in the last section, we focused on the switching process, in the present section we will study the situation when the resonator is locked to the state of low- or high-amplitude oscillations. The emission power yields detailed information about the fluctuations of the electrical field. This is an interesting problem on its own, since the driven nonlinear resonator is a nonlinear system in a non-equilibrium state. Fluctuations also play an important role for the readout process with Josephson bifurcation amplifiers, since they determine the measurement backaction on the qubit [92, 93].

In Fig. 6.6 we show the emission spectrum in the high-amplitude regime for a parameter choice in the regime of operation of a Josephson bifurcation amplifier. The emission spectrum shows a sharp peak at the driving frequency as a direct consequence of the monochromatic driving, $\langle a \rangle \sim \exp\left[-i\omega_d t\right]$, and broad side-peaks which are shifted from the driving frequency, and which are related to fluctuations of the electrical field. In the following, we will subtract the contribution from the monochromatic driving and only plot the side-peaks around the frequency $\omega = \omega_d$, like shown in Fig. 6.6b.

The spectrum of a driven nonlinear resonator is usually calculated by linearizing the equations of motion around a stable point in phase space [92, 17]. In an approach based on linearized equations, only the the primary, Raman-like side-peaks around the frequencies $\omega_d \pm \delta\omega_d$ appear. This approach is sufficient if the nonlinearity of the resonator is weak compared to the detuning.

Here we solve the master equation to obtain the full emission spectrum of the driven nonlinear resonator. For strong nonlinearities, but typical circuit QED parameters we observe that additional, second-order peaks appear in the emission spectrum at the frequency $\omega_d - 2\left|\delta\omega_d\right|$ and also directly at the driving frequency [94].

In the limit of not too strong damping, we can derive an approximative expression for the emission spectrum, which can be be useful for the interpretation of our numerical results. As we have seen earlier, the low- and high-amplitude oscillations are represented by several quasi-energy levels around the local minimum or the global maximum of the quasi-potential, respectively. In the stationary state, the coupling to the environment leads to transitions between neighboring quasi-energy states; these transitions are at the origin of the side-peaks in the emission spectrum.

The derivation is shown in Appendix A and leads to the expression

$$\begin{aligned} S(\omega_d + \omega) &= \sum_{m \neq 0} \sum_{n} \left|\langle n + m \left| a \right| n \rangle\right|^2 \langle n \left| \tilde{\rho}_{\mathrm{s}} \right| n \rangle \\ &\times \frac{2\kappa_{n+m,n}}{\left(\omega - \left[\omega_n - \omega_{n+m}\right]\right)^2 + \kappa_{n+m,n}^2}, \end{aligned} \tag{6.5}$$

which predicts that transitions from the quasi-energy level n to the level $n + m$ lead to a peak in the emission spectrum at the frequency $\omega = \omega_n - \omega_{n+m} = \left(E_n - E_{n+m}\right)/\hbar$, where E_i is the energy of the quasi-energy level i in the rotating frame.

Here we focus on the situation where the system is locked to low- or high-amplitude oscillations, which means that we assume that only quasi-energy levels with energies near the local minimum or the global maximum of the quasi-potential will have a finite occupation probability. In the following, we number the quasi-energy states starting from the respective extremum of the quasi-potential (this differs from the convention used in Sec. 6.1, but is more convenient for our purposes here).

The energy difference between quasi-energy levels is approximatively given by $\omega_n - \omega_{n+m} \approx \mp m \cdot \left|\delta\omega_d\right|$ (for the low-/high-amplitude oscillations respectively). Thus, Eq. (6.5) predicts side-peaks in the emission spectrum located at the frequencies $\omega = \omega_d \mp m \cdot \left|\delta\omega_d\right|$. The height of the peaks is proportional to the absolute square of the matrix element $\langle n + m \left| a \right| n \rangle$ and to the occupation probability $\langle n \left| \tilde{\rho}_{\mathrm{s}} \right| n \rangle$ of the level $\left| n \right\rangle$.

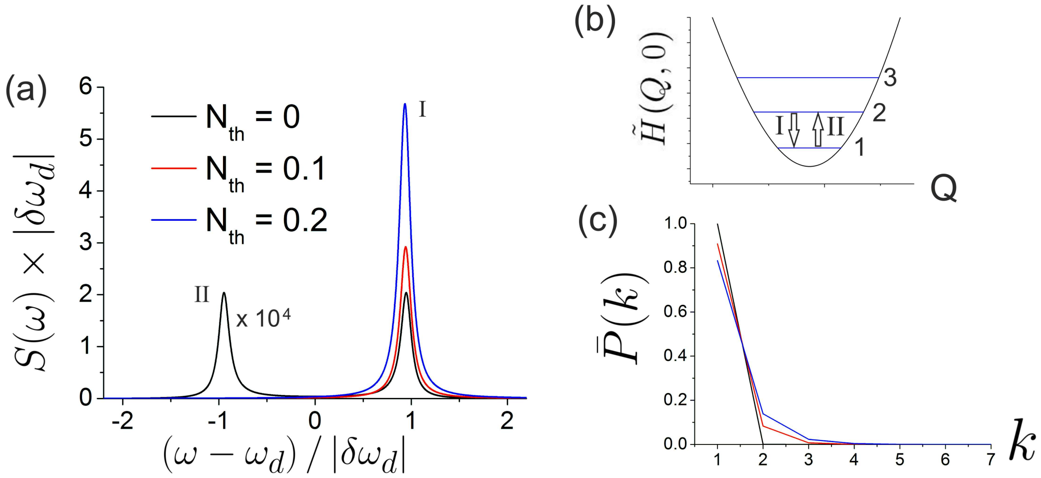

Figure 6.7: Spectrum of the driven nonlinear resonator in the regime of low-amplitude oscillations. (a) Emission spectrum for different temperatures. (b) The quasi-potential around the local minimum and the first 3 quasi-energy levels. (c) Distribution function $\bar{P}(k)$ for different temperatures, corresponding to the values used in (a). The driving strength is fixed to $f / |\delta\omega_d| = 0.67$; other parameters like in Fig. 6.1.

In a linearized theory, only transitions between nearest quasi-energy levels ($m = \pm 1$) are accounted for, so that only the primary side-peaks at $\omega \approx \omega_d \pm |\delta\omega_d|$ are predicted. As mentioned, in the regime of high-amplitude oscillations, we observe however the appearance of an additional, second-order peak at the frequency $\omega \approx \omega_d - 2\,|\delta\omega_d|$, which we can relate to transitions between next-to nearest eigenlevels ($m = 2$).

As an additional effect, we see a second-order peak at the driving frequency, which is not related to transitions between quasi-energy levels and not predicted by Eq. (6.5). We will show in Appendix A that this peaks is a consequence that the quasi-potential around the local maximum is not harmonic, but asymmetric. We will show in Sec. 6.5 that the height of the second-order grows with the effective Planck constant λ, and thus with the nonlinearity.

6.4 The emission spectrum: Results

6.4.1 The emission spectrum in the regime of low-amplitude oscillations

We first investigate the case of weak driving , where the resonator is in a stationary state of low amplitude oscillations. In Fig. 6.7b we show the quasi-potential and the position of the first three quasi-energy-levels around the local minimum. We are numbering the levels starting from the bottom of the potential and plot in Fig. 6.7c the corresponding distribution function $\bar{P}(k)$, i.e., the probability that the driven resonator is in the quasi-energy state k. We show the results for zero temperature ($N_{th} = 0$) and for finite temperature ($N_{th} = 0.1$ / $N_{th} = 0.2$). As we see, in the first case only the lowest quasi-energy state is populated, while for finite temperature, also some of the other states have a finite occupation probability.

Fig. 6.7c shows the emission spectrum $S(\omega)$. The right peak, located around the frequency $\omega \approx \omega_d + |\delta\omega_d|$, is related to processes where the system makes a transition between nearest quasi-energy states in direction towards the minimum of the potential, as illustrated by the arrow I in the quasi-potential plot, accompanied by the emission of a photon of frequency $\omega \approx \omega_d + |\delta\omega_d|$. For $T = 0$, only the lowest quasi-energy state is populated, while the occupation probability for the other states is almost zero, $\langle n \,|\tilde{\rho}_{\mathrm{s}}|\, n\rangle \approx 0$ for $n > 1$. According to Eq. (6.5), this means that height of the emission peak is very small, which is confirmed by the numerical result. On the other hand, for $T > 0$, also the other quasi-energy state have a finite occupation probability, resulting in a higher emission peak.

The approximative expression (6.5) for the spectrum also predicts that the peak height is proportional to the square of the matrix elements $\langle n-1\,|a|\, n\rangle$. In Appendix A, we calculate the matrix elements numerically and show that - in the regime of low-amplitude oscillations - the matrix elements $\langle n-1\,|a|\, n\rangle$ are much larger than the matrix elements of the form $\langle n+1\,|a|\, n\rangle$, which are related to transitions in the other direction, e.g., from level 1 to level 2 (as illustrated by the arrow II). For this reason, at finite temperature, the side-peak at the frequency $\omega \approx \omega_d - |\delta\omega_d|$ is much smaller than the other primary side peak.

Also the matrix elements of the form $\langle n+m\,|a|\, n\rangle$ with $m \neq 0$, which are connected to transitions between not-neighboring levels are very small. As a consequence we do not observe additional peaks in the spectrum.

To summarize, in the regime of low-amplitude oscillations, the system

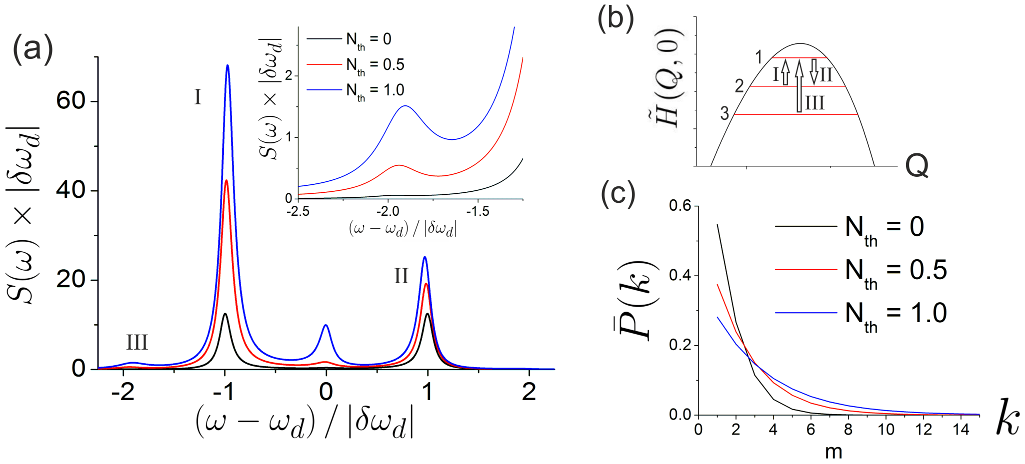

Figure 6.8: Spectrum of the driven nonlinear resonator in the regime of high-amplitude oscillations. (a) Emission spectrum for different temperatures; the inset shows the spectrum around the frequency $\omega = \omega_d - 2\,|\delta\omega_d|$. (b) The quasi-potential around the global maximum and the first 3 quasi-energy levels. (c) Distribution function $\tilde{P}(k)$ for different temperatures, corresponding to the values used in (a). The driving strength is fixed to $f / |\delta\omega_d| = 4$; other parameters like in Fig. 6.1.

qualitatively behaves like a linear resonator, and only one of the side-peaks, located around the frequency $\omega \approx |\delta\omega_d|$ is pronounced. However, the nonlinearity will lead to a shift of the emission peak; this effect will be discussed now.

6.4.2 The emission spectrum in the regime of high-amplitude oscillations

In this section, we focus on the case of strong driving, where the driven resonator is locked to a state of high amplitude oscillations. In Fig. 6.8, we plot the quasi-potential and the distribution functions for zero temperature ($N_{th} = 0$) and finite temperature ($N_{th} = 0.5$ / $N_{th} = 1$). In contrast to the case of low-amplitude oscillations, already for zero temperature there is a broad distribution over many of the quasi-energy states. Finite temperature leads to a further broadening of the distribution.

The emission spectrum shows now two pronounced primary side-peaks at the frequencies $\omega \approx \omega_d \pm |\delta\omega_d|$, in contrast to the case of low-amplitude oscillations, where only one of the peaks was pronounced. These primary side-peaks are related to transitions between nearest eigenlevels accompanied by the emission of photons with the corresponding frequency.

The peak I located at the frequency $\omega \approx \omega_d - |\delta\omega_d|$ is related to transitions between nearest levels towards the maximum of the quasi-potential. As mentioned, already for $T = 0$, the higher-lying states have a finite occupation probability, $\langle n |\tilde{\rho}_{\mathrm{s}}| n\rangle \neq 0$ for $n > 1$, so that the peak is visible at zero temperature. As we see in the plot, the peak height strongly increases with temperature.

The second primary side-peak (II), located at the frequency $\omega \approx \omega_d - |\delta\omega_d|$, is associated with transitions between nearest levels away from the maximum of the quasi-potential. The appearance of this peak is due to the fact that - in the regime of high amplitude oscillations - the corresponding matrix elements $\langle n+1 |a| n\rangle$ can be of similar size as the matrix elements $\langle n-1 |a| n\rangle$ (see App. A), which are related to the peak I. As a consequence, both primary side-peaks at frequencies $\omega = \pm |\delta\omega_d|$ are of similar height.

The height of the primary side-peaks can be well described by linearized theories [17]. However, our results show the appearance of additional, second-order peaks, which are not predicted by linearized theories.

We observe a second-order peak (III) in the emission spectrum located at the frequency $\omega \approx \omega_d - 2|\delta\omega_d|$. This peak is smaller than the primary side-peaks, but still visible, and is related to transitions between next-to-nearest quasi-energy levels (in direction towards the maximum of the potential). Again, using the approximative expression (6.5) for the emission spectrum, we can explain the appearance of this peak by looking at the corresponding matrix elements $\langle n-2 |a| n\rangle$. Like shown in appendix A, these matrix elements can become relatively large when the system is in the high-amplitude regime. The height of the emission peak also strongly increases with temperature.

Additionally, we observe in Fig. 6.8a second-order peak at the frequency $\omega = 0$, which results from the fact the the quasi-potential around the global maximum is not harmonic, but asymmetric. As we mentioned before, the stationary state of the system in the high-amplitude regime is characterized by a broad distribution over many of the quasi-energy states. For every of these states, $\langle n |Q| n\rangle = \sqrt{\lambda/2}\,\langle n \left|\left(a + a^\dagger\right)\right| n\rangle$ is the expectation value of the oscillation amplitude in the case that the system is in this specific state.

For a harmonic (quasi-)potential, the matrix elements would be simply given by the position of the global maximum of the potential, $\langle n |Q| n\rangle = Q_{\max}$. But due to the nonlinearity, the potential is asymmetric, and the oscillation amplitude $\langle n |Q| n\rangle$ of the quasi-energy states is shifted from the the position $Q_{\max}$ of the maximum, so that $\langle n |Q| n\rangle \neq \langle n' |Q| n'\rangle$ for $n \neq n'$.

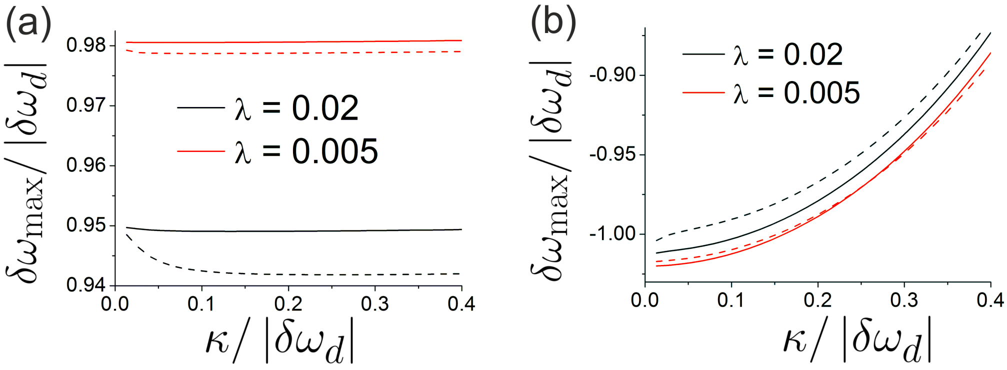

Figure 6.9: (a) Peak position of the primary side-peak at $\omega \approx \omega_d + |\delta\omega_d|$ in the low-amplitude regime as function of the damping rate for driving strength $f/|\delta\omega_d| = 0.67$ and thermal photon number $N_{th} = 0.01$ (solid lines) / $N_{th} = 0.1$ (dashed lines). (b) Peak position of the primary side-peak at $\omega \approx \omega_d + |\delta\omega_d|$ in the high-amplitude regime as function of the damping rate for driving strength $f/|\delta\omega_d| = 4$ and thermal photon number $N_{th} = 0$ (solid lines) / $N_{th} = 0.5$ (dashed lines).

We show in Appendix A that this is at the origin of the broad peak at the frequency $\omega = 0$.

6.4.3 The position of the primary side-peaks

In this section we discuss the position of the primary side-peak. The approximative expression (6.5) for the emission spectrum predicts that the position of the side-peaks is defined by the level spacing between the quasi-energies. However, the numerical results show that for strong damping, also the damping of the resonator and the temperature will have an effect on the position of the emission peaks.

In the following, we will focus on the highest side-peak, which is the side-peak at the frequency $\omega \approx \omega_d + |\delta\omega_d|$ in the regime of low-amplitude oscillations and the side-peak at the frequency $\omega \approx \omega_d - |\delta\omega_d|$ in the regime of low-amplitude oscillations.

Fig. 6.9 shows the position of the above-mentioned side-peaks as function of the damping rate κ for two different values of the effective Planck constant $\lambda = K/2\delta\omega_d$ (corresponding to two values of the nonlinearity). To determine the peak position, we calculate the spectrum numerically and directly extract the frequency $\omega_{\max} = \omega_d + \delta\omega_{\max}$ at which the peak reaches its maximum value. To show the influence of temperature, we use two different values for the thermal photon number N_{th} in each plot (solid and dashed lines).

We start by discussing the low-amplitude regime (Fig. 6.9a. For a linear resonator, $K = 0$, the emission peak would be located exactly at the frequency $\omega = \omega_d + |\delta\omega_d|$ ($\delta\omega_{\max} = |\delta\omega_d|$). Here however, we observe a shift of the frequency $\delta\omega_{\max}$ which increases with the effective Planck constant λ. To understand this, we can apply a transformation on the Hamiltonian (5.5), using the displacement operator $U(\alpha) = \exp\left[\alpha \cdot \left(a + a^\dagger\right)\right]$.

In the regime of low-amplitude oscillations, the oscillation amplitude can be approximated as $\alpha = \langle a \rangle \approx -f/\left(2\delta\omega_d\right)$. Using this value for the unitary transformation, we get rid of the driving term $-1/2\,\hbar f\left(a + a^\dagger\right)$ and obtain the new Hamiltonian:

$$\bar{H} = U(\alpha)\tilde{H}U^\dagger(\alpha) \approx -\hbar\delta\omega_d a^\dagger a + \frac{1}{2}\hbar K a^\dagger a\left(a^\dagger a + 1\right) + \hbar K \frac{f^2}{4\delta\omega_d^2}, \qquad (6.6)$$

where we neglected terms which contain a non-equal number of annihilation/creation operators. Using this approximative form of the Hamiltonian, we can determine the quasi-energy spectrum and specifically the level spacing between the first 2 levels:

$$\tilde{\omega}_{12} = \left\langle 2\left|\bar{H}\right|2\right\rangle - \left\langle 1\left|\bar{H}\right|1\right\rangle \approx |\delta\omega_d| \cdot \left[1 - 2\lambda - \lambda\frac{f^2}{\delta\omega_d^2}\right]. \qquad (6.7)$$

This expression predicts that the shift of the level spacing $\tilde{\omega}_{21}$ increases with the parameter $\lambda = K/2\delta\omega_d$. For the two values of λ used in Fig. 6.9, we obtain $\tilde{\omega}_{21} \approx 0.988$ ($\lambda = 0.005$) and $\tilde{\omega}_{21} \approx 0.951$ ($\lambda = 0.02$), which fits qualitatively the numerical data.

By comparing the solid and dashed lines, we see that an increase of the temperature has the tendency to move the peaks away from the frequency $\delta\omega_{\max} = |\delta\omega_d|$. This shift also grows with the effective Planck constant.

We want now to shortly discuss the position and the width of the primary side-peak at the frequency $\omega \approx \omega_d - |\delta\omega_d|$ in the regime of high-amplitude oscillations, which is shown in Fig. 6.9b. Our results show a monotonic increase of the frequency ω_{max} with the damping rate. The effect is much stronger than for the case of low-amplitude oscillations, where the damping rate only had a small influence on the peak position.

Comparing the solid curves, corresponding to two different values of λ, we see that for increasing λ, we obtain a shift of the peaks which is almost independent of the damping rate κ. Also a finite temperature leads to a shift of the primary side-peak; however, in the regime of not too weak damping, the effect of temperature and the parameter λ on the peak position is much smaller than the effect of the damping rate.

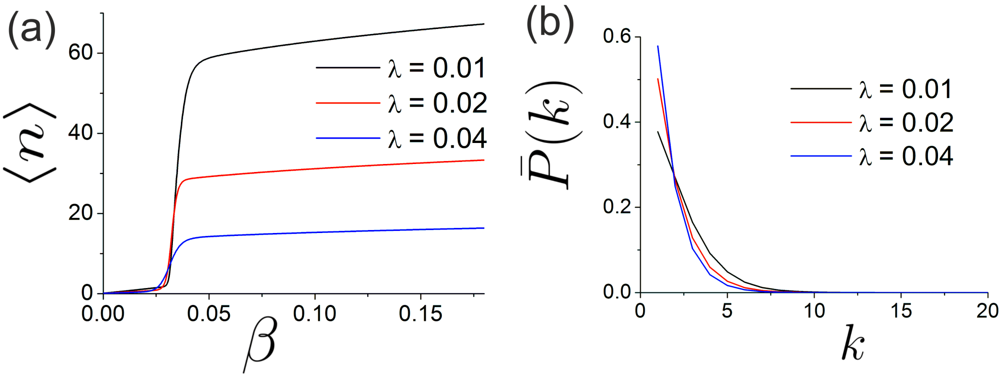

Figure 6.10: (a) Average photon number as function of the scaled driving strength β. (b) Occupation probability of the quasi-energy states for $\beta = 0.16$. We used $K = 2\lambda\delta\omega_d$ and $N_{\text{th}} = 0.1$, other parameters like in Fig. 6.1.

6.5 Role of the effective Planck constant in the high-amplitude regime

As we have seen in the last section, the nonlinearity of the resonator leads to the appearance of additional side-peaks in the emission spectrum with respect to the case of linear resonator. In this section, we want to investigate the dependence of these effects on the magnitude of the nonlinearity. We will do this by discussing the role of the effective Planck constant λ, since the latter is proportional to the nonlinearity.

In Sec. 5.2 we introduced the variables Q and P, which describe the oscillation amplitude of the resonator. The two operators obey the commutation relation $[Q, P] = i\lambda$, with the effective Planck constant $\lambda = K/\left(2\delta\omega_d\right)$. The classical dynamics of the variables Q, P are determined by the shape of the quasi-potential and only depend on the scaled driving strength β, but are independent of λ. A similar behavior can be found for the average photon number in the resonator, like shown in Fig. 6.10.

The only major difference between the three curves is a constant factor, which results from the relation $a = 1/\sqrt{2\lambda} \cdot (Q + iP)$. From the latter relation we can conclude that the average photon number in the resonator is inversely proportional to the effective Planck constant, $\langle n \rangle \sim 1/\lambda$. Consequently, a large value for λ, i.e., a large nonlinearity, leads to a small average photon number even in the regime of high-amplitude oscillations.

However, as mentioned before, the parameter λ defines the level spacing of the quasi-energy levels on the scale of the quasi-potential. For small values

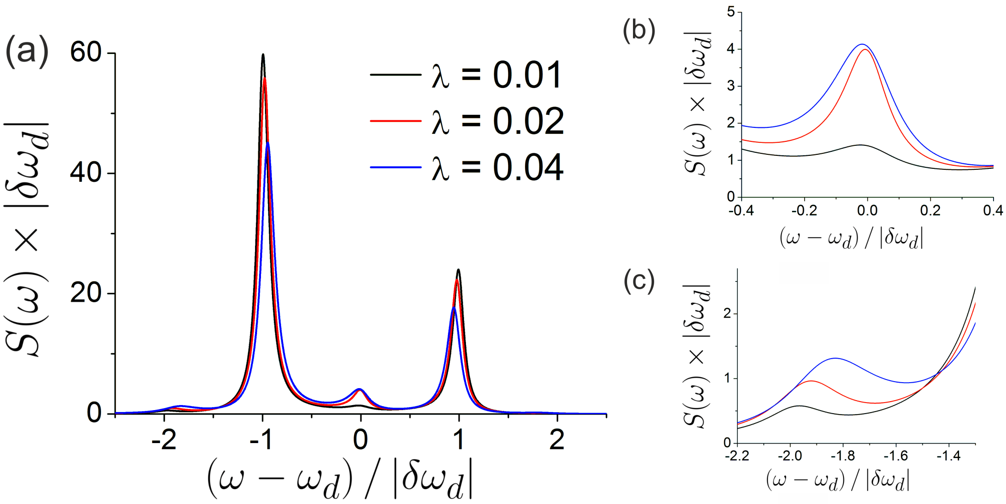

Figure 6.11: (a) Emission spectrum $S(\omega)$ for different values of the effective Planck constant λ. (b) and (c) show the second-order peaks. The value of the scaled driving strength is fixed to $\beta = 0.16$, the thermal photon number is $N_{th} = 0.75$; other parameters like in Fig. 6.1.

of λ, there is a dense distribution of eigenlevels around the extrema; this is the classical regime. On the other hand, for large values of λ, the eigenlevels are rather distant. Fig. 6.10 shows the occupation probability of the quasi-energy levels near the global maximum of the quasi-potential. We used three different values for the parameter λ and a fixed value for the scaled driving strength β.

Although the curve is more flat for small values of the effective Planck constant, the occupation probabilities of the first levels, $k \lesssim 4$, have only a small dependence on λ. This means that for large values of λ, there is a rather large occupation probability for quasi-energy levels which are relatively far away from the global maximum of the quasi-potential, so that the nonlinearity of the potential can have a larger effect.

Influence on the second-order peaks

Fig. 6.11a show the the emission spectrum of a driven nonlinear resonator for different values of the effective Planck constant λ and at a finite temperature, $N_{\mathrm{th}} = 0.75$. In order to compare the results, we fix the scaled driving strength β, thus leaving the shape of the quasi-potential unchanged (for $\lambda = 0.02$, this corresponds to the driving strength $f / |\delta\omega_d| = 4$).

Looking at the primary side-peaks at the frequencies $\omega \approx \omega_d \pm, |\delta\omega_d|$, we see that their height is slightly decreasing for larger values of λ. For the case of the left peak, which is connected to transitions between nearest quasi-energy levels towards the maximum of the quasi-potential, this is consistent with the smaller occupation probability of the higher-lying states, $k \neq 1$. For increasing values of λ, we also observe a shift of the primary side-peaks away from the frequencies $\omega = \omega_d \pm, |\delta\omega_D|$. This has been discusses in the last section.

As expected, the parameter λ has a huge influence on the second-order peaks. The peak height of the emission peak at the frequency $\omega \approx \omega_d - 2\,|\delta\omega_D|$ clearly increases with the parameter λ, as shown by the inset in Fig. 6.11a. As already mentioned, we can relate this peak to transitions between next-to-nearest quasi-energy levels in direction towards the global maximum of the quasi-potential.

Using the approximative expression (6.5) for the spectrum, we can deduce that the transition rate $|\langle k+2\,|a|\,k\rangle|^2$ is strongly increasing with the effective Planck constant; this will be confirmed in App. A. Like for the primary side-peaks, we also observe a shift of the emission peak away from the frequency $\omega = \omega_d - 2\,|\delta\omega_D|$ with increasing values of of the nonlinearity, but here the shift is even larger.

Finally, also the broad peak at the frequency $\omega = 0$ increases with the parameter λ. However, for larger values of λ, the effect is not so strong anymore, as wee can see by comparing the two curves for $\lambda = 0.02$ and $\lambda = 0.04$.

To summarize our observations, our numerical results show that the second-order peaks become visible and pronounced for large values of the nonlinearity. Thus, superconducting resonators are a promising candidate to observe these effects, since the nonlinearity can be made relatively large by using Josephson junctions.

In Ref. [94], expressions for the first- and second-order peaks, valid in the limit of small coupling, have been derived. It was shown that in this limit, the second-order peaks become visible if the effective Planck constant fulfills the condition $\kappa^2/\delta\omega_d^2 \ll K/\left(2\delta\omega_d\right)$, or equivalently, $K \gg 2\kappa^2/\delta\omega_d$.

Chapter 7

Coupling to a two-level fluctuator

In the last chapter, we have investigated the dynamics of a driven nonlinear resonator. Here we want to consider the case that the resonator is coupled to an (unwanted) two-level fluctuator (TLF). The coupling to a TLF can not be treated in the same way as the coupling to a thermal bath, since the resonator can influence the dynamics of the TLF, and, e.g., populate the excited state of the TLF even at zero temperature.

In experiments concerned with the high-contrast readout of superconducting qubits, the driven nonlinear resonator is coupled to a two-level-system (the qubit) which has a long coherence time and whose level spacing is detuned from the resonator to avoid transitions between the qubit levels. The measurement method has been demonstrated experimentally [6, 7, 8], and experimental and theoretical efforts have been done to investigate the back-action of the driven resonator on the qubit [71, 92, 95, 96].

Here we explore the situation where the level splitting of the two-level-system can be close to the resonator frequency, and where the decoherence rate of the two-level-system can be large. We are especially interested in how a TLF affects the switching of the resonator from low-to high-amplitude oscillations, which plays a central in the high-contrast readout with JBAs.

We will focus on the case of a TLF with a large decoherence rate, since in this regime, we can derive analytical expressions for the effective temperature and damping of the driven resonator in presence of a TLF, which qualitatively explain the numerical results. However, we also extend our discussion to the case of TLF with a small decoherence rate.

In Sec. 7.1 we present our model to describe the TLF and the resonator. In Secs. 7.2 and 7.3 we discuss the stationary properties of the system.

Finally, in Sec. 7.4, we investigate the effects of the TLF on the switching rate of the driven nonlinear resonator.

7.1 Model

We describe a driven nonlinear resonator which is coupled to a two-level-system. Within the Rotating-Wave Approximation (RWA), the system can be described by the Hamiltonian

$$\begin{aligned} H &= \hbar\omega_r\, a^\dagger a + \frac{\hbar K}{12}\left(a + a^\dagger\right)^4 - \hbar f \cos\left(\omega_d t\right)\left(a + a^\dagger\right) \\ &+ \frac{1}{2}\hbar\omega_{\mathrm{TLS}}\sigma_z + \hbar g\left(\sigma_+ a + \sigma_- a^\dagger\right), \end{aligned} \tag{7.1}$$

where ω_{TLS} is the frequency of the two-level system and g is the coupling strength between the resonator and the two-level-system. By doing the RWA, we assume that the detuning between the resonator and the two-level-system is not too large, $|\omega_{\mathrm{TLS}} - \omega_R| \ll \omega_R$. The operators σ_i are the usual Pauli operators.

It is convenient to move to a description in a frame rotating with the driving frequency. This is done by applying the transformation $\tilde{H} = UHU^\dagger - \hbar\omega_d\left(a^\dagger a + \sigma_z/2\right)$ with the unitary operator $U = \exp\left[i\omega_d t\left(a^\dagger a + \sigma_z/2\right)\right]$. The Hamiltonian in the rotating frame is given by

$$\begin{aligned} \tilde{H} &= -\hbar\delta\omega_d a^\dagger a + \frac{1}{2}\hbar K a^\dagger a\left(a^\dagger a + 1\right) - \frac{1}{2}\hbar f\left(a + a^\dagger\right) \\ &- \frac{1}{2}\hbar\delta\omega_{\mathrm{TLS}}\sigma_z + \hbar g\left(\sigma_+ a + \sigma_- a^\dagger\right). \end{aligned} \tag{7.2}$$

Here, $\delta\omega_{\mathrm{TLS}} = \omega_d - \omega_{\mathrm{TLS}}$ is the detuning between the driving field and the two-level-system.

The master equation approach

We assume that the resonator and the two-level-fluctuator are coupled to independent heat baths. The dynamics of the system are then described by the Liouville equation

$$\dot{\tilde{\rho}} = -\frac{i}{\hbar}\left[\tilde{H}, \tilde{\rho}\right] + L_R\tilde{\rho} + L_{\mathrm{TLS}}\tilde{\rho} = G\tilde{\rho}. \tag{7.3}$$

We use the usual Lindblad terms

$$\begin{aligned} L_{\mathrm{TLS}}\,\rho &= \frac{\Gamma_\downarrow}{2}\left(2\sigma_-\rho\sigma_+ - \rho\sigma_+\sigma_- - \sigma_+\sigma_-\rho\right) \\ &+ \frac{\Gamma_\uparrow}{2}\left(2\sigma_+\rho\sigma_- - \rho\sigma_-\sigma_+ - \sigma_-\sigma_+\rho\right) \\ &+ \frac{\Gamma_\varphi^*}{2}\left(\sigma_z\rho\sigma_z - \rho\right), \end{aligned} \tag{7.4}$$

to describe relaxation, excitation and pure dephasing of the TLF with rates $\Gamma_\uparrow$, $\Gamma_\downarrow$ and Γ_φ^*. For later purposes, we also introduce the rate $\Gamma_1 = \Gamma_\uparrow + \Gamma_\downarrow$ as well as the bare inversion $D_0 = \left(\Gamma_\uparrow - \Gamma_\downarrow\right)/\Gamma_1$. The Lindblad terms for the resonator have been introduced in Eq. (5.10).

The excitation/relaxation rates and the bare inversion of the TLF obey the relations $\Gamma_\uparrow = \Gamma_\downarrow \exp\left(-\beta\hbar\omega_{\mathrm{TLS}}\right)$ and $D_0 = -\tanh\left(\beta\hbar\omega_{\mathrm{TLS}}/2\right)$ where $\beta = 1/\left(k_B T\right)$ is the inverse temperature. If we assume that the resonator and the TLF are coupled to baths with the same temperature T, the parameter β obeys the relation $\beta = \log\left[\left(N_{\mathrm{th}}+1\right)/N_{\mathrm{th}}\right]/\left(\hbar\omega_R\right)$.

Adiabatic elimination of the TLF in the low-amplitude regime

If the dephasing rate of the TLF is much larger than the damping rate of the resonator, $\Gamma_\varphi \gg \kappa$, we can adiabatically eliminate the TLF from the equations of motion of the coupled system. The dynamics of the resonator can then be described by effective values for the detuning, the temperature and the damping, which depend on the parameters of the TLF.

In the following, we will derive an expression for the effective detuning $\delta\omega_d^{\mathrm{eff}}$, which we obtain from the semiclassical equations of motion. We then use equations for the diagonal elements of the density matrix to obtain expressions for the effective temperature $N_{\mathrm{th}}^{\mathrm{eff}}$ and damping κ^{eff} of the driven resonator in presence of a TLF.

The semiclassical approximation

The procedure we follow here to obtain the semiclassical equations is the same as discussed in Sec. 2.4. We start from the equations of motion for the system operators in the rotating frame and neglect all correlations, which leads to a system of equations for the classical variables $\alpha = \langle a\rangle$, $s_\pm = \langle\sigma_\pm\rangle$

and $s_z = \langle \sigma_z \rangle$:

$$\begin{aligned}
\frac{d}{dt}\alpha &= \left(i\delta\omega_d - \frac{\kappa}{2}\right) \cdot \alpha - iK\left|\alpha\right|^2 \alpha - igs_- + i\frac{f}{2}\,, && (7.5)\\
\frac{d}{dt}s_+ &= -\left(i\delta\omega_{\mathrm{TLS}} + \Gamma_\varphi\right) \cdot s_+ - igs_z\alpha^*\,, && (7.6)\\
\frac{d}{dt}s_z &= -2ig\left(s_+\alpha - s_-\alpha^*\right) - \Gamma_1\left(s_z - D_0\right)\,. && (7.7)
\end{aligned}$$

If the dephasing rate of the TLF is much bigger than the damping rate of the resonator, $\Gamma_\varphi \gg \kappa$, we can adiabatically eliminate the TLF variables, so that we obtain the relations $s_+ = -igs_z\alpha^* / \left(\Gamma_\varphi + i\delta\omega_{\mathrm{TLS}}\right)$ and $s_z = D_0 - 2ig/\Gamma_1 \cdot \left(s_+\alpha - s_-\alpha^*\right)$.

Plugging the expression for the variable s_+ into the equation of motion (7.5) for the variable α (describing the electrical field in the resonator), we obtain

$$\begin{aligned}
\frac{d}{dt}\alpha &= \left(i\delta\omega_d - \frac{\kappa}{2}\right) \cdot \alpha \,-\, iK\left|\alpha\right|^2 \alpha \,+\, i\frac{f}{2}\\
&+ \left(\frac{g^2\Gamma_\varphi}{\Gamma_\varphi^2 + \delta\omega_{\mathrm{TLS}}^2}\, s_z + i\frac{g^2\delta\omega_{\mathrm{TLS}}}{\Gamma_\varphi^2 + \delta\omega_{\mathrm{TLS}}^2}\, s_z\right) \cdot \alpha && (7.8)
\end{aligned}$$

The two-level-fluctuator leads to a shift of the detuning between the driving and the resonator, so that we can describe the resonator by means of the effective detuning

$$\delta\omega_d^{\mathrm{eff}} = \delta\omega_d + \frac{g^2\delta\omega_{\mathrm{TLS}}}{\Gamma_\varphi^2 + \delta\omega_{\mathrm{TLS}}^2}\, s_z\,. \tag{7.9}$$

The effective detuning depends on the TLF inversion s_z; the latter can be expressed as:

$$s_z = D_0 / \left(1 + \frac{4g^2}{\Gamma_1}\frac{\Gamma_\varphi}{\Gamma_\varphi^2 + \delta\omega_{\mathrm{TLS}}^2} \cdot \left|\alpha\right|^2\right) \tag{7.10}$$

This expression is not closed, since it still depends on the resonator field α. We can however use the approximation $\left|\alpha\right|^2 \approx \left(f/2\right)^2 / \left[\left(\kappa/2\right)^2 + \delta\omega_d^2\right]$, valid in the low-amplitude regime for $K\left|\alpha\right|^2 \ll \left|\delta\omega_d\right|, g^2/\Gamma_\varphi \ll \left|\delta\omega_d\right|$, to obtain a closed expression for the TLF inversion.

Similarly, the semiclassical equations also predict a shift of the damping rate κ. However, we will use a different route to derive an expression for the effective damping of the resonator. The method will be described below and has the advantage that it also includes the effects of temperature.

Effective damping and temperature

As we have seen in Sec. 6, the temperature and the damping rate have a strong influence on the dynamics of a driven nonlinear resonator, especially on the switching rate. In the quantum-mechanical picture, the switching from low-amplitude to high-amplitude oscillations is caused by transitions between the quasi-energy-levels due to the coupling to the environment; this phenomenon is called quantum activation [97]. As the transition rates are defined by the damping and the temperature, the latter also influence the switching rate.

Starting from the equations of motion for the diagonal elements of the reduced density matrix of the resonator, which describe the population of the quasi-energy levels, we can derive expressions for the transition rates between the quasi-energy levels. The derivation is shown in App. B; in the low-amplitude regime, the effect of the TLF on the transition rates can be qualitatively described by means of an effective damping rate κ^{eff} and an effective thermal photon number $N_{\text{th}}^{\text{eff}}$, which depend on the parameters of the TLF:

$$\kappa^{\text{eff}} = \kappa - \frac{g^2\,\Gamma_\varphi}{\Gamma_\varphi^2 + \left(|\delta\omega_d| + \delta\omega_{\text{TLS}}\right)^2}\langle\sigma_z\rangle\,, \tag{7.11}$$

$$N_{\text{th}}^{\text{eff}} = \frac{1}{\kappa^{\text{eff}}}\left[\kappa N_{\text{th}} + \frac{g^2\,\Gamma_\varphi}{\Gamma_\varphi^2 + \left(|\delta\omega_d| + \delta\omega_{\text{TLS}}\right)^2}\left(1 + \langle\sigma_z\rangle\right)\right]\,,. \tag{7.12}$$

These expressions still depend on the TLF inversion $\langle\sigma_z\rangle$. However, using the semiclassical Eq. (7.10) for the TLF inversion and the approximation $|\alpha|^2 \approx (f/2)^2 \,/\, \left[(\kappa/2)^2 + \delta\omega_d^2\right]$, we can obtain closed expressions for the effective parameters.

7.2 Stationary properties in the low-amplitude state

We start by discussing the effects of a two-level-fluctuator on a driven nonlinear resonator when the latter is locked to the regime of low-amplitude oscillations. In Fig. 7.1 we show the average photon number in the resonator as function of the detuning $\delta\omega_{\text{TLS}} = \omega_d - \omega_{\text{TLS}}$ between the two-level-fluctuator and the driving frequency. The dashed lines in the left plot show the results obtained by using Eqs. (7.9), (7.11) and (7.12) for the effective detuning,

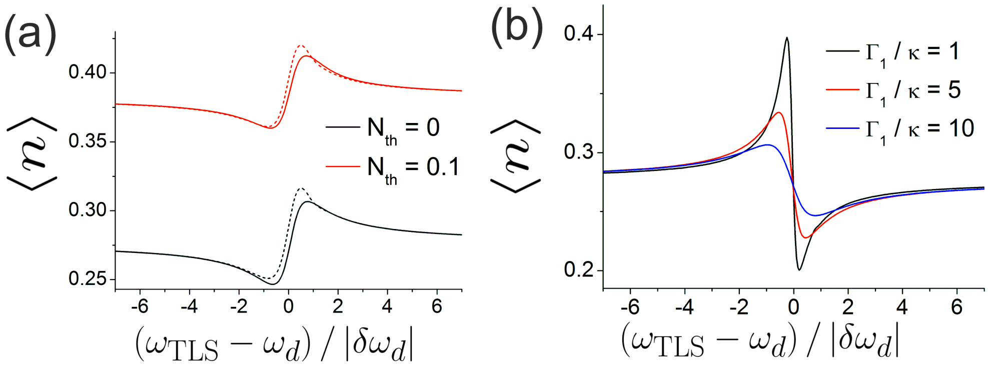

Figure 7.1: Average photon number $\langle n \rangle$ as function of the TLF frequency (a) for different values of the temperature with $\Gamma_1/\kappa = 10$, and (b) for different values of the TLF relaxation rate and $N_{\mathrm{th}} = 0$. The other parameters are $K/\delta\omega_d = 0.04$, $f/|\delta\omega_d| = 1$, $\kappa/|\delta\omega_d| = 0.133$, $g/|\delta\omega_d| = 0.27$ and $\Gamma_\varphi^* = 0$.

damping and temperature of the resonator. We observe a good agreement between both results.

Here, the effect of the TLF on the resonator can be mainly described by the effective detuning $\delta\omega_d^{\mathrm{eff}}$. Although the TLF also affects the effective damping and temperature, the latter have a rather small influence on the average photon number. For large detuning between the driving and the TLF, we obtain the relation $\delta\omega_d^{\mathrm{eff}} \approx \delta\omega_d + g^2 D_0/\delta\omega_{\mathrm{TLS}}$.

The right plot in Fig. 7.1 shows the results for different values of the TLF decoherence rate Γ_1. In the case of not too strong coupling and large values of the rate Γ_1, the effect of the resonator on the inversion of the TLF can be neglected, so that we can make the approximation $\langle \sigma_z \rangle \approx D_0$. In this case, the largest shift of the resonator detuning occurs at the TLF frequency $\omega_{\mathrm{TLS}} = \omega_d \pm \Gamma_\varphi$, and the shift is given by $\delta\omega_d^{\mathrm{eff}} - \delta\omega_d = g^2 D_0 / (2\Gamma_\varphi)$. We thus see that the effect grows with decreasing dephasing rate Γ_φ, as confirmed in the plot.

We note that for smaller values of the decoherence rate Γ_1, the average photon number shows a similar behavior as in the case of a large decoherence rate and is still well described by the Eq. (7.9) for the effective detuning. The qualitative difference is that in the regime of small TLF decoherence, the latter saturates near the driving frequency, $\langle \sigma_z \rangle \to 0$ for $\omega_{\mathrm{TLS}} \approx \omega_d$. For this reason, the shift of the detuning $\omega_d^{\mathrm{eff}} - \omega_d = g^2 \delta\omega_{\mathrm{TLS}} \langle \sigma_z \rangle / \left(\Gamma_\varphi^2 + \delta\omega_{\mathrm{TLS}}^2\right)$ stays finite for a decreasing rate Γ_1.

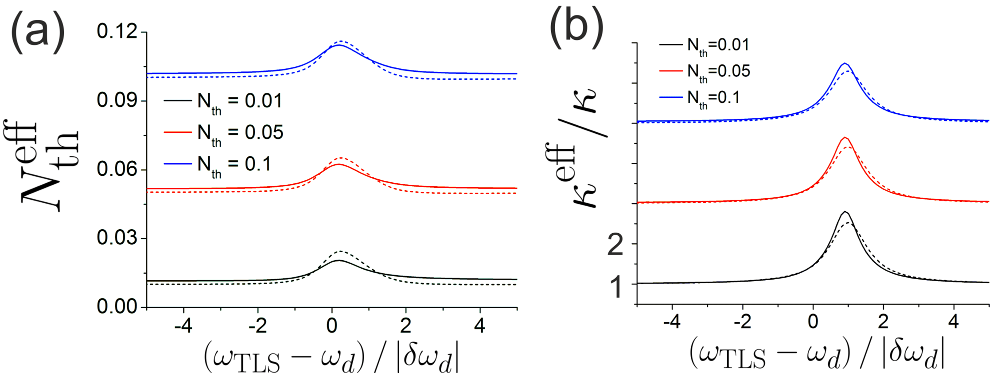

Figure 7.2: (a) Effective thermal photon number and (b) effective damping rate of the driven nonlinear resonator as function of the TLF frequency. The solid lines show the results obtained via the distribution function and the emission spectrum, while the dashed lines show the approximative analytical expressions (7.11) and (7.12). The rate Γ_1 is given by $\Gamma_1/\left|\delta\omega_d\right| = 1.33$, other parameters like in Fig. 7.1. For better visibility, the blue and red curves in (b) are shifted along the y-axis.

Effective damping and temperature

The dependence of the average photon number on the TLF frequency can be well explained by a shift of the detuning between the driving and the resonator. However, our approximative analytical results predict that the TLF also influences the damping rate and the temperature of the resonator. In order to check our predictions, we have to investigate properties of the resonator which have a strong dependence on the damping and the temperature.

We start by discussing the occupation probability $\bar{P}(k) = \langle k\,|\tilde{\rho}|\,k\rangle$ of the quasi-energy states of the driven resonator. For small damping, $\kappa \ll |\delta\omega_d|$, $\bar{P}(k)$ is approximatively described by a Boltzmann function, parametrized by the Planck number $\bar{n}_e = N_{\text{th}} + (2N_{\text{th}}+1)\sinh^2 r^*$ [90]. For low-amplitude oscillations, the squeezing factor r^* is much smaller than 1, so that we can use the approximation $\bar{n}_e \approx N_{\text{th}}$, which yields the relation $\bar{P}(k+1)/\bar{P}(k) = \exp\left(-\hbar\left|\delta\omega_d\right|/k_B T\right)$.

In the case of coupling to a TLF, we can define an effective temperature via the definition $\bar{P}(2)/\bar{P}(1) = \exp\left(-\hbar\left|\delta\omega_d\right|/k_B T^{\text{eff}}\right)$, where $k = 1, 2$ denotes the two quasi-energy states which are nearest to the local minimum of the quasi-potential. This corresponding effective thermal photon number obeys the relation $N_{\text{th}}^{\text{eff}} = \left(\bar{P}(1)/\bar{P}(2) - 1\right)^{-1}$.

In Fig. 7.2a, we plot the effective thermal photon number as function of the TLF frequency. The solid lines show the results extracted from the distribution function $\bar{P}(k)$, while the dashed lines show the approximative analytical result (7.12). In all cases, we observe an increase of the temperature around the TLF frequency $\omega_{\text{TLS}} = \omega_d$. We also see that there is a good qualitative agreement between the numerical and the analytical results. The analytical approximation tends to overestimate the increase of the effective temperature, however it still provides the correct order of magnitude.

We see that the strongest increase occurs when the two-level-fluctuator is close to resonance with the driving frequency, $\omega_{\text{TLS}} \approx \omega_d$. This is consistent with Eq. (7.12), which predicts that the increase of the thermal photon number is proportional to the occupation probability $1/2 \cdot (1 + \langle\sigma_z\rangle)$ of the excited TLF state. When the TLF is in its excited state, it can make a coherent transition back to the ground state and create a photon in the resonator, which corresponds to heating and thus to an increase of the temperature. On the other hand, the TLF is driven by the coherent oscillations of the resonator, so that the occupation probability of the excited TLF state becomes large when the driving is matching the TLF frequency.

We now turn to the discussion of the effective damping rate κ^{eff}, which will be based on the linewidth of the primary side-peaks visible in the emission spectrum (see Sec. 6.4). Using the approximative analytical formulas for the emission peaks derived by the author V. Peano in Ref. [94], we obtain the expression

$$S(\omega_d + \omega) = \frac{1}{|\delta\omega_d|} \cdot \frac{\kappa \cosh^2 r_1^* \bar{n}_e}{(\omega - \nu_1 \cdot |\delta\omega_d|)^2 + (\kappa/2)^2} \,. \tag{7.13}$$

for the primary side-peak at the frequency $\omega \approx \omega_d + |\delta\omega_d|$. From this expression it follows that the damping rate κ is equal to the full width at half maximum (FWHM) of the emission line. We note that our fully numerical calculations show that the FWHM is actually slightly bigger than the damping rate; however, in the parameter regime used here the corrections are rather small and can be neglected.

Fig. 7.2b shows the effective damping rate calculated via the HWHM of the primary side-peak (solid lines) as well as the analytical expression (7.11) that we derived for κ^{eff} (dashed lines). Here we observe a strong increase of the damping rate around the TLF frequency $\omega_{\text{TLS}} = |\delta\omega_d|$. We also see a good quantitative agreement between the numerical and analytical results.

The increase of the effective damping rate results from processes where the TLF absorbs a photon from the resonator or emits a photon into the resonator. The absorption is the most efficient when the TLF and the resonator

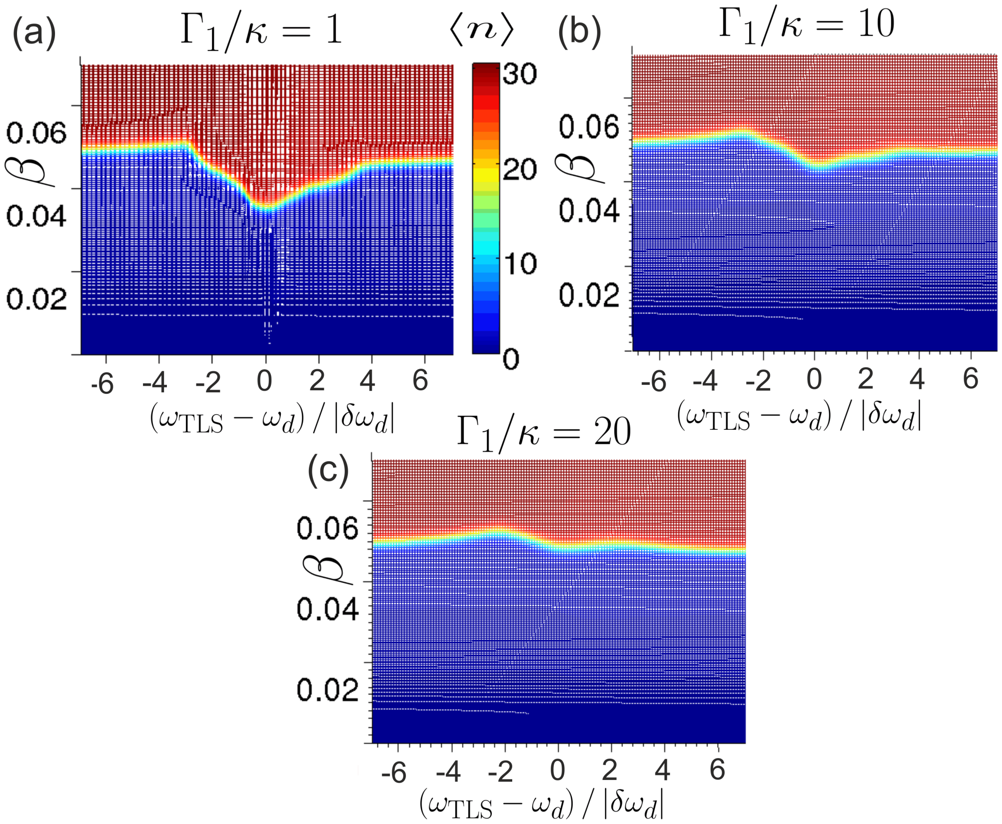

Figure 7.3: Average photon number $\langle n \rangle$ as function of the scaled driving strength β and the TLF frequency at zero temperature, $N_{\mathrm{th}} = 0$ for different values of the rate Γ_1. Other parameters like in Fig. 7.1.

are in resonance, $\omega_{\mathrm{TLS}} = \omega_R$. Since in our case the detuning $\delta\omega_d$ is negative, we can write this resonance condition in the form $\omega_{\mathrm{TLS}} - \omega_d = \omega_R - \omega_d = + |\delta\omega_d|$, which is confirmed by our numerical results and by the analytical expression that we derived for κ^{eff}.

7.3 The stable state

In the regime of bistability, a driven nonlinear resonator can display low-amplitude and high-amplitude oscillations. In the stationary state, for $t \to \infty$, the resonator relaxes to one of the two oscillation states, which we will refer to as the stable state. In general, the stationary state of the resonator at low driving strength is characterized by low-amplitude oscillations, while for strong driving, the resonator relaxes to the high-amplitude state.

The transition between the two regimes occurs at a certain driving strength which depends on the properties of the driven resonator, most notably the detuning $\delta\omega_d$ from the driving frequency. As we have seen in Sec. 6.1, also the temperature and the damping can have a strong effect. In this section, we want to discuss the influence of a two-level-fluctuator on the stable state of the resonator.

Fig. 7.3 shows the average photon number in the resonator as function of the scaled driving strength $\beta = f^2K/\left(4\delta\omega_d^3\right)$ and the TLF frequency at zero temperature, $N_{\text{th}} = 0$. We first focus on the region where the detuning between the TLF and the driving is large, $|\omega_{TLS} - \omega_d| \gg \Gamma_\varphi$. In this regime, the influence of the TLF on the resonator can be well explained by means of the effective detuning, which can be approximatively expressed as $\delta\omega_d^{\text{eff}} \approx \delta\omega_d + \frac{g^2D_0}{\delta\omega_{\text{TLS}}}$.

If the TLF frequency is smaller than the driving frequency ($\delta\omega_{\text{TLS}} > 0$), it will shift the resonator away from the driving, $\left|\delta\omega_d^{\text{eff}}\right| > |\delta\omega_d|$, so that the transition from low-amplitude to high-amplitude oscillations occurs at a larger driving strength. Similarly, if the TLF frequency is bigger than the driving frequency, the TLF shifts the resonator towards the driving, so that the transition occurs at a smaller driving strength.

If the TLF frequency is close to the driving, the behavior of the resonator can not be explained by means of the effective detuning only. In Figs. 7.3a,b we observe that the transition from low-amplitude to high-amplitude oscillations occurs at a lower driving strength around the TLF frequency $\omega_{\text{TLS}} \approx \omega_d$. This effect can be attributed to the increase of the effective temperature (7.12) induced by the TLF.

Our plots show the behavior at zero temperature, $N_{\text{th}} = 0$; in this regime, even a small increase of the temperature can have a strong effect on the stable state of the resonator. As we discussed in Sec. 6.1, an increase of the temperature generally leads to a transition at a lower driving strength. Here we see that the driving strength at which the transition occurs, reaches its lowest value when the TLF is in resonance with the driving, $\delta\omega_{\text{TLS}} \approx \omega_d$. This is consistent with our earlier observation that the effective temperature reaches its maximum at this resonance. By comparing the two plots in the top row, we see that the effect becomes more pronounced for smaller values of the relaxation rate Γ_1, which is also predicted by our approximative expression for $N_{\text{th}}^{\text{eff}}$.

Fig. 7.3c finally shows the result for a rather large value TLF relaxation rate. Here we observe another effect of the TLF on the driven resonator:

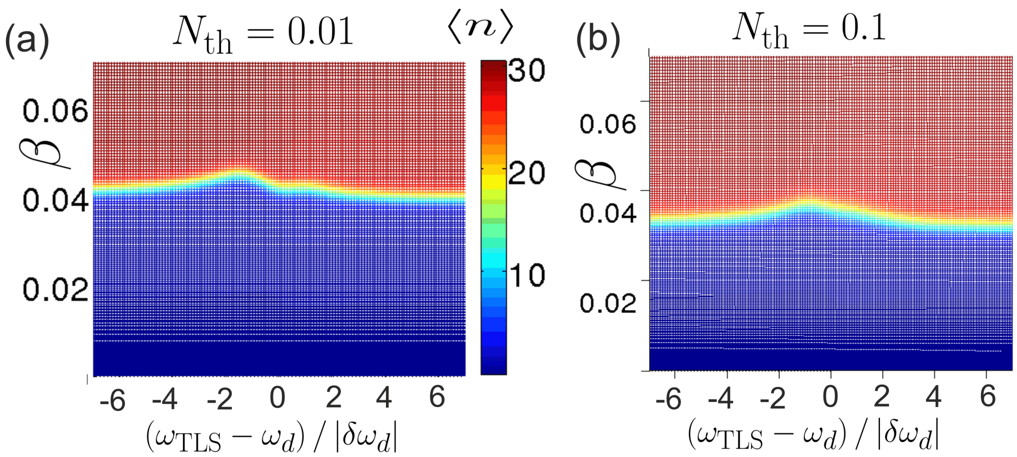

Figure 7.4: Average photon number $\langle n \rangle$ as function of the scaled driving strength β and the TLF frequency for different values of the temperature and for a fixed value $\Gamma_1/\kappa = 10$, other parameters like in Fig. 7.1.

Coming from the right side ($\omega_{\mathrm{TLS}} > \omega_d$), we observe a slight increase of the driving strength at which the system switches from low- to high-amplitude oscillations, which can not result from the increase of the effective temperature or the decrease of the effective detuning. We can attribute this behavior to the effective damping, which reaches its maximum value around the frequency $\omega_{\mathrm{TLS}} = \omega_d + |\delta\omega_d|$. On the other hand, we can still see the effect of the effective temperature in a small region around the frequency $\omega_{\mathrm{TLS}} = \omega_d$.

So far, we have restricted our discussion on the case of zero temperature, $N_{\mathrm{th}} = 0$. We will now briefly discuss the case of finite temperature. Fig. 7.4 shows the average photon number in the resonator for (a) $N_{\mathrm{th}} = 0.01$ and (b) $N_{\mathrm{th}} = 0.1$. We note that with increasing physical temperature, the transition from low-amplitude to high-amplitude oscillations occurs at a lower driving strength, as can be seen in the asymptotic behavior for large values of $|\omega_{\mathrm{TLS}} - \omega_d|$.

We first turn to the case $N_{\mathrm{th}} = 0.01$. Starting from TLF frequencies larger than the driving, $\omega_{\mathrm{TLS}} > \omega_d$ and moving towards the resonance $\omega_{\mathrm{TLS}} = \omega_d$, the transition from low-amplitude to high-amplitude-oscillations occurs at higher driving strength. Like before, we can attribute this effect to an increase of the effective damping. As the physical temperature of the resonator is finite, a further increase of the effective temperature, induced by the TLF, has now a smaller effect and is dominated by the effective damping This explains the qualitative differences as compared to Fig. 7.3b in the region around the resonance $\omega_{\mathrm{TLS}} = \omega_d$.

Finally, Fig. 7.4b shows the case of even higher temperature, $N_{\mathrm{th}} = 0.1$. Here the effect of the effective temperature is not visible anymore; for all TLF frequencies close to the driving frequency ω_d, the transition occurs at larger values of the driving strength. The effect is actually more pronounced ob the left side, $\omega_{\mathrm{TLS}} < \omega_d$, where the effects of the effective damping and the effective detuning both work in the same direction.

To summarize our observations, we have seen that, depending on the relaxation rate of the TLF and the temperature of the resonator, the TLF can act mainly as a source of noise or as a source of damping for the resonator.

7.4 The switching rate

Introduction

In this section, we discuss the effects of a TLF on the switching of a driven nonlinear resonator from low- to high-amplitude oscillations. Under strong driving, if the resonator is initialized in a state of low-amplitude oscillations, it will need a certain time to switch to the high-amplitude state (see Sec. 6.2). The switching rate can vary over many orders of magnitude and depends strongly on the parameters of the resonator and on the coupling to the environment.

The sensitivity of the switching rate on small changes of the detuning $\delta\omega_d$ is used in circuit QED experiments to obtain a high-contrast readout of superconducting qubits. The fidelity of this method relies on the mapping between the two qubit states and the two states of the driven nonlinear resonator. For this reason, it is important that the resonator only switches if the qubit is in the excited state and that the switching is not induced by other processes.

On the other hand, we have seen that a two-level-fluctuator influences the effective temperature and damping of the resonator, which themselves can have a strong influence on the switching rate. This motivates us to investigate the behavior of the switching rate in presence of a TLF.

As we mentioned before, in the quantum-mechanical picture, the switching is caused by transitions between quasi-energy levels due to the coupling of the resonator to the environment. The quasi-energy levels around the local minimum of the quasi-potential describe low-amplitude oscillations. The switching from low- to high-amplitude oscillations can be described in analogy to the thermal escape of a particle from a potential well [97].

The switching rate depends on the transition rates between the quasi-energy levels in direction away from the local minimum of the quasi-potential, which describe how “fast” the system can leave the potential well. In App. B, we show how the TLF affects the transition rates between the quasi-energy levels located at the bottom of the quasi-potential well. The effect can be described by means of an effective damping rate (7.11) and temperature (7.12). Although the approximations made in the derivation are not valid for the quasi-energy levels near the top of the quasi-potential well, we can still use our results to obtain a qualitative understanding of the numerical results.

Results

Figs. 7.5a-c show the switching rate $\gamma_{\rm sw}$ of the resonator as function of the TLF frequency for different values of the temperature. To determine the switching rate, we proceed in analogy to the method described in Sec. 6.2, i.e., we solve the master equation numerically with the condition that the driven resonator is initially in a state of low-amplitude oscillations. As the switching rate can vary over several orders of magnitude, we use a logarithmic scale on the y-axis; to illustrate the influence of the TLF on the switching rate, the dotted horizontal line in each plot shows the switching rate without the TLF (for coupling strength $g = 0$).

In all plots, we observe a pronounced increase of the switching rate for TLF frequencies near the driving frequency, $\omega_{\rm TLS} \approx \omega_d$. In the case of low temperature, when the switching rate in absence of the TLF is rather small, the switching rate can grow by several orders of magnitude. For higher temperatures, the increase is still visible, but the effect is not so strong anymore.

We first focus on the asymptotic behavior, when the TLF is far detuned from the driving, $|\delta\omega_{\rm TLS} - \omega_d| \gg g \cdot (f/\,|\delta\omega_d|)$. In this regime, the occupation probability of the two TLF states is not affected by the coupling to the resonator, $\langle\sigma_z\rangle \approx D_0$. The main effect of the TLF on the resonator results from the shift of the detuning, $\delta\omega_d^{eff} \approx \delta\omega_d + g^2\delta\omega_q\langle\sigma_z\rangle/\left(\Gamma_\varphi^2 + \delta\omega_q^2\right) \approx \delta\omega_d - g^2 D_0/(\omega_{\rm TLS} - \omega_d)$, while the increase of the effective damping and temperature can be neglected.

We also see that the switching rate in this regime only depends on the detuning of the TLF frequency from the driving, but not on the TLF dephasing rate. In the case $\omega_{TLS} < \omega_d$, the driven resonator is shifted away from the driving, thus decreasing the switching rate $\gamma_{\rm sw}$, while for TLF frequencies $\omega_{TLS} > \omega_d$, the resonator is brought closer to resonance with the driving, which leads to an increase of the switching rate.

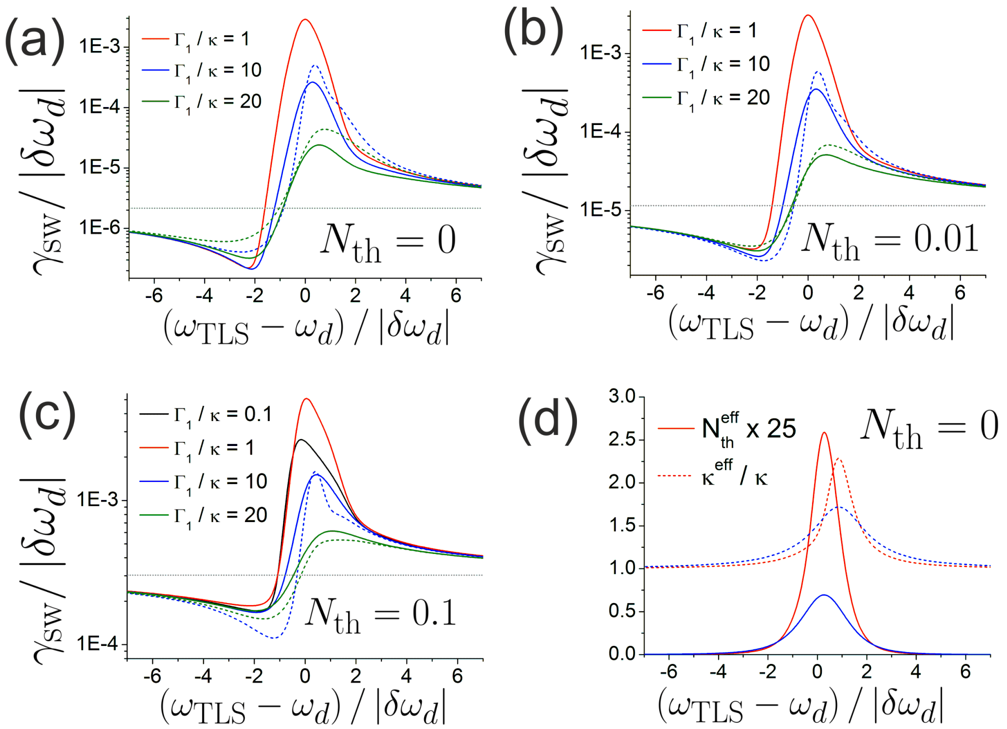

Figure 7.5: (a)-(c) Switching rate of the resonator as function of the TLF frequency for different values of the rate Γ_1 and the thermal photon number $N_{\rm th}$. We show the results used by the full numerical solution of the master equation for the resonator and the TLF (solid lines) and by solving the master equation for the resonator only and using the expressions (7.9), (7.12) and (7.11) for the effective detuning, temperature and damping. The gray dashed lines show the switching rate in absence of the TLF ($g = 0$). (d) Effective damping and temperature calculated from the expressions (7.12) and (7.11). The colors correspond to the colors uses in the plots of the switching rate. The driving strength is fixed to $f / |\delta\omega_d| = 2.8$, other parameters like in Fig. 7.1.

We now focus on the case that the TLF is not far detuned from the driving. When the TLF frequency is close to the driving frequency, $\omega_{\mathrm{TLS}} \approx \omega_d$, the TLF should have no effect on the detuning, $\delta\omega_d^{\mathrm{eff}} \approx \delta\omega_d$. However, we observe that the switching rate can increase by several orders of magnitude in this region. We attribute this effect to the increase of the effective temperature of the resonator induced by the TLF.

Indeed, by using the approximative expressions for the effective detuning, damping and temperature that we derived earlier, we can qualitatively reproduce our numerical results obtained by solving the master equation for the full system (resonator and TLF). On the other hand, we do not obtain a quantitative agreement, since the approximative results tend to overestimate the switching rate. This is consistent with our earlier observation that our analytical expression for the thermal photon number is larger than the effective thermal photon number extracted from the distribution function over the quasi-energy states.

The two-level fluctuator is driven by the coherent oscillations $\langle a\rangle \sim \exp(i\omega_d t)$ of the resonator. The occupation probability $P_\uparrow^{\mathrm{TLF}}$ of the excited TLF state becomes maximum at the resonance $\omega_{\mathrm{TLS}} = \omega_d$. At zero temperature, the semiclassical expression 7.10 for the TLF inversion leads to

$$P_\uparrow^{\mathrm{TLF}}(\omega_{\mathrm{TLS}} = \omega_d) = 1/2 \cdot (1 + \langle\sigma_z\rangle) \approx \frac{2g^2\langle n\rangle}{\Gamma_1\Gamma_\varphi + 4g^2\langle n\rangle}, \tag{7.14}$$

where $\langle n\rangle$ is the average photon number in the low-amplitude regime.

An increase of the TLF dephasing leads to a decrease of the effective temperature, since the latter is proportional to the occupation probability of the excited TLF state, $N_{\mathrm{th}}^{\mathrm{eff}} \sim P_\uparrow^{\mathrm{TLF}}$. This is shown in Fig. 7.5 d, where we plot the approximative expression (7.12) for the thermal photon number at zero physical temperature, $N_{\mathrm{th}} = 0$; the colors of the lines correspond to the colors used in the plots of the switching rate. Consequently, also the switching rate decreases with increasing TLF dephasing.

This general behavior extends to the case of finite temperature, $N_{\mathrm{th}} > 0$ and smaller TLF dephasing. like can be seen by comparing in the plots 7.5a-c. We observe however that the increase of the switching rate becomes less pronounced for increasing physical temperature of the resonator, i.e., when the switching rate of the resonator in absence of the TLF is already rather large.

We note that in the case of large TLF dephasing, the width of the curves $N_{\mathrm{th}}^{\mathrm{eff}}(\omega_{\mathrm{TLS}}^{\mathrm{eff}})$ is approximatively given by the TLF dephasing rate Γ_φ, like can be seen from the analytical expressions for $N_{\mathrm{th}}^{\mathrm{eff}}$ and $\langle\sigma_z\rangle$. This means that

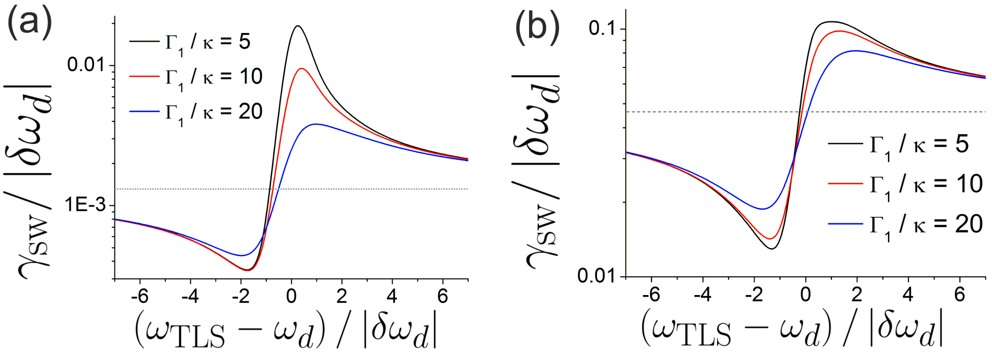

Figure 7.6: Switching rate of the resonator as function of the TLF frequency for different values of the rate Γ_1 two different values of the driving strength, (a) $f/|\delta\omega_d| = 3.2$ and (b) $f/|\delta\omega_d| = 3.6$. The thermal photon number is fixed to $N_{\mathrm{th}} = 0.01$, other parameters like in Fig. 7.1.

the increase of the effective temperature can only significantly change the switching rate if the detuning of the TLF from the driving is not much bigger than the TLF dephasing.

We finally want to discuss the role of the driving strength. Figs. 7.5b, 7.6a and 7.6b show the switching rate for increasing values of the driving strength, but otherwise the same parameters. All the curves shows the same qualitative behavior; however, the influence of the TLF on the switching rate gets weaker for stronger driving strength. This is due to the fact that for larger driving, the switching rate of the resonator is less sensitive to an increase of the temperature (see Sec. 6.2).

In the case $f/|\delta\omega_d| = 2.8$, the switching rate is increased by more than 2 orders of magnitude for TLF frequencies around the value $\omega_{\mathrm{TLS}} \approx \omega_d$, where the effective temperature reaches its maximum value. For driving strength $f/|\delta\omega_d| = 3.2$, the effect is less pronounced and the switching rate only increases by roughly one order of magnitude.

Finally, in the case of even stronger driving, $f/|\delta\omega_d| = 3.6$, the switching rate at the frequency $\omega_{\mathrm{TLS}} = \omega_d$ is very close to the switching rate of the bare resonator, without coupling to a TLF. This means that the dynamics of the driven resonator are not much affected by the increase effective temperature. Indeed, in this regime the shape of the curves is defined by the shift of the detuning (7.9) between the driving and the resonator.

To summarize our results, we have seen that a two-level-fluctuator can lead to an increase of the switching rate by several orders of magnitude. The effect is strong in parameter regimes where the driven resonator is very sensitive to an increase of the temperature, i.e., for small physical temperature and for not too strong driving strength. In parameter regimes where the system is not so sensitive to temperature, the TLF can still affect the switching dynamics by effectively shifting the resonator away or towards the driving frequency and thus decreasing or increasing the switching rate.

Chapter 8

Conclusion

In this thesis, we have theoretically investigated two systems based on superconducting circuits including Josephson junctions: the single-qubit laser and the driven nonlinear resonator. In both systems, we have observed qualitatively new behavior compared to standard quantum optical systems.

In contrast to a many-atom laser, a single-qubit laser shows a smooth transition from the non-lasing to the lasing regime. Nevertheless, the transition is still well-defined and characterized by an increase of the average photon number and a narrowing of the linewidth, which is one of the typical features of conventional lasers.

Single-qubit lasers show some interesting effects due to the strong coupling strength between the qubit and the resonator. In the lasing regime, an increase of the coupling strength leads to an increase of the linewidth and thus to a deterioration of the lasing state. Far above the lasing threshold, the linewidth can even become comparable to the bare linewidth of the resonator, so that in this regime, the laser does not show the typical linewidth narrowing anymore.

We have used the semiquantum model, which provides an accurate estimate of the average photon number and a qualitative description of the linewidth at zero detuning, to investigate the scaling of the lasing properties with the number of qubits. For increasing numbers of qubits, the lasing transition gets sharper, and the growth of the linewidth with the coupling is not so pronounced anymore. In the limit of large numbers of qubits, we recover the semiclassical laser equations.

For zero detuning between the qubit and the resonator, we can use approximation schemes like the semiquantum or the phase diffusion model, which neglect correlations between amplitude and phase fluctuations of the electrical field, to obtain a correct description of the linewidth. For finite detuning however, these approximation schemes fail, so that we rely on the numerical solution of the Liouville equation.

Although the amplitude fluctuations in the lasing regime are rather weak, they have a strong effect on the emission spectrum in the strong coupling regime. If the single-qubit laser is brought near the lasing transition by increasing the detuning, the amplitude fluctuations lead to a strong enhancement of the linewidth. Furthermore, the behavior of the emission line is not governed by a single eigenvalue anymore, so that the lineshape differs from a simple Lorentzian form.

If the qubit is affected by low-frequency noise, the latter leads to an inhomogeneous broadening of the emission line, which for realistic parameters becomes much broader than the natural laser linewidth. We have derived analytical expressions which predict the linewidth and the Gaussian shape of the emission line in presence of slow noise and which agree well with numerical results.

Nonlinear resonators based on superconducting circuits are characterized by rather large nonlinearities, which are attained by using Josephson junctions. We have investigated the emission spectrum of a driven nonlinear resonator, which provides information about the fluctuations of the electrical field in the resonator.

For weak driving, in the low-amplitude regime, the system qualitatively behaves like a linear resonator, so that the emission spectrum only shows a sharp peak due to the coherent driving and two Raman-like primary side-peaks. For strong driving however, in the high-amplitude regime, we observe interesting new features, namely the appearance of two second-order side-peaks, which are not predicted by the standard approach which linearizes the equations of motion for the fluctuations around the stable solution.

We have derived an approximative expression for the emission spectrum, which relates the side-peaks to transitions between quasi-energy levels of the driven resonator. One of the second-order peaks, shifted by twice the detuning from the driving frequency, results from transitions between next-to nearest quasi-energy levels, which are forbidden for a linear resonator.

We also observe a second-order peak located directly at the driving frequency, results from the asymmetry of the quasi-potential. The height of the additional, second-order peaks increases with the nonlinearity, which makes circuit QED systems a promising candidate to observe these peaks experimentally.

The stationary state of the driven nonlinear resonator and the switching rate between low-and high-amplitude oscillations can depend sensitively on the coupling to the environment. Usually the environment is modeled as a thermal bath, which is described by Lindblad terms in the Liouville equation for the density matrix.

In the final part of the thesis, we have investigated the coupling of a driven nonlinear resonator to a two-level-fluctuator. Since in contrast to a thermal bath, the state of a TLF can be affected by the coupling to the resonator, we have used a master equation approach for the coupled resonator-TLF system to calculate the dynamics of the system. We have also shown that, for the case of a TLF with a large dephasing rate, the influence of the TLF on the resonator can be qualitatively described by means of an effective temperature and damping rate for the resonator, which depend on the parameters of the TLF.

We observed that the coupling of the TLF can lead to an increase of the switching rate from low- to high-amplitude oscillations by several orders of magnitude when the TLF frequency is close to the driving frequency of the resonator. This can be explained by an increase of the effective temperature of the resonator: the coherent oscillations of the resonator drive the TLF, and the latter can subsequently cause transitions between quasi-energy levels away from the local minimum of the quasi-potential.

The effect is especially pronounced in parameter regimes where the driven nonlinear resonator is sensitive to an increase of the temperature, i.e., for small physical temperature and moderate driving strength, and for small dephasing rate of the TLF, when the resonator can efficiently drive the TLF.

Appendix A

Emission spectrum of the driven nonlinear resonator

In this section, we will derive an approximative expression for the emission spectrum.

Derivation of the analytical expression

The Liouville equation in the quasi-energy basis

The correlation function of the resonator connected to the emission of photons is given by

$$\langle a^\dagger(t+\tau)a(t)\rangle = \mathrm{Tr}\{a^\dagger e^{G\tau} a\tilde{\rho}_\mathrm{s}\} = \mathrm{Tr}\{a^\dagger \rho^a(\tau)\}, \tag{A.1}$$

where G is the superoperator appearing in the Liouville equation (5.9) for the density matrix, and ρ_s is the stationary density matrix. We we introduced the operator $\rho^a(\tau)$, which follows the same time-evolution as the density matrix, $\rho^a(\tau) = \exp(G\tau)\,\rho^a(0)$, and is defined by the initial condition $\rho^a(0) = a\tilde{\rho}_\mathrm{s}$.

Projecting Eq. (A.1) on the basis of quasi-energy eigenstates, we obtain:

$$\begin{aligned}\langle a^\dagger(t+\tau)a(t)\rangle &= \sum_n \langle n\left|a^\dagger \rho^a(\tau)\right|n\rangle = \sum_{n,m}\langle n\left|a^\dagger\right|m\rangle\langle m\left|\rho^a(\tau)\right|n\rangle \\ &= \sum_m\sum_n \langle n\left|a^\dagger\right|n+m\rangle\langle n+m\left|\rho^a(\tau)\right|n\rangle \end{aligned} \tag{A.2}$$

In order to calculate the matrix elements $\langle n+m\left|\rho^a(\tau)\right|n\rangle$, it is convenient to move to the interaction picture with respect to the system Hamiltonian

H, $\rho_I^a(\tau) = \exp\left(iH\tau/\hbar\right)\rho^a(\tau)\exp\left(-iH\tau/\hbar\right)$. This leads to the following equations:

$$
\begin{aligned}
& \frac{d}{d\tau}\langle n+m\left|\rho_I^a(\tau)\right|n\rangle = \langle n+m\left|L_{RI}\,\rho_I^a(\tau)\right|n\rangle \\
= \;& \frac{\kappa}{2}\left(N_{th}+1\right)\langle n+m\left|2a_I\rho_I^a(\tau)a_I^\dagger - \left[a_I^\dagger a_I,\rho_I^a(\tau)\right]_+\right|n\rangle \\
+ \;& \frac{\kappa}{2}N_{th}\,\langle n+m\left|2a_I^\dagger\rho_I^a(\tau)a_I - \left[a_I a_I^\dagger,\rho_I^a(\tau)\right]_+\right|n\rangle,
\end{aligned}
\tag{A.3}
$$

where the photon creation and annihilation operators $a_I^{(\dagger)}$ are now time-dependent, $a_I^{(\dagger)}(\tau) = \exp\left(iH\tau/\hbar\right)a^{(\dagger)}\exp\left(-iH\tau/\hbar\right)$.

The secular approximation

We can formally write Eq. (A.3) in the form [48]

$$
\begin{aligned}
& \frac{d}{d\tau}\langle n+m\left|\rho_I^a(\tau)\right|n\rangle = \sum_{k,l}\gamma_{n+m,n,k,l}(\tau)\,\langle k\left|\rho_I^a(\tau)\right|l\rangle \\
= \;& \sum_{k,l}R_{n+m,n,k,l}\,e^{i(\omega_{n+m}-\omega_n-\omega_k+\omega_l)\tau}\,\langle k\left|\rho_I^a(\tau)\right|l\rangle,
\end{aligned}
\tag{A.4}
$$

where the expression

$$
\begin{aligned}
& R_{n+m,n,k,l} = \frac{\kappa}{2}\left(N_{th}+1\right)[\,2\langle n+m\left|a\right|k\rangle\langle l\left|a^\dagger\right|n\rangle \\
& -\langle n+m\left|a^\dagger a\right|k\rangle\;\delta_{l,n} - \langle l\left|a^\dagger a\right|n\rangle\delta_{k,n+m}\,] \\
& +\frac{\kappa}{2}N_{th}[\,2\langle n+m\left|a^\dagger\right|k\rangle\langle l\left|a\right|n\rangle \\
& -\langle n+m\left|aa^\dagger\right|k\rangle\;\delta_{l,n} - \langle l\left|aa^\dagger\right|n\rangle\delta_{k,n+m}\,]
\end{aligned}
\tag{A.5}
$$

is time-independent. We will now calculate the matrix elements using the secular approximation, which means that we will only consider terms for which the exponential $\exp\{i\left(\ldots\right)\tau\}$ disappears. In other words, only contributions which satisfy the equation $\omega_{n+m} - \omega_n - \omega_k + \omega_l = 0$ will be kept.

Evaluating the matrix elements $\langle n+m\left|\rho_a(\tau)\right|n\rangle$

In order to derive an expression for the emission spectrum, we will now make the assumption that the stationary density matrix $\tilde{\rho}_{\mathrm{s}}$ is approximatively diagonal in the basis of quasi-energy states. This can be checked numerically and is justified for small damping, $\kappa \ll |\delta\omega_d|$. In this case, the matrix elements of the operator ρ_a at the time $\tau = 0$ can be written in the form

$$\langle n+m\,|\rho_a(0)|\,n\rangle = \langle n+m\,|a\tilde{\rho}_{\mathrm{s}}|\,n\rangle = \langle n+m\,|a|\,n\rangle\langle n\,|\tilde{\rho}_{\mathrm{s}}|\,n\rangle. \tag{A.6}$$

Diagonal elements

Within the secular approximation, the time-derivative $\frac{d}{d\tau}\langle n\,|\rho_I^a(\tau)|\,n\rangle$ is coupled only to other diagonal matrix elements $\langle k\,|\rho_I^a(\tau)|\,k\rangle$:

$$\frac{d}{d\tau}\langle n\,|\rho_I^a(\tau)|\,n\rangle = \sum_k R_{n,n,k,k}\,\langle k\,|\rho_I^a(\tau)|\,k\rangle. \tag{A.7}$$

We can now split up the matrix elements $\langle n\,|a|\,n\rangle$ into the sum $\langle n\,|a|\,n\rangle = \langle a\rangle + \langle n\,|\Delta a|\,n\rangle$, where $\langle a\rangle$ is the average value of the annihilation operator a in the stationary state, and the operator $\Delta a = a - \langle a\rangle$ denotes the fluctuations of the oscillation amplitude.

For a driven nonlinear resonator, the second term in the sum would vanish, but due to the nonlinearity, it has a finite value. For the diagonal elements of the operator ρ_I^a at time $\tau = 0$, we obtain

$$\langle n\,|\rho_I^a(0)|\,n\rangle = \langle a\rangle\langle n\,|\tilde{\rho}_{\mathrm{s}}|\,n\rangle + \langle n\,|\Delta a|\,n\rangle\langle n\,|\tilde{\rho}_{\mathrm{s}}|\,n\rangle \tag{A.8}$$

The first term is proportional to the diagonal elements of the stationary matrix density matrix ρ_{s}; since the latter obey the equation $\frac{d}{d\tau}\langle n\,|\tilde{\rho}_{\mathrm{s}}|\,n\rangle = \sum_k R_{n,n,k,k}\,\langle k\,|\rho_{\mathrm{s}}|\,k\rangle = 0$, this term will be constant in time. On the other hand, the second term will decay, so that the diagonal elements of the operator $\rho_I^a(\tau)$ have the form

$$\langle n\,|\rho_I^a(\tau)|\,n\rangle = \langle a\rangle\langle n\,|\tilde{\rho}_{\mathrm{s}}|\,n\rangle + A_n(\tau), \tag{A.9}$$

where $A_n(\tau)$ is a real function that satisfies the initial condition $A_n(0) = \langle n\,|\Delta a|\,n\rangle\langle n\,|\tilde{\rho}_{\mathrm{s}}|\,n\rangle$ and decays to 0, $A_n(\tau) \to 0$ for $\tau \to \infty$. The diagonal elements thus lead to the contribution

$$\begin{aligned}\langle a^\dagger(t+\tau)a(t)\rangle|_{m=0} &= \sum_n \langle n\,|a^\dagger|\,n\rangle\langle n\,|\rho_a(\tau)|\,n\rangle \\ &= \langle a\rangle \sum_n \langle n\,|a^\dagger|\,n\rangle\langle n\,|\tilde{\rho}_{\mathrm{s}}|\,n\rangle + \sum_n \langle n\,|a^\dagger|\,n\rangle A_n(\tau) \\ &= |\langle a\rangle|^2 + A(\tau)\end{aligned} \tag{A.10}$$

to the correlation function, with $A(\tau) = \sum \langle n\,|a^\dagger|\,n\rangle A_n(\tau)$.

Non-diagonal elements

For non-diagonal elements, within the secular approximation, and because of the anharmonicity of the energy spectrum, we only get a contribution to Eq. (A.4) from terms which satisfy $k = n + m$, $l = n$:

$$\frac{d}{d\tau}\langle n+m\,|\rho_I^a(\tau)|\,n\rangle = R_{n+m,n,n+m,n}\,\langle n+m\,|\rho_I^a(\tau)|\,n\rangle. \tag{A.11}$$

This is the same equation as for the non-diagonal elements of the density matrix $\rho(\tau)$. Since we assumed that the stationary density matrix is diagonal, the non-diagonal elements of any initial density matrix will decay to 0 for long times, $\langle n+m\,|\rho(\tau)|\,n\rangle \to 0$ for $t \to \infty$. This means that the expression $R_{n+m,n,n+m,n}$ has to be negative. Introducing the quantity $\kappa_{n+m,n} = -R_{n+m,n,n+m,n}$, we can write:

$$\begin{aligned}\langle n+m\,|\rho_I^a(\tau)|\,n\rangle &= \langle n+m\,|\rho^a(0)|\,n\rangle e^{-\kappa_{n+m,n}\tau}\,,\\ \langle n+m\,|\rho^a(\tau)|\,n\rangle &= \langle n+m\,|\rho^a(0)|\,n\rangle e^{i(\omega_n-\omega_{n+m})\tau}e^{-\kappa_{n+m,n}\tau}\end{aligned} \tag{A.12}$$

with $\langle n+m\,|\rho^a(0)|\,n\rangle = \langle n+m\,|a|\,n\rangle\langle n\,|\tilde{\rho}_{\mathrm{s}}|\,n\rangle$.

The emission spectrum

Using Eqs. (A.9) and (A.12), we obtain an approximative expression for the correlation function $\langle a^\dagger(t+\tau)a(t)\rangle$:

$$\begin{aligned}\langle a^\dagger(t+\tau)a(t)\rangle = |\langle a\rangle|^2 + A(\tau) + \sum_{m\neq 0}\sum_n |\langle n+m\,|a|\,n\rangle|^2\\ \times\,\langle n\,|\tilde{\rho}_{\mathrm{s}}|\,n\rangle e^{i(\omega_n-\omega_{n+m})\tau}e^{-\kappa_{n+m,n}\tau}A(\tau).\end{aligned} \tag{A.13}$$

From this, we directly obtain an expression for the emission spectrum $S(\omega) = 2\,\mathrm{Re}\int_0^\infty d\tau\,\langle a^\dagger(t+\tau)a(t)\rangle e^{-i\omega\tau}$:

$$\begin{aligned}S(\omega) &= 2\pi\,|\langle a\rangle|^2\,\delta(\omega) + 2\,\mathrm{Re}A(\omega)\\ &+ \sum_{m\neq 0}\sum_n |\langle n+m\,|a|\,n\rangle|^2 \times \frac{2\kappa_{n+m,n}\langle n\,|\tilde{\rho}_{\mathrm{s}}|\,n\rangle}{(\omega-[\omega_n-\omega_{n+m}])^2+\kappa_{n+m,n}^2}.\end{aligned} \tag{A.14}$$

The first term describes a sharp peak at the frequency $\omega = 0$ as a consequence of the monochromatic driving, while the second term, $2\,\mathrm{Re}A(\omega) = 2\,\mathrm{Re}\int_0^\infty d\tau A(\tau)\exp(-i\omega\tau)$, describes a broad peak at the frequency $\omega = 0$. Finally, the sum in the second line describes the side-peaks at frequencies $\omega \approx \pm m\,|\delta\omega_d|$.

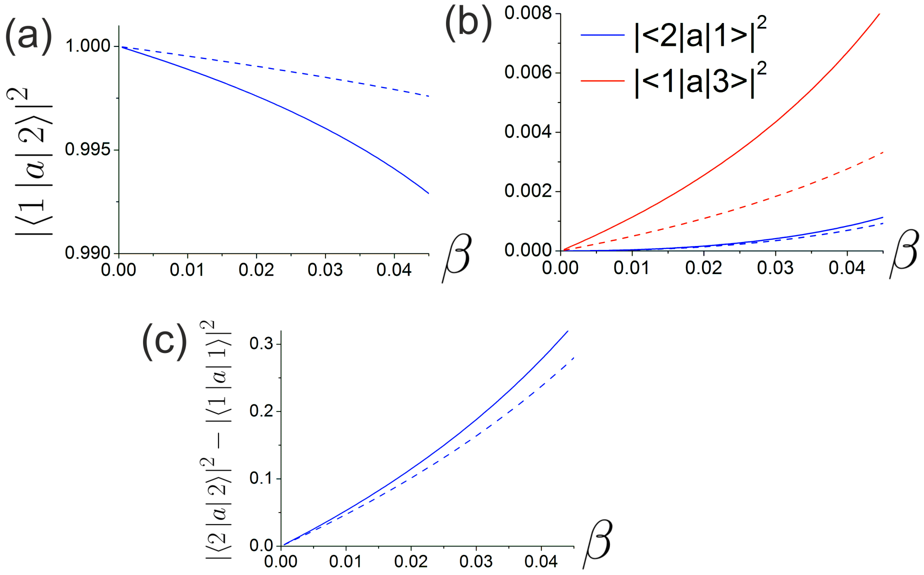

Figure A.1: Matrix elements of the operator a in the regime of low-amplitude oscillations as function of the scaled driving strength for $\lambda = 0.01$ (dashed lines) and $\lambda = 0.02$ (solid lines).

Matrix elements of the operator a

In App. A, we derived an approximative expression for the emission spectrum of a driven nonlinear resonator, predicting that the height of the emission peaks is defined by matrix elements of the form $\langle n + m\,|a|\,n\rangle$. Here we numerical results calculate some of the matrix elements for the regime of low- and high-amplitude oscillations.

Low-amplitude oscillations

We start by discussing the regime of low-amplitude oscillations. In this case, the emission peaks are connected to matrix elements of the operator a between quasi-energy levels located near the local minimum of the quasi-potential. More precisely, the emission peak at the frequency $\omega \approx \omega_d - m \cdot |\delta\omega_d|$ is connected to matrix elements $\langle n + m\,|a|\,n\rangle$.

Fig. A.1 shows some of the matrix elements $|\langle n + m\,|a|\,n\rangle|^2$ as function of the scaled driving strength $\beta = f^2 K/\left(4\delta\omega_d^3\right)$. To show the influence of the effective Planck constant, we also used two different values for the parameter $\lambda = K/\left(2\delta\omega_d\right)$ in each plot.

In A.1a, we see the matrix element $\langle 1 |a| 2\rangle$, connected to the emission peak at the frequency $\omega \approx \omega_d + |\delta\omega_d|$, and which has a value close to 1. This is similar to the case of a linear resonator, where this matrix element has the exact value 1, while all matrix elements $\langle n+m |a| n\rangle$ are zero for $m \neq -1$.

On the other hand, by looking at Fig. A.1b, we see that the matrix element $\langle 2 |a| 1\rangle$ is much smaller than 1, explaining why for finite temperature, the corresponding primary-side peak at the frequency $\omega \approx \omega_d - |\delta\omega_d|$ is much smaller than the primary side-peak at $\omega \approx \omega_d - |\delta\omega_d|$. Only for very small temperature, when the occupation probability $\langle 2 |\tilde{\rho}_{\mathrm{s}}| 2\rangle$ of the second quasi-energy levels tends to zero, both peaks can be of comparable (small) height.

We now turn to the second-order peaks at the frequencies $\omega \approx \omega_d \pm 2 |\delta\omega_d|$ and connected to matrix elements of the form $\langle n \pm 2 |a| n\rangle$. The matrix element $\langle 1 |a| 3\rangle$ is shown in Fig. A.1b.

We see that it become comparatively large for larger values of the scaled driving β. However, the height of the corresponding peak is also proportional to the occupation probability $\langle 3 |\tilde{\rho}_{\mathrm{s}}| 3\rangle$ of the third quasi-energy state. For zero temperature, $\langle 3 |\tilde{\rho}_{\mathrm{s}}| 3\rangle$ is very small; on the other hand, for finite temperature and larger values of the scaled driving, the resonator will be in a state of high-amplitude oscillations and not in state of low-amplitude oscillations.

The matrix element $\langle 3 |a| 1\rangle$, which is not shown here, is orders of magnitude smaller than the matrix element $\langle 3 |a| 1\rangle$. For these reasons, none of the second-order peaks are visible in th regime of low-amplitude oscillations.

Finally, Fig. A.1c shows the difference $|\langle 2 |a| 2\rangle|^2 - |\langle 1 |a| 1\rangle|^2$ as measure for the fluctuations of the oscillation amplitude. We can see that the difference is much smaller than in the regime of high-amplitude oscillations.

High-amplitude oscillations

We turn now to the discussion of the regime of low-amplitude oscillations. In this case, the emission peaks are connected to matrix elements of the operator a between quasi-energy levels located near the global maximum of the quasi-potential. More precisely, the emission peak at the frequency $\omega \approx \omega_d + m \cdot |\delta\omega_d|$ is connected to matrix elements $\langle n+m |a| n\rangle$.

In A.2a, we see the matrix elements $\langle 1 |a| 2\rangle$ and $\langle 2 |a| 1\rangle$. We see that they are within the same order of magnitude, which explains, together with the broad distribution function $\bar{P}(k) = \langle k |\tilde{\rho}_{\mathrm{s}}| k\rangle$, that the two primary side-peaks are of similar size. We also see that the parameter λ only has small influence on the matrix elements and tends to slightly reduce their value.

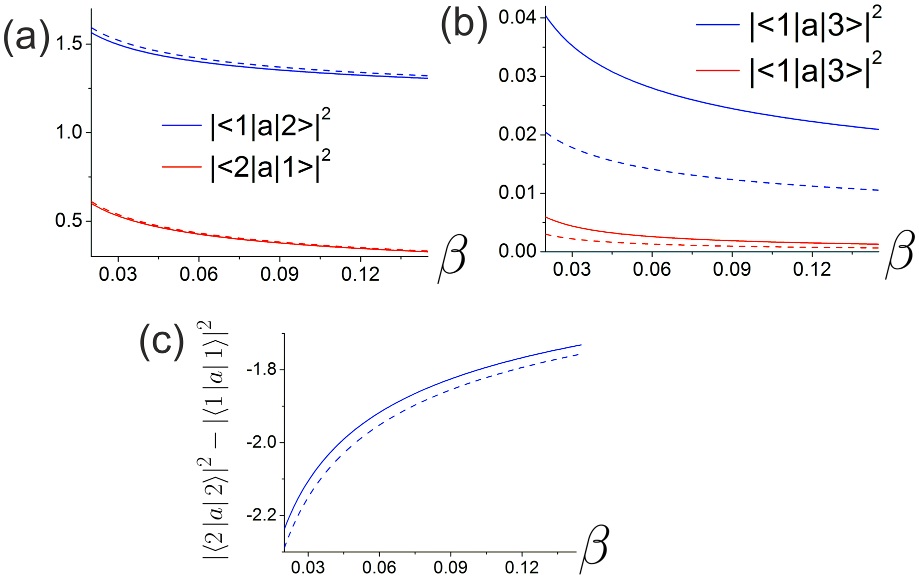

Figure A.2: Matrix elements of the operator a in the regime of low-amplitude oscillations as function of the scaled driving strength for $\lambda = 0.01$ (dashed lines) and $\lambda = 0.02$ (solid lines).

In Fig. A.2b shows the matrix element $\langle 1\,|a|\,3\rangle$. We see that it is relatively large, which, together with the rather large occupation probability $\langle 3\,|\tilde{\rho}_{\mathrm{s}}|\,3\rangle$ of the third quasi-energy state, explains why the second-order peak at the frequency $\omega \approx \omega_d - 2\,|\delta\omega_d|$ becomes is visible in the emission spectrum.

We also see that the absolute value of the matrix element $\langle 1\,|a|\,3\rangle$ clearly increases with the parameter λ, which confirms our observation that the second-order peaks become more pronounced for larger values of λ. On the other hand, the matrix element $\langle 3\,|a|\,1\rangle$, also shown in Fig. A.2b, is rather small. This explains why the corresponding peak at $\omega \approx \omega_d + 2\,|\delta\omega_d|$ is not visible in our plots of the emission spectrum.

Finally, Fig. A.2c shows the difference $|\langle 2\,|a|\,2\rangle|^2 - |\langle 1\,|a|\,1\rangle|^2$. As already mentioned, the difference is much larger than in the case of low-amplitude oscillations. Interestingly, here we only observe only a small dependence on the parameter λ.

Appendix B

Effective temperature and damping

In this appendix we show how we can qualitatively describe the influence of a TLF on the driven resonator by means of an effective temperature and damping. We will assume that the resonator is in the low-amplitude state and that the TLF dephasing is large.

Fig. B.1 shows the quasi-potential of the driven nonlinear resonator around the local minimum. The shape of the potential is defined by the detuning $\delta\omega_d$, the nonlinearity K and the driving strength f. The coupling to the environment, parametrized by the damping rate κ and the thermal photon number N_{th}, leads to transitions between the quasi-energy levels. Additionally, transitions between these levels can be caused by the coupling to the two-level fluctuator.

We start with the Hamiltonian (7.2) for the resonator and the TLF in the rotating frame

$$\begin{aligned}\tilde{H} &= -\hbar\delta\omega_d a^\dagger a + \frac{1}{2}\hbar K a^\dagger a\left(a^\dagger a + 1\right) - \frac{1}{2}\hbar f\left(a + a^\dagger\right) \\ &- \frac{1}{2}\hbar\delta\omega_{\text{TLS}}\sigma_z + \hbar g\left(\sigma_+ a + \sigma_- a^\dagger\right). \end{aligned} \tag{B.1}$$

For our analysis, we follow the method described in Ref. [94] and make a harmonic expansion of the quasi-energy Hamiltonian of the driven nonlinear resonator around the low-amplitude solution, like demonstrated by the dashed line in Fig. B.1 of the quasi-potential. The new ladder operators are defined by the squeezing transformation $a = \alpha + b\cosh r_i^* - b^\dagger \sinh r_i^*$ with the squeezing factor r_i^* and lead to the modified Hamiltonian

$$\tilde{H} = \hbar\left|\delta\omega_d\right| b^\dagger b - \frac{1}{2}\hbar\delta\omega_{\text{TLS}}\sigma_z + \hbar g\left(\sigma_+ b + \sigma_- b^\dagger\right) + \hbar g\alpha\sigma_x. \tag{B.2}$$

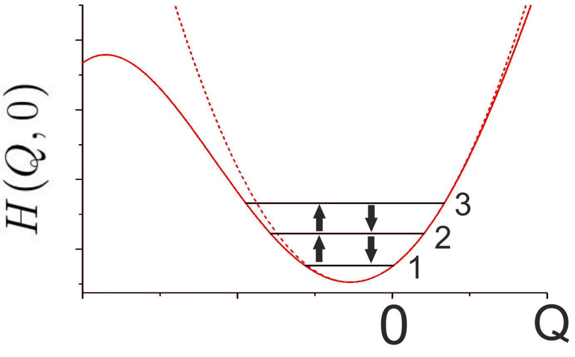

Figure B.1: The quasi-potential around the local minimum; the dashed line shows the harmonic approximation valid in vicinity of the minimum. The solid black lines show the first three quasi-energy levels.

Here we have neglected small coupling terms $\sim g \sinh r_i^*$. We have also assumed that the frequency of the oscillations around the stable solution is equal to the detuning $|\delta\omega_d|$; this approximation is not necessary in our derivation, but we make it for the sake of simplicity. Similarly, we also assume that the quantum temperature n_e is equal to the physical temperature $N_{\rm th}$. In this case, the dissipation terms for the driven resonator are simply given by

$$\begin{aligned} L_R\tilde{\rho} &= \frac{\kappa}{2}\left(N_{\rm th}+1\right)\left(2b\tilde{\rho}b^\dagger - b^\dagger b\tilde{\rho} - \tilde{\rho}b^\dagger b\right) \\ &+ \frac{\kappa}{2}N_{\rm th}\left(2b^\dagger\tilde{\rho}b - bb^\dagger\tilde{\rho} - \tilde{\rho}bb^\dagger\right) \end{aligned}$$

For the TLF, we use the usual dissipation terms (7.4) parametrized by the rates $\Gamma_{\uparrow,\downarrow}$ and Γ_φ^*.

We are interested in the transitions between the quasi-energy levels of the driven resonator. It is useful to introduce the reduced density matrix of the resonator, whose matrix elements obey the relation relation $\langle n\,|\tilde{\rho}_{\rm R}|\,m\rangle = \langle n\uparrow|\tilde{\rho}|\,m\uparrow\rangle + \langle n\downarrow|\tilde{\rho}|\,m\downarrow\rangle$. The diagonal elements of the reduced density matrix describe the occupation probability of the quasi-energy levels:

$$\begin{aligned} \frac{d}{dt}\langle n\,|\tilde{\rho}_{\rm R}|\,n\rangle &= 2g\left\{\sqrt{n+1}\,{\rm Im}\langle n+1\downarrow|\tilde{\rho}|\,n\uparrow\rangle - \sqrt{n}\,{\rm Im}\langle n\downarrow|\tilde{\rho}|\,n-1\uparrow\rangle\right\} \\ &- \kappa\left[(N_{\rm th}+1)n + N_{\rm th}(n+1)\right]\langle n\,|\tilde{\rho}_{\rm R}|\,n\rangle \\ &+ \kappa(N_{\rm th}+1)(n+1)\langle n+1\,|\tilde{\rho}_{\rm R}|\,n+1\rangle \\ &+ \kappa N_{\rm th} n\langle n-1\,|\tilde{\rho}_{\rm R}|\,n-1\rangle \qquad \text{(B.3)} \end{aligned}$$

In this equation, the coupling to the TLF enters via matrix elements of the form $\langle n+1\downarrow|\tilde{\rho}|\, n\uparrow\rangle$. The latter obey the following equation:

$$\begin{aligned}
&\frac{d}{dt}\langle n+1\downarrow|\tilde{\rho}|\, n\uparrow\rangle = (i\delta\omega_d - i\delta\omega_{\mathrm{TLS}})\,\langle n+1\downarrow|\tilde{\rho}|\, n\uparrow\rangle \\
&\quad - \Big(\Gamma_\varphi + \frac{\kappa}{2}(N_{\mathrm{th}}+1)(2n+1) + \frac{\kappa}{2}N_{\mathrm{th}}(2n+3)\Big)\,\langle n+1\downarrow|\tilde{\rho}|\, n\uparrow\rangle \\
&\quad - ig\sqrt{n+1}\;\left[\langle n\uparrow|\tilde{\rho}|\, n\uparrow\rangle - \langle n+1\downarrow|\tilde{\rho}|\, n+1\downarrow\rangle\right] \\
&\quad - ig\lambda\;\left[\langle n+1\uparrow|\tilde{\rho}|\, n\uparrow\rangle - \langle n+1\downarrow|\tilde{\rho}|\, n\downarrow\rangle\right] \\
&\quad + \kappa(N_{\mathrm{th}}+1)\sqrt{(n+2)(n+1)}\langle n+2\downarrow|\tilde{\rho}|\, n+1\uparrow\rangle \\
&\quad + \kappa N_{\mathrm{th}}\sqrt{(n+1)n}\langle n\downarrow|\tilde{\rho}|\, n-1\uparrow\rangle
\end{aligned} \tag{B.4}$$

Within the adiabatic approximation $\kappa \ll \Gamma_\varphi$, we can make use of the relation $\left|\frac{d}{dt}\langle n+1\downarrow|\tilde{\rho}|\, n\uparrow\rangle\right| \ll \Gamma_\varphi\,|\langle n+1\downarrow|\tilde{\rho}|\, n\uparrow\rangle|$ and set the left side of the equation to 0.

Since we are interested in the transition rates between the quasi-energy levels, we only consider the terms $\sim \langle n\uparrow,\downarrow|\tilde{\rho}|\, n\uparrow,\downarrow\rangle$ in the following. The terms $\sim g\lambda$ actually describe the shift of the resonator frequency, which we have already obtained using the semiclassical approach. We thus obtain the following expression:

$$\begin{aligned}
&\langle n+1\downarrow|\tilde{\rho}|\, n\uparrow\rangle \\
&\quad = \left[\Big(\Gamma_\varphi + \frac{\kappa}{2}(N_{\mathrm{th}}+1)(2n+1) + \frac{\kappa}{2}N_{\mathrm{th}}(2n+3)\Big) + i\,(\delta\omega_{\mathrm{TLS}} - \delta\omega_d)\right]^{-1} \\
&\qquad \times\, ig\sqrt{n+1}\;\left(\langle n+1\downarrow|\tilde{\rho}|\, n+1\downarrow\rangle - \langle n\uparrow|\tilde{\rho}|\, n\uparrow\rangle\right) + \ldots \\
&\quad \approx [\Gamma_\varphi - i\Delta]^{-1} \\
&\qquad \times\, ig\sqrt{n+1}\;\left(\langle n+1\downarrow|\tilde{\rho}|\, n+1\downarrow\rangle - \langle n\uparrow|\tilde{\rho}|\, n\uparrow\rangle\right) + \ldots\,,
\end{aligned} \tag{B.5}$$

where $\Delta = \omega_{\mathrm{TLS}} - \omega_{\mathrm{R}}$ is the detuning between the two-level fluctuator and the resonator.

We can now insert this expression into Eq. B.3 for the diagonal elements of the reduced density matrix. In order to obtain a closed equation, we make one further approximation by factorizing the diagonal matrix elements: $\langle n\uparrow,\downarrow|\tilde{\rho}|\, n\uparrow,\downarrow\rangle \approx P_{\uparrow,\downarrow}\cdot\langle n\,|\tilde{\rho}_{\mathrm{R}}|\, n\rangle = 1/2\,(1 \pm \langle\sigma_z\rangle)\cdot\langle n\,|\tilde{\rho}_{\mathrm{R}}|\, n\rangle$.

The occupation probability of the quasi-energy states is then described by the following equation:

$$\begin{aligned}
\frac{d}{dt}\langle n\,|\tilde{\rho}_{\mathrm{R}}|\,n\rangle \;&\approx\; -\left[\kappa(N_{\mathrm{th}}+1)+\frac{g^2\Gamma_\varphi}{\Gamma_\varphi^2+\Delta^2}(1-\langle\sigma_z\rangle)\right]\cdot n\cdot\langle n\,|\tilde{\rho}_{\mathrm{R}}|\,n\rangle \\
&- \left[\kappa N_{\mathrm{th}}+\frac{g^2\Gamma_\varphi}{\Gamma_\varphi^2+\Delta^2}(1+\langle\sigma_z\rangle)\right](n+1)\langle n\,|\tilde{\rho}_{\mathrm{R}}|\,n\rangle \\
&+ \left[\kappa(N_{\mathrm{th}}+1)+\frac{g^2\Gamma_\varphi}{\Gamma_\varphi^2+\Delta^2}(1-\langle\sigma_z\rangle)\right](n+1)\langle n+1\,|\tilde{\rho}_{\mathrm{R}}|\,n+1\rangle \\
&+ \left[\kappa N_{\mathrm{th}}+\frac{g^2\Gamma_\varphi}{\Gamma_\varphi^2+\Delta^2}(1+\langle\sigma_z\rangle)\right]\cdot n\cdot\langle n-1\,|\tilde{\rho}_{\mathrm{R}}|\,n-1\rangle \\
&+ \cdots \qquad\qquad (\mathrm{B.6})
\end{aligned}$$

The terms in the first 4 lines describe transitions between quasi-energy levels n. We now define the rate $\Gamma_{n\to n\pm1}$ as the transition rate from level n tot level $n\pm1$ and obtain

$$\begin{aligned}
\Gamma_{n\to n+1} \;&=\; \left[\kappa N_{\mathrm{th}}+\frac{g^2\Gamma_\varphi}{\Gamma_\varphi^2+\Delta^2}(1+\langle\sigma_z\rangle)\right](n+1) \\
&\equiv\; \kappa^{\mathrm{eff}}N_{\mathrm{th}}^{\mathrm{eff}}(n+1) \\
\Gamma_{n+1\to n} \;&=\; \left[\kappa(N_{\mathrm{th}}+1)+\frac{g^2\Gamma_\varphi}{\Gamma_\varphi^2+\Delta^2}(1-\langle\sigma_z\rangle)\right](n+1) \\
&\equiv\; \kappa^{\mathrm{eff}}(N_{\mathrm{th}}^{\mathrm{eff}}+1)(n+1). \qquad (\mathrm{B.7})
\end{aligned}$$

The transition rates can be described by an effective damping rate $\kappa^{\mathrm{eff}} = \Gamma_{n+1\to n}-\Gamma_{n\to n+1}/(n+1)$,

$$\kappa^{\mathrm{eff}} = \kappa - \frac{2g^2\Gamma_\varphi}{\Gamma_\varphi^2+\Delta^2}\langle\sigma_z\rangle\,, \qquad (\mathrm{B.8})$$

and an effective temperature $N_{\mathrm{th}}^{\mathrm{eff}} = \Gamma_{n\to n+1}/\left[\kappa^{\mathrm{eff}}(n+1)\right]$,

$$N_{\mathrm{th}}^{\mathrm{eff}} = \left[\kappa N_{\mathrm{th}}+\frac{g^2\Gamma_\varphi}{\Gamma_\varphi^2+\Delta^2}(1+\langle\sigma_z\rangle)\right]/\kappa^{\mathrm{eff}}\,. \qquad (\mathrm{B.9})$$

We can obtain closed expressions for the effective damping and temperature by using the semiclassical expression 7.10 for the TLF inversion, which is valid in the regime of low-amplitude oscillations.

Bibliography

[1] J. Clarke and F. K. Wilhelm, *Superconducting quantum bits*, Nature **453**, 1031 (2008).

[2] Yu. Makhlin, G. Schön, and A. Shnirman, *Quantum-state engineering with Josephson-junction devices*, Rev. Mod. Phys. **73**, 357 (2001).

[3] M. A. Nielsen and I. L. Chuang, *Quantum Computation and Quantum Information*, Cambridge University Press (2000).

[4] A. Blais, R.-S. Huang, A. Wallraff, S. M. Girvin, and R. J. Schoelkopf, *Cavity quantum electrodynamics for superconducting electrical circuits: An architecture for quantum computation*, Phys, Rev. A **69**, 062320 (2004).

[5] R. J. Schoelkopf and S. M. Girvin, *Wiring up quantum systems*, Nature **541**, 664 (2008).

[6] A. Lupascu, S. Saito, T. Picot, P. C. de Groot, C. J. P. M. Harmans, and J. E. Mooij, *Quantum non-demolition measurement of a superconducting two-level system*, Nature Phys. **3**, 119 (2007).

[7] M. Metcalfe, E. Boaknin, V. Manucharyan, R. Vijay, I. Siddiqi, C. Rigetti, L. Frunzio, R. J. Schoelkopf, and M. H. Devoret, *Measuring the decoherence of a quantronium qubit with the cavity bifurcation amplifier*, Phys. Rev. B **76**, 174516 (2007).

[8] F. Mallet, F. R. Ong, A. Palacios-Laloy, F. Nguyen, P. Bertet, D. Vion, and D. Esteve, *Single-shot qubit readout in circuit quantum electrodynamics*, Nature Phys. **5**, 791 (2009).

[9] J. M. Fink, M. Göppl, M. Baur, R. Bianchetti, P. J. Leek, A. Blais, and A. Wallraff, *Climbing the Jaynes-Cummings ladder and observing its $\sqrt{n}$ nonlinearity in a cavity QED system*, Nature **454**, 315 (2008).

[10] M. Hofheinz, H. Wang, M. Ansmann, R. C. Bialczak, E. Lucero, M. Neeley, A. D. O'Connell. D. Sank, J. Wenner, J. M. Martinis, and A. N. Cleland, *Synthesizing arbitrary quantum states in a superconducting resonator*, Nature **459**, 546 (2009).

[11] Yu. Makhlin, G. Schön, and A. Shnirman, *Dissipation in Josephson qubits*, New Directions in Mesoscopic Physics (towards Nanoscience), R. Fazio, V. F. Gantmakher, and Y. Imry (eds.), pp. 197-224, Kluwer (2003).

[12] Y. Shalibo, Y. Rofe, D. Shwa, F. Zeides, M. Neeley, J. M. Martinis, and N. Katz, *Lifetime and coherence of two-level defects in a Josephson junction*, Phys. Rev. Lett. **105**, 177001 (2010).

[13] O. Astafiev, K. Inomata, A. O. Niskanen, T. Yamamoto, Yu. A. Pashkin, Y. Nakamura, and J. T. Tsai, *Single artificial-atom lasing*, Nature **449**, 588 (2007).

[14] J. Koch, T. M. Yu, J. Gambetta, A. Houck, D. I . Schuster, J. Majer, A. Blais, M. H. Devoret, S. M. Girvin, and R. J. Schoelkopf, *Charge-insensitive qubit design derived from the Cooper-pair box*, Phys. Rev. A **76**, 042319 (2007).

[15] D. P. DiVincenzo, *The Physical Implementation of Quantum computation*, Fortschr. Phys. **48**, 9-11, 771 (2000).

[16] M. I. Dykman and V. N. Smelyanskiy, *Quantum theory of transitions between stable states of a nonlinear oscillator interacting with a medium in a resonant field*, Zh. Eksp. Teor. Fiz. **94**, 61 (1988).

[17] P. D. Drummond and D. F. Walls, *Quantum theory of optical bistability: Nonlinear polarisability model*, J. Phsy. A: Math Gen. **13**, 725 (1980).

[18] M. O. Scully and M. S. Zubairy, *Quantum Optics*, Cambridge Press, Cambrige, 1997.

[19] D. Meschede, H. Walther, and G. Müller, *One-atom maser*, Phys. Rev. Lett. **54**, 551 (1985).

[20] H. Walther, B. T. H. Varcoe, B.-G. Englert, and T. Becker, *Cavity quantum electrodynamics*, Rep. Prog. Phys. **69**, 1325 (2006).

[21] R. F. Voss and R. A. Webb, *Macroscopic quantum tunneling in 1-μm Nb Josephson junctions*, Phys. Rev. Lett. **47**, 265 (1981).

[22] M. H. Devoret, J. M. Martinis, and J. Clarke, *Measurements of macroscopic quantum tunneling out of the zero-voltage state of a current-biased Josephson junction*, Phys. Rev. Lett. **55**, 1908 (1985).

[23] J. M. Martinis, M. H. Devoret, and J. Clarke, *Energy-level quantization in the zero-voltage state of a current-biased Josephson junction*, Phys. Rev. Lett. **55**, 1543 (1985).

[24] Y. Nakamura, C. D. Chen, and J. S. Tsai, *Spectroscopy of energy-level splitting between two macroscopic quantum states of charge coherently superposed by Josephson coupling*, Phys. Rev. Lett. **79**, 2328 (1997).

[25] J. R. Friedman, V. Patel, W. Chen, S. K. Toipygo, and J. E. Lukens, *Quantum superpositions of distinct macroscopic states*, Nature **406**, 43 (2000).

[26] C. H. van der Wal, A. C. J. ter Haar, F. K. Wilhelm, R. N. Schouten. C. J. P. M. Harmans, T. P. Orlando, S. LLoyd, and J. E. Mooij, *Quantum superpositions of macroscopic persistent current*, Science **290** 773 (2000).

[27] J. I. Cirac and P. Zoller, *Quantum computation with cold trapped ions*, Phys. Rev. Lett. **74**, 4091 (1995).

[28] H. Haeffner, C. F. Roos, and R. Blatt, *Quantum computating with trapped ions*, Phys. Rep. **469**, 155 (2008).

[29] D. Loss and D. P. DiVincenzo, *Quantum computation with quantum dots*, Phys. Rev. A **57**, 120 (1998).

[30] R. Hanson and D. D. Awschalom, *Coherent manipulations of single spins in semiconductors*, Nature **453**, 1043 (2008).

[31] J. M. Raimond, M. Brune, and S. Haroche, *Manipulating quantum entanglement with atoms and photons in a cavity*, Rev. Mod. Phys. **73**, 565 (2001).

[32] D. Esteve and D. Vion, *Solid state quantum bit circuits*, Les Houches Summer School-Session LXXXI on Nanoscopic Quantum Physics (2004).

[33] D. Vion, A. Aassime, A. Cottet, P. Joyez, H. Poithier, C. Urbina, D. Esteve, and M. H. Devoret, *Manipulating the quantum state of an electrical circuit*, Science **296**, 886 (2002).

[34] A. Wallraff, D. I. Schuster, A. Blais, L. Frunzio, R.-S. Huang, J. Majer, S. Kumar, S. M. Girvin, and R. J. Schoelkopf, *Strong coupling of a single photon to a superconducting qubit using circuit quantum electrodynamics*, Nature **431**, 162 (2004).

[35] I. Chiorescu, P. Bertet, K. Semba, Y. Nakamura, C. J. P. Harmans, and J. E. Mooij, *Coherent dynamics of a flux qubit coupled to a harmonic oscillator*, Nature **431**, 159 (2004).

[36] A. Blais, J. Gambetta, A. Wallraff, D. I. Schuster, S. M. Girvin, M. H. Devoret, and R. J. Schoelkopf, *Quantum-information processing with circuit quantum electrodynamics*, Phys, Rev. A **75**, 032329 (2007).

[37] J. H. Plantenberg, P. C. de Groot, C. J. P. M. Harmans, J. E. Mooij, *Demonstration of controlled-CNOT quantum gates on a pair of superconducting quantum bits*, Nature **447**, 836 (2007).

[38] L. DiCarlo, J. M. Chow, J. M. Gambetta, L. S. Bishop, B. R. Johnson, D. I. Schuster, J. Majer, A. Blais, L. Frunzio, S. M. Girvin, and R. J. Schoelkopf, *Demonstration of two-qubit algorithms with a superconducting quantum processor*, Nature **460**, 240 (2009).

[39] R. C. Bialczak, M. Ansmann, M. Hofheinz, E. Lucero, M. Neeley, A. D. O'Connell. D. Sank, H. Wang, J. Wenner, M. Steffen, A. N. Cleland, and J. M. Martinis, *Quantum process tomography of a universal entangling gate implemented with Josephson phase qubits*, Nature Phys. **6**, 409 (2010).

[40] M. A. Sillanpää, J. I. Park, and R. W. Simmonds, *Coherent quantum state storage and transfer between two phase qubits via a resonant cavity*, Nature **449**, 439 (2007).

[41] J. Majer, J. M. Chow, J. M. Gambetta, J. Koch, B. R. Johnson, J. A. Schreier, L. Frunzio, D. I. Schuster, A. A. Houck, A. Wallraff, A. Blais, M. H. Devoret, S. M. Girvin, and R. J. Schoelkopf, *Coupling superconducting qubits via a cavity bus*, Nature **449**, 443(2007).

[42] S. Filipp, P. Maurer, P. J. Leek, M. Baur, R. Bianchetti, J. M. Fink, M. Göppl, L. Steffen, J. M. Gambetta, A. Blais, and A. Wallraff, *Two-qubit state tomography using a joint dispersive readout*, Phys. Rev. Lett. **102**, 200402 (2009).

[43] D. I. Schuster, A. A. Houck, J. A. Schreier, A. Wallraff, J. M. Gambetta, A. Blais, L. Frunzio, J. Majer, B. Johnson, M. H. Devoret, S.

M. Girvin, and R. J. Schoelkopf, *Resolving photon number states in a superconducting circuit*, Nature **445**, 515 (2007).

[44] A. A. Houck, D. I. Schuster, J. M. Gambetta, J. A. Schreier, B. R. Johnson, J. M. Chow, L. Frunzio, J. Majer, M. H. Devoret, S. M. Girvin, and R. J. Schoelkopf, *Generating single microwave photons in a circuit*, Nature **449**, 328 (2007).

[45] D. V. Averin and V. Ya. Aleshkin, *Resonance tunneling of Cooper pairs in a system of two small Josephson junctions*, JETP Lett. **50**, 367.

[46] M.-S. Choi, F. Plastina, and R. Fazio, *Charge and current fluctuations in a superconducting single-electron transistor near a Cooper pair resonance*, Phys. Rev. B **67**, 045105 (2003).

[47] H. J. Carmichael, *Statistical methods in quantum optics 1: Master equations and Fokker-Planck equations*, Springer, Berlin (2002).

[48] C. Cohen-Tannoudji, J. Dupont-Roc, and G. Grynberg, *Atom-Photon interactions: Basic processes and applications*, Wiley Science Paperback Series (1998).

[49] E. T. Jaynes and F. W. Cummings, *Comparison of quantum and semiclassical radiation theories with application to the beam maser*, Proc. IEEE **51**, 89 (1963).

[50] C. W. Gardiner and P. Zoller, *Quantum Noise*, Springer, Berlin (2004).

[51] D.A. Rodrigues, J. Imbers, and A.D. Armour, *Quantum dynamics of a resonator driven by a superconducting single-electron transistor: a solid-state analogue of the micromaser*, Phys. Rev. Lett. **98**, 067204 (2007).

[52] J. Hauss, A. Fedorov, C. Hutter, A. Shnirman, and G. Schön, *Single-qubit lasing and cooling at the Rabi frequency*, Phys. Rev. Lett. textbf100, 037003 (2008).

[53] M. Grajcar, S. H. W. van der Ploeg, A. Izmalkov, E. Il'ichev, H.-G. Meyer, A. Fedorov, A. Shnirman, and G. Schön, *Sisyphus cooling and amplification by a superconducting qubit*, Nature Phys. **4**, 612 (2008).

[54] S. Ashhab, J. R. Johansson, A. M. Zagoskin, and F. Nori, *Single-artificial-atom lasing using a voltage-biased superconducting charge qubit*, New J. Phys. **11**, 023030 (2009).

[55] N. Didier, Y. M. Blanter, and F. Hekking, *Quantum dynamics of a three-level Josephson-atom maser*, Phys. Rev. B **82**, 214507 (2010).

[56] M. Marthaler, Y. Utsumi, D. S. Golubev, A. Shnirman, and G. Schön, *Lasing without inversion in circuit quantum electrodynamics*, Phys. Rev. Lett. **107**, 093901 (2011).

[57] C. Ginzel, H.-J. Briegel, U. Martini, B.-G. Englert, and A. Schenzle, *Quantum optical master equations: The one-atom laser*, Phys. Rev. A **48**, 732 (1993).

[58] M. Reid, K. J. McNeil, D. F. Walls, *Unified approach to multiphoton lasers and multiphoton bistability*, Phys. Rev. A **24**, 2029 (1981).

[59] P. Mandel, *Fluctuations in laser theories*, Phys. Rev. A **21**, 2020 (1980).

[60] Y. Mu and C. M. Savage, *One-atom lasers*, Phys. Rev. A, **46**, 5944 (1992).

[61] C. Lang, D. Bozyigit, C. Eichler, L. Steffen, J. M. Fink, A. A. Abdumalikov, M. Baur, S. Filipp, M. P. da Silva, A. Blais, and A. Wallraff, *Observation of resonant photon blockade at microwave frequencies using correlation function measurements*, Phys. Rev. Lett. **106**, 243601 (2011).

[62] S. André, V. Brosco, A. Shnirman, and G. Schön, *Phase diffusion and locking in single-qubit lasers*, Phys. Rev. A **79**, 053848 (2009).

[63] S. André, V. Brosco, M. Marthaler, A. Shnirman, and G. Schön, *Few-qubit lasing in circuit QED*, Physica scripta **T 137**, 014016 (2009), *Proceedings of the Nobel Symposium 2009, Qubits for future quantum computers, May 2009 in Göteborg, Sweden.*

[64] S. André, P. Q. Jin, V. Brosco, J. H. Cole, A. Romito, A. Shnirman, and G. Schön, *Single-qubit lasing in the strong coupling regime*, Phys. Rev. A **82**, 053802 (2010).

[65] D. F. Walls and G. J. Milburn, *Quantum optics*, Springer (1994).

[66] Y. Nakamura, Y. A. Pahskin, T. Yamamoto, adn J. S. Tsai, *Charge echo in a Cooper-pair box*, Phys. Rev. Lett. **88**, 047901 (2002).

[67] D. J. Van Harlingen, T. L. Robertson, B. L. T. Plourde, P. A. Reichardt, T. A. Crane, and J. Clarke, *Decoherence in Josephson-junction qubits due to critical-current fluctuations*, Phys. Rev. B **70**, 064517 (2004).

[68] F. Yoshihara, K. Harrabi, A. O. Niskanen, Y. Nakamura, adn J. S. Tsai, *Decoherence of flux qubits due to 1/f flux noise*, Phys. Rev. Lett. **97**, 167001 (2006).

[69] J. Schriefl, Y. Makhlin, A. Shnirman, and G. Schön, *Decoherence from ensembles of two-level fluctuators*, New J. Phys. **8**, 1 (2006).

[70] I. Siddiqi, R. Vijay, F. Pierre, C. M. Wilson, L. Frunzio, M. Metcalfe, C. Rigetti, R.J. Schoelkopf, M. H. Devoret, D. Vion, and D. Esteve, *Direct observation of dynamical bifurcation between two driven oscillation states of a Josephson junction*, Phys. Rev. Lett. **94**, 027005 (2005).

[71] F. Ong, M. Boissonneault, F. Mallet, A. Palacios-Laloy, A. Dewes, A. C. Doherty, A. Blais, D. Vion, and D. Esteve, *Circuit QED with a nonlinear resonator: ac-Stark shift and dephasing*, Phys. Rev. Lett. **106**, 167002 (2011).

[72] R. Vijay, M. H. Devoret, and I. Siddiqi, *The Josephson bifurcation amplifier*, Rev. Sci.Instrum. **80**, 111101 (2009).

[73] I. Siddiqi, R. Vijay, F. Pierre, C. M. Wilson, M. Metcalfe, C. Rigetti, L. Frunzio, and M. H. Devoret, *RF-driven Josephson bifurcation amplifier for quantum measurement*, Phys. Rev. Lett. **93**, 207002 (2004).

[74] I. Siddiqi, R. Vijay, M. Metcalfe, E. Boaknin, L. Frunzio, R.J. Schoelkopf, and M. H. Devoret, *Dispersive measurements of superconducting qubit coherence with a fast latching readout*, Phys. Rev. B **73**, 054510 (2006).

[75] N. Boulant, G. Ithier, P. Meeson, F. Nguyen, D. Vion, D. Esteve, I. Siddiqi, R. Vijay, C. Rigetti, F. Pierre, and M. H. Devoret, *Quantum nondemolition readout using a Josephson bifurcation amplifier*, Phys. Rev. B **76**, 014525 (2007).

[76] E. Boaknin, V. Manucharyan, S. Fissette, M. Metcalfe, L. Frunzio, R. Vijay, I. Siddiqi, A. Wallraff, R.J. Schoelkopf, and M. H. Devoret, *Dispersive microwave bifurcation of a superconducting resonator cavity incorporating a Josephson junction*, arXiv:cond-mat/0702445 (2007).

[77] A. Dewes, R. Lauro, F. R. Ong, V. Schmitt, P. Milman, P. Bertet, D. Vion, and D. Esteve, *Demonstrating quantum speed-up in a superconducting two-qubit processor*, arXiv:1110.5170 (2011)

[78] A. Lupascu, E. F. C. Driessen, L. Roschier, C. J. P. M. Harmans, and J. E. Mooij, *High-contrast dispersive readout of a superconducting flux qubit using a nonlinear resonator*, Phys. Rev. Lett. **96**, 127003 (2006).

[79] M. Tinkham, *Introduction to Superconductivity*, Dover Publications (2004).

[80] M. I. Dykman, *Quantum measurements with dynamically bistable systems*, arXiv: 0810.5016 (2008).

[81] D. I. Schuster, A. Wallraff, A. Blais, L. Frunzio, R.-S. Huang, J. Majer, S. M. Girvin, and R. J. Schoelkopf, *ac Stark shift and dephasing of a superconducting qubit strongly coupled to a cavity field*, Phys. Rev. Lett. **94**, 123602 (2005).

[82] V. E. Manucharyan, E. Boaknin, M. Metcalfe, R. Vijay, I. Siddiqi, and M. Devoret, *Microwave bifurcation of a Josephson junction: Embedding-circuit requirements*, Phys. Rev. B **76**, 014524 (2007).

[83] H. Nakano, S. Saito, K. Semba, and H. Takayanagi, *Quantum time evolution in a qubit readout process with a Josephson bifurcation amplifier*, Phys. Rev. Lett **102**, 257003 (2009).

[84] A. Verso and J. Ankerhold, *Dissipation in a rotating frame: Master equation, effective temperature, and Lamb shift*, Phys. Rev. A, textbf81, 022110 (2010).

[85] V. Leyton, M. Thorwart, and V. Peano, *Qubit state detection using the quantum Duffing oscillator*, arXiv: 1109.5562 (2011).

[86] M. I. Dykman, *Critical exponents in metastable decay via quantum activation*, Phys. Rev. E **75**, 011101 (2007).

[87] L.-Z. Guo, Z.-G. Zheng, adn X.-Q. Li, *Quantum dynamics of mesoscopic driven Duffing oscillators*, Europhys. Lett. **90**, 10011 (2009)

[88] M. I. Dykman andM. A. Krivoglaz, *Fluctuations in nonlinear systems near bifurcations corresponding to the appearance of new stable states*, Physica **104 A**, 480 (1980).

[89] M .I. Dykman, M. Marthaler, and V. Peano, *Quantum heating of a parametrically modulated oscillator: Spectral signatures*, Phys. Rev. A **83**, 052115 (2011).

[90] M. I. Dykman, *Periodically modulated quantum nonlinear oscillators*, arXiv: 1112.2407 (2011).

[91] I. Serban and F. K. Wilhelm, *Dynamical tunneling in macroscopic systems*, Phys. Rev. Lett. **99**, 137001 (2007).

[92] I. Serban, M. I. Dykman, and F. K. Wilhelm, *Relaxation of a qubit measured by a driven Duffing oscillator*, Phys. Rev. A **81**, 022305 (2010).

[93] A. A. Clerk, M. H. Devoret, S. M. Girvin, F. Marquardt, R. J. Schoelkopf, *Introduction to quantum noise, measurement, and amplification*, Rev. Mod. Phys. **82**, 1155 (2010).

[94] S. André, L. Guo, V. Peano, M. Marthaler, and G. Schön, *Emission spectrum of the driven nonlinear oscillator*, arXiv:1203.2491 (2012).

[95] I. Serban. F. K. Wilhelm, *Qubit decoherence due to detector switching*, arXiv:0905.3045 (2009).

[96] M. Boissonneault, A. C. Doherty, F. R. Ong, P. Bertet, D. Vion, D. Esteve, and A. Blais, *Back-action of a driven nonlinear resonator on a superconducting qubit*, Phys. Rev. A **85**, 022305 (2012).

[97] M. Marthaler and M. I. Dykman, *Switching via quantum activation: A parametrically modulated oscillator*, Phys. Rev. A **73**, 042108 (2006).